ORNL/TM-9083
ENDF-337

ornl

OAK RIDGE NATIONAL LABORATORY

MARTIN MARIETTA

Calculated Neutron-Induced Cross Sections for ^{63,65}Cu from 1 to 20 MeV and Comparisons with Experiments

D. M. Hetrick
C. Y. Fu
D. C. Larson

OPERATED BY
MARTIN MARIETTA ENERGY SYSTEMS, INC.
FOR THE UNITED STATES
DEPARTMENT OF ENERGY

Printed in the United States of America. Available from
National Technical Information Service
U.S. Department of Commerce
5285 Port Royal Road, Springfield, Virginia 22161
NTIS price codes—Printed Copy: A07 Microfiche A01

ORNL/TM-9083
ENDF-337

Contract No. DE-AC05-840R21400

Engineering Physics and
Mathematics Division

Calculated Neutron-Induced Cross Sections for $^{63,65}Cu$ from 1 to 20 MeV and Comparisons with Experiments

D. M. Hetrick*
C. Y. Fu
D. C. Larson

Date Published - August 1984

*Computer Sciences Division,
Martin Marietta Energy Systems, Inc.
Oak Ridge, TN 37831

OAK RIDGE NATIONAL LABORATORY
Oak Ridge, Tennessee 37831
operated by
MARTIN MARIETTA ENERGY SYSTEMS, INC.
for the
DEPARTMENT OF ENERGY

TABLE OF CONTENTS

LIST OF TABLES

LIST OF FIGURES

ABSTRACT

Nuclear model codes were used to compute cross sections for neutron-induced reactions on both ^{63}Cu and ^{65}Cu for incident energies from 1 to 20 MeV. The input parameters for the model codes were determined through analysis of experimental data in this energy region. Discussion of the models used, the input data, the resulting calculations, extensive comparisons to measured data, and comparisons to the Evaluated Nuclear Data File (ENDF/B-V) for Cu (MAT 1329) are included in this report.

1. INTRODUCTION

The nuclear data needs specified by the National Nuclear Data Center (NNDC) include evaluated neutron cross sections for copper, an important material for fusion reactor applications. Guided by experimental data, we have performed a comprehensive set of nuclear model calculations for neutron reactions on $^{63,65}Cu$ for incident energies between 1 and 20 MeV in which we have particularly addressed the NNDC requests for copper as noted in Ref. ND83. This report documents these calculations.

Several nuclear model codes were employed in this analysis. The optical-model code GENOA (PE67) and the Distorted Wave Born Approximation (DWBA) program DWUCK (KU72) were used to determine optical-model parameters and direct-interaction cross sections needed as input for the Hauser-Feshbach code TNG (FU80, FU80a). The TNG code provides energy and angular distributions of particles emitted in the compound and precompound reactions, ensures consistency among all reactions, and maintains energy balance.

The optical-model parameter sets, discrete energy levels, and other parameters needed as input for TNG are discussed in Chapter II. Chapter III includes a discussion of the computational methods and procedures for the calculations. Figures showing calculated results compared to measured data are given in Chapter IV, along with some brief discussions. In Chapter V, the calculations are compared to cross sections from the ENDF/B-V for Cu. A short summary is given in Chapter VI.

2. PARAMETER DETERMINATION

2.1 NEUTRON OPTICAL-MODEL POTENTIAL

Since optical-model parameters are essential input for our nuclear model calculations, much effort was spent to determine a good set of neutron optical-model parameters for n + ^{63,65}Cu so as to reproduce the elastic scattering angular-distribution data available, as well as the nonelastic, elastic and total cross sections. The experimental angular-distribution data sets selected for fitting were those of Walt and Barschall (WA54) at 1.0 MeV; Holmqvist and Wiedling (HO69) at 2.0, 2.47, 4.0, 6.09, 7.05, and 8.05 MeV; Becker et al. (BE66) at 3.2 MeV; Hill (HI58) at 5.0 MeV; Kinney and Perey (KI74) at 5.5, 7.0, and 8.5 MeV; Coon et al. (CO58) at 14.5 MeV; and Begum et al. (BE79) at 16.1 MeV. Kinney and Perey measured data for both ^{63}Cu and ^{65}Cu at each energy; the other data sets are for natural Cu. The angular-distribution data for ^{63}Cu and ^{65}Cu did not exhibit significant isotopic dependence; thus, all of the above sets were used simultaneously to find one set of optical-model parameters for both ^{63}Cu and ^{65}Cu as described below.

Total elastic scattering cross sections were obtained by integrating each of the angular-distribution data sets. Wick's theorem (WI49) was used to estimate the cross section at 0 degrees, and since none of the data sets cover the angular range to 180 degrees, three extra data points were added between θ_{max} of the measurement and 180 degrees spaced equally in angle with the cross-section value measured at θ_{max}. The added data point at 0 degrees was given an uncertainty of 5%, while the three added points at large angles were given uncertainties of 50%. These added points were used to help constrain the least-squares fit during extraction of the total elastic cross section but were not used during the remainder of the analysis. The total cross-section values were taken from recent work of Larson et al. (LA80) which has already been checked with other available data. The nonelastic cross sections were then extracted by subtracting the total elastic cross sections from the total cross section.

The optical-model code GENOA (PE67) was used to fit the above selected sets of elastic scattering angular-distribution data as well as the total

cross section. Compound elastic-scattering angular distributions were calculated with TNG for each of the above incident neutron energies, and these were used as input to GENOA. The magnitude of the compound elastic contribution was searched on, along with the optical-model parameters, to obtain a minimum chi-square. The energy-dependent magnitude of the compound elastic contribution was represented by the empirical relation

$$\sigma_{CE}(E) = A/\{1 + \exp [B - E)/C]\}. \quad (1)$$

Initially, individual best-fit parameters were obtained for each of the angular-distribution data sets using the code GENOA and searching techniques similar to those described in Ref. FU76. For energies $E_n \geq 5$ MeV, the compound elastic term is very small and was not included. Following the individual searches, an average geometry was obtained by averaging the results of the individual searches, weighted by $\sqrt{1/\chi^2}$ where

$$\chi^2 = \frac{1}{N} \sum_{i=1}^{N} \left(\frac{\sigma_i \text{ (experiment)} - \sigma_i \text{ (calculation)}}{\Delta\sigma_i \text{(experiment)}} \right)^2 .$$

With the average geometry thus determined, individual searches were again done, this time varying only the strengths of the real and surface-imaginary terms V and W_D. A linear least-squares analysis was used to determine an energy dependence for the strengths. Then the code GENOA was made to search again for the parameters A, B, and C in Eq. (1) and the optical-model parameters V and W_D, using the geometry obtained earlier and searching on all data sets simultaneously. Searches on the optical-model parameters and on the parameters of Eq. (1) were repeated until convergence was achieved. As mentioned above, only one set of neutron optical-model parameters was obtained and used as input to the TNG code for both ^{63}Cu and ^{65}Cu.

Values for the best-fit parameter set finally obtained from this work are given in Table 1. This set of neutron optical-model parameters was then used for the rest of the model calculations to generate required neutron transmission coefficients. Figures 1-10 show a comparison of our calculated results with measured elastic scattering angular-distribution data while Fig. 11 shows a comparison of the calculated total, elastic and

nonelastic cross sections with the measured total, and extracted elastic and nonelastic cross sections. Figures 1-6 include results for natural Cu, Figs. 7-8 for ^{63}Cu, and Figs. 9-10 for ^{65}Cu.

2.2 CHARGED-PARTICLE OPTICAL-MODEL PARAMETERS

The proton optical-model parameters are taken from the work of Perey (PE63) as modified by Arthur and Young (AR80). The optical-model potential used for the protons is given in Table 2. Similarly, optical-model parameters for alpha particles were taken from Lemos (LE72) as modified by Arthur and Young (AR80). They are given in Table 3.

2.3 THE DIRECT REACTION MODEL AND PARAMETERS

The Distorted Wave Born Approximation (DWBA) program DWUCK (KU72) was used to calculate the direct-interaction component of the inelastic-scattering cross sections to a number of levels in ^{63,65}Cu for which information was available. Inputs to this code were the neutron optical-model parameters of Table 1 and the deformation parameters, $\beta_\ell'^2$, shown in Table 4 for ^{63}Cu and in Table 5 for ^{65}Cu. The $\beta_\ell'^2$ includes a statistical factor and is used for odd-A targets. It is related to β_ℓ^2, the deformation parameter with $J^\pi=0^+$, via the expression

$$\beta_\ell'^2 = \beta_\ell^2 \left[\frac{2J_f+1}{(2J_i+1)\ (2L+1)} \right] ,$$

where J_i and J_f are the spins of the initial and final states of the nucleus, and L is the angular momentum transfer (YI82). The β_ℓ^2 values shown in Tables 4 and 5 are taken from McCarthy and Crawley (MC66). The resulting calculated direct inelastic excitation cross sections, shown in Figs. 12-13, were used as input in the TNG code (FU80).

2.4 DISCRETE ENERGY LEVELS AND LEVEL-DENSITY PARAMETERS

The statistical-model calculations with TNG require a complete description of the energy levels of the residual nuclei for the various

open channels. The low-energy region of excitation of these nuclei can be adequately described in terms of discrete levels for which we usually know the energy, spin and parity (J^{π}), and gamma-ray deexcitation branching ratios, hereinafter referred to as branching ratios. As the excitation energy increases, our knowledge of these levels becomes incomplete, and eventually, as their number increases, we prefer to describe them in terms of a level density formula. In this section we give the discrete levels used in the calculations and discuss the level density formulae and parameters.

The reactions for which we need level information for the residual nuclei are: $^{63}Cu(n,n')^{63}Cu$, $^{63}Cu(n,p)^{63}Ni$, $^{63}Cu(n,\alpha)^{60}Co$, $^{63}Cu(n,np)^{62}Ni$, $^{63}Cu(n,n\alpha)^{59}Co$, $^{63}Cu(n,2n)^{62}Cu$, $^{63}Cu(n,\gamma)^{64}Cu$, $^{65}Cu(n,n')^{65}Cu$, $^{65}Cu(n,p)^{65}Ni$, $^{65}Cu(n,\alpha)^{62}Co$, $^{65}Cu(n,np)^{64}Ni$, $^{65}Cu(n,n\alpha)^{61}Co$, $^{65}Cu(n,2n)^{64}Cu$, and $^{65}Cu(n,\gamma)^{66}Cu$. The level energies, J^{π} values and gamma-ray branching ratios adopted for these nuclei are given in Tables 6 to 18. There are a few levels where the energies are known, but J^{π} values or branching ratios are experimentally undetermined. These J^{π} values and branching ratios were assigned as indicated by the parentheses in the tables. In most cases, these values are as given in the references (see below); others were estimated from systematics. Excited states were reported having E_x larger than for levels shown in Tables 6-18. However, the branching ratios for these higher levels were not known and thus the levels were not used in the calculations.

The information on the first 15 levels of ^{63}Cu in Table 6 was taken from the compilation of Auble (AU79). The 2.506-MeV level was taken from Dickens (DI83). Levels having energies from 2.536 to 2.889 MeV were taken from Browne et al. (BR78). The levels with energies of 3.3, 3.48, and 3.7 MeV were taken from McCarthy and Crawley (MC66). Although there are many other levels in this energy region, the cross section for exciting these levels can be adequately accounted for in the TNG calculation (FU80) with the level density formulae. We include the above three levels because they are collective and the cross sections for exciting these levels were computed by DWUCK (KU72) and input to TNG. Also, as seen earlier (Tables 4 and 5), the β_{ℓ}^2 values for these levels are large, which gives rise to significant contributions to inelastic-scattering and gamma-ray production cross sections.

For ^{63}Ni, the level energies, the adopted J^{π} values, and gamma-ray branching ratios are given in Table 7. They were taken from Ref. AU79. Table 8 shows the levels, J^{π} values, and branching ratios for ^{60}Co. This information was taken from the compilation of Auble (AU79a), with the exception of the J^{π} value for the 0.786-MeV level, which is from Ref. BR78. Level information for ^{62}Ni, given in Table 9, was taken from the compilation of Halbert (HA79). For ^{59}Co, the level energies, adopted J^{π} values, and branching ratios are given in Table 10, which was compiled from the work of Abbondanno et al. (AB80). The information on levels of ^{62}Cu, given in Table 11, was taken from Ref. HA79.

For ^{65}Cu, the level energies, their J^{π} values and branching ratios adopted are given in Table 12. These were taken from Ref. DI83 for levels having energies of 2.534 MeV and below, and from Ref. MC66 for levels having energies of 3.08, 3.35, and 3.5 MeV. As explained above for ^{63}Cu, we include the last three levels because they are collective. There are many other levels in this energy region, but the level density formulae (FU80) can adequately account for cross sections exciting these "other" levels.

Level information for ^{65}Ni, given in Table 13, was taken from the compilation of Auble (AU75). For ^{62}Co, information was obtained from Ref. HA79 and is given in Table 14. Table 15 shows the levels, J^{π} values, and branching ratios for ^{64}Ni. They were taken from the compilation of Halbert (HA79a). For ^{61}Co, the level energies, adopted J^{π} values, and branching ratios are given in Table 16, which was compiled from the work of Auble (AU75a). Table 17 shows the level information for ^{64}Cu, taken from Ref. HA79a. For ^{66}Cu, the level energies and J^{π} values were taken from Ref. BR78, and are given in Table 18.

To represent the continuum excitation energy region occurring above the highest-energy discrete level (continuum cutoff E_c), the level-density formulae as described by Fu (FU76 and FU80) were used. The level-density parameters of the residual nuclei of all reactions analyzed are given in Table 19. The formulae of Gilbert and Cameron (GI65) were used in computing most of the parameters. However, it was found that for computing the parameter "c" a formula due to Facchini and Saetta-Menichella (FA68) produced better results. Also, the parameter "a" was based on more recent data for the s-wave neutron spacing parameter D_o from Mughabghab et al.

(MU81). For ^{64,66}Cu, the resulting "a" due to Ref. GI65 was too small; the "a" computed using the formula in Ref. GI65 with the new data for D_o was found to be too large. Thus, the parameter "a" for each of the residual nuclei was adjusted so that TNG (FU80) gave reasonable results at a number of incident neutron energies. It should be noted that the parameters T, E_o, c, and E_x in Table 19 all depend on the parameter "a."

2.5 GIANT DIPOLE RESONANCE PARAMETERS

The giant dipole resonance parameters used in this analysis are those reported by Fuller et al. (FU73). For ^{63}Cu, the first resonance has a peak cross section of 63 mb, the width of the resonance is 5 MeV, and the energy of the resonance peak is 16.5 MeV. The second resonance has a peak cross section of 22 mb, the width of the resonance is 7.1 MeV, and the energy of the resonance peak is 21.3 MeV. ^{65}Cu also has two resonances with the first having a peak cross section of 88 mb, width of 5 MeV, and energy of the resonance peak of 16.8 MeV. The second resonance has a peak cross section of 36 mb, the resonance width is 6 MeV, and the resonance peak has energy 20.5 MeV.

2.6 (n,d), (n,t), AND (n,^{3}He) CROSS SECTIONS

The only measured data point found for the (n,t) reaction was reported by Biro et al. (BI75) as 0.32 mb at an incident energy of 14.7 MeV. Since this cross section is very small, the (n,t) reaction was ignored in the TNG calculations. For (n,^{3}He) the shapes of the ^{63,65}Cu(n,α) cross sections were used (FU82), normalized to the ^{63}Cu (n,^{3}He) cross section of 3.2 mb at 14.1 MeV reported by Pollehn and Neurt (PO61) and to the ^{65}Cu (n,^{3}He) cross section of 2.0 mb at 14.8 MeV reported by Poularikas et al. (PO61a). Similarly, for (n,d) the shapes of the ^{63,65}Cu(n,p) cross sections were used (FU82), normalized to the ^{63}Cu(n,d) cross section of 9.0 mb at 14.8 MeV reported by Grimes et al. (GR78) and to the ^{65}Cu(n,d) cross section of 10.0 mb at 14.8 MeV, also from Ref. GR78. These cross sections were not computed by the TNG code but were input to it as correction factors to reduce proportionately the other TNG calculated cross sections.

3. COMPUTATIONAL METHODS AND PROCEDURES

Nuclear model calculations play an important role in modern evaluations for the interpolation and extrapolation of cross sections to energy regions where no data exist, and for predictions of reaction cross sections for which there are few or no experimental data. However, in order to ensure internal consistency, the model calculations should simultaneously reproduce as much of the experimental information as possible for as many reaction channels as reliable data are available. As noted earlier, the model code TNG (FU80, FU80a) was used exclusively for this analysis. Calculations for both ^{63}Cu and ^{65}Cu at a number of incident energies from 1.0 to 20.0 MeV were performed. Parameters required as input to TNG are now summarized. The discrete energy levels for each of the residual nuclei and the gamma-ray branching ratios (Tables 6-18), the level density parameters (Table 19), the direct inelastic cross sections calculated by DWUCK (KU72) as discussed in Section II, the optical-model parameters (Tables 1-3), the giant dipole resonance parameters, and the (n,d) and (n,^{3}He) cross sections were all used as input to the TNG computer code. Parameters required for the precompound mode of reaction were the same as determined previously in a global analysis (FU80) and were found to be satisfactory for the present calculations.

TNG simultaneously computes cross sections for all energetically possible binary reactions and tertiary reactions, and also computes the resulting gamma-ray production cross sections. Also, TNG computes the compound and precompound cross sections in a consistent fashion and conserves angular momentum in both compound and precompound reactions. Thus, the cross-section sets are consistent and energy balance is ensured. The results from TNG are found to agree reasonably well with available data, and these comparisons are discussed in the next section.

4. COMPARISON OF CALCULATIONS WITH EXPERIMENTS

In this section the TNG calculated cross sections are compared with available data. When the comparisons were made for natural Cu, the cross sections for each isotope were multiplied by its fractional natural abundance (69.2% for ^{63}Cu, 30.8% for ^{65}Cu) and summed to obtain the results.

4.1 NONELASTIC CROSS SECTIONS

Comparison of the nonelastic cross section with experiment is shown in Fig. 14. Numerous other data sets were available from the CSISRS library (CS83) but for clarity Fig. 14 contains only those sets with two or more data points. The good agreement lends support to the optical-model parameters adopted for the n + ^{63,65}Cu channel.

4.2 TOTAL INELASTIC SCATTERING CROSS SECTION

The TNG calculation of cross sections for total inelastic-scattering of neutrons from copper is compared to experimental data in Fig. 15. The calculated cross sections agree well with the data of Beyster et al. (BE55, BE56), Bonner and Slatterly (BO59), Taylor et al. (TA55), Ball et al. (BA58), and Thomson (TH63), but they are smaller than the data reported by Slaughter and Dickens (SL83), as well as smaller than those deduced from the neutron scattering data of Kinney and Perey (KI74) between 3 and 8 MeV. The latter two data sets are believed to be too large because they already exceed the upper limit given by the nonelastic cross section shown in Fig. 14.

4.3 ANGULAR DISTRIBUTIONS FOR INELASTIC SCATTERING

The calculated differential ^{63,65}Cu(n,n′) cross sections for exciting the low-lying discrete levels are compared with those measured by Kinney and Perey (KI74) from 5.5 to 8.5 MeV in Figs. 16-23. The DWBA calculations

for inelastic scattering were added to the TNG computations to obtain the results in these figures. In the Kinney and Perey report (KI74), angular distributions for both individual levels and groups of levels are presented. The TNG and DWUCK calculations were summed for the groups of levels for the comparisons. The agreement is fairly good as the calculations usually fall within the error bars of the data. The need for nuclear model analyses can be seen from these figures — the angular range covered by the measurement accounts for only half of the cross section.

4.4 INELASTIC SCATTERING TO DISCRETE LEVELS

The comparison of the calculated and experimental (n,n′) cross sections for individual levels and groups of levels for both ^{63}Cu and ^{65}Cu is given in Figs. 24-29. The calculated direct interaction cross sections (see Figs. 12-13) are included. The data reported by Kinney and Perey (KI74) are generally smaller than the calculation. Their data were obtained by integrating the measured angular observations isotropically. The fact that this procedure can give results which could be too small can be seen in Figs. 16-23, which show that the angular range missed by the measurement contributes a significant part of the cross section.

4.5 ANGULAR DISTRIBUTIONS OF NEUTRON PRODUCTION CROSS SECTIONS

The calculated angular distributions of neutron production cross sections for natural Cu at an incident energy of 13.75 MeV and for secondary energies of E'_n = 4.0-5.0, 6.0-7.0, and 8.0-9.0 MeV are compared with experiments in Fig. 30. The data of Salnikov et al. (SA74) were relative cross sections which we normalized to the data of Vonach et al. (VO80) at 3.0 MeV.

4.6 INTEGRATED YIELD OF SECONDARY NEUTRONS

The integrated yield of secondary neutrons as a function of incident neutron energy is shown in Fig. 31. The TNG calculation is compared with the data of Morgan (MO79) for secondary neutron energies greater than 0.76

MeV. The Morgan data were measured at 130 degrees, whereas the TNG results were computed for all angles (angular spacing was 10 degrees). Since the result integrated over the outgoing energy and angle is dominated by the part of the spectrum at the small outgoing energy end (see next section and Fig. 34 for outgoing neutron energies from 0 to 5 MeV) where the angular distribution is essentially isotropic, the comparison shown in this figure is reasonably valid. The deviation for incident energies greater than 17 MeV is probably due to the (n,3n) contribution, which was not calculated in this work.

4.7 NEUTRON EMISSION SPECTRA

Neutron emission spectra were computed for 22 incident energies; examples of comparisons of calculated spectra with experimental data of Morgan (MO79), Hermsdorf et al. (HE75), Vonach et al. (VO80), and Salnikov et al. (SA75) are shown in Figs. 32-35 for incident neutron energies of 5.5, 9.5, 13.75, and 14.5 MeV, respectively. The data of Morgan were measured at 130 degrees; the other data are angle integrated. The data of Salnikov et al. were normalized to the data of Vonach et al. at 3.0 MeV. The figures show the calculated total neutron emission spectra, as well as the calculated emission spectra from the individual contributing reactions. The (n,n′) continuum and discrete level computations were combined into the one curve labeled "(N,NG)." The curve labeled "(N,NP)" includes contributions from both the (n,np) and (n,pn) reactions. Likewise, the curve labeled "(N,NA)" includes contributions from both the (n,nα) and (n,αn) reactions. The curve labeled "TNG Calculation" is the calculated angle-integrated spectrum and includes the angle-integrated direct inelastic cross sections from the DWUCK code (these were input to the TNG code). For E_n > 10 MeV the angle-integrated spectrum and the 130-degree spectrum differ substantially. For example, the case for E_n = 13.75 MeV (Fig. 34) shows the computed results at an angle of 130 degrees also. In this figure, the dashed curve labeled "Calculation, θ=130°" is the computed direct inelastic cross section at 130 degrees from the DWUCK code added to the TNG calculation at 130 degrees. For E_n=5.5, 9.5, and 13.75 MeV, the elastic cross section shown is the computed shape elastic cross section at

130 degrees from the GENOA code (PE67) added to the compound elastic cross section computed by TNG at 130 degrees. The elastic cross section peak in the Morgan data should not be confused by comparing it with the calculated cross sections from the discrete levels. The computed elastic cross section was not smeared (i.e., folded with the experimental detectors response resolution) for these plots and is not in phase with Morgan's data.

4.8 PROTON AND ALPHA-PARTICLE EMISSION SPECTRA

The calculated (n,xp) and (n,xα) spectra for both ^{63}Cu and ^{65}Cu are compared to measurements by Grimes et al. (GR79, HA77) in Figs. 36-39. The (n,xp) spectra are sums of the partial spectra from the (n,p), (n,pn), and (n,np) reactions. Likewise, the (n,xα) spectra are sums of (n,α), (n,αn), and (n,nα). The measurements were taken at an incident energy of 14.8 MeV, whereas the TNG calculations were at 14.5 MeV. However, the spectral distributions are not expected to vary substantially from E_n = 14.5 MeV to 14.8 MeV.

The proton-particle production spectra for ^{63}Cu and ^{65}Cu, shown respectively in Figs. 36 and 38, have different spectral shapes because of the large (n,np) contribution in ^{63}Cu. For ^{63}Cu, the (n,np) threshold is substantially smaller than the (n,2n) threshold. Thus, there is an energy range (about 5.5 MeV) of excitation in ^{63}Cu (after one neutron is emitted) for which deexcitation by emitting a second neutron is impossible and proton emission is the dominant mode of deexcitation. Even though the outgoing proton energy of 3 MeV is smaller than the energy associated with the peak of the Coulomb barrier, the proton emission spectrum in Fig. 36 exhibits a "peak" at 3 MeV. The corresponding energy range for this "peak" to occur in ^{65}Cu is smaller by about 2 MeV, and the ^{65}Cu(n,np) cross section is much smaller.

The same features of subcoulomb penetration by alpha particles is indicated in the data shown in Figs. 37 and 39 but we cannot reproduce them with calculations. The calculations do, however, reproduce the main features of the higher-energy portions of the alpha-particle spectra reasonably well. In both isotopes, the (n,np) and (n,nα) reactions have

nearly the same thresholds. Thus, theoretically, the subcoulomb penetration by low-energy alpha particles is strongly suppressed by the competing protons emitted at the same energies.

4.9 BINARY AND TERTIARY REACTION CROSS SECTIONS

The calculated binary and tertiary cross sections for ^{63}Cu and ^{65}Cu are compared to available data in Figs. 40-48. As discussed by Fu (FU82), the two data points in Fig. 40 are the $^{63}Cu(n,px)$ cross section so the calculation shown includes the sum of the (n,p) and (n,pn) cross sections. Also, the (n,np) cross section (Fig. 42) does not include the (n,pn) cross section. Figure 41 shows the results for $^{63}Cu(n,\alpha)$. Numerous other data sets were available for $^{63}Cu(n,2n)$ from the CSISRS library (CS83); only those sets with three or more data points are included in Fig. 43. No data were available for the $^{63}Cu(n,\alpha n)$ + $(n,n\alpha)$ cross sections. Other data sets were available for both $^{65}Cu(n,p)$ and $^{65}Cu(n,2n)$ from the CSISRS library (CS83); again, only those sets with more than one point are included in Figs. 44 and 48. The $^{65}Cu(n,\alpha)$ data and calculation are shown in Fig. 45, and the $^{65}Cu(n,pn)$ + (n,np) and $^{65}Cu(n,\alpha n)$ + $(n,n\alpha)$ results are shown in Figs. 46 and 47, respectively.

The calculated $^{63}Cu(n,p)$ excitation function shown in Fig. 40 exhibits a dip around 8 MeV, while the calculated $^{63}Cu(n,\alpha)$ excitation function in Fig. 41 shows a change of slope near the same energy. Both features are due to the competition of one reaction with the other. If the cross sections making up these excitation functions are appropriately summed, one obtains a smooth excitation function near 8 MeV. The (n,n′) cross section at 8 MeV is 20 times larger and is insensitive to such competitions. The $^{63}Cu(n,\alpha)$ reaction is one of several reactions used for dosimetry measurements, and we recently performed an evaluation in which this reaction was studied simultaneously with 12 other dosimetry reaction cross sections. This evaluation (FU82a) is based on the generalized least-squares technique which includes the impacts of measured ratios and cross-reaction covariances. The resulting values for the $^{63}Cu(n,\alpha)$ differ somewhat from the TNG calculations shown in Fig. 41 for the incident-neutron energy region near 8 MeV. The smallness of the cross section and

its sensitivity to details of the model calculation indicates that for applied purposes (e.g. dosimetry) the evaluated results of FU82a should be used. From the point of view of the present analysis, however, the TNG calculation has provided a reasonable characterization of the behavior of the cross section for the $^{63}Cu(n,\alpha)$ reaction over a wide range of incident neutron energies.

4.10 CAPTURE CROSS SECTION

The $^{63}Cu(n,\gamma)$ and $^{65}Cu(n,\gamma)$ calculated cross sections are compared to measurements in Figs. 49 and 50, respectively.

The calculations for the capture cross sections for $E_n < 1$ MeV will be improved when we perform the evaluation in the energy range $E_n = 10^{-5}$ eV to 1 MeV for ^{63}Cu and ^{65}Cu. In this energy range, the optical-model parameters need to be adjusted to reproduce the s- and p-wave strength functions before capture cross-section calculations can be made reliably. Furthermore, the giant dipole parameters are not well determined experimentally and can be adjusted within experimental uncertainties in view of the sensitivity of the calculated capture cross sections to these parameters.

4.11 GAMMA-RAY EXCITATION FUNCTIONS

Excitation functions for six important gamma rays are shown in Figs. 51 through 56. The measurements shown in these figures are discussed in detail by Slaughter and Dickens (SL83). The TNG calculations are in fairly good agreement with the data measured by Rogers et al. (RO77) but are consistently smaller than the measurement of Slaughter and Dickens (SL83) for incident energies greater than 3.0 MeV.

4.12 INTEGRATED YIELD OF SECONDARY GAMMA RAYS

The integrated yield of secondary gamma rays with $E_\gamma > 0.72$ MeV for the TNG calculations and measurements are shown in Fig. 57. The data of Morgan (MO79), Dickens et al. (DI73), and Chapman (CH76) have uncertainties of 10%; those of Drake et al. (DR78) and Rogers et al. (RO77) have uncertainties of 15%. For clarity, the data were plotted at the midpoints of the incident neutron energy bins. The data of Morgan and Chapman are larger than the calculated integrated yield for incident energies greater than 3 MeV. The calculated yields agree with the data of Rogers et al., Dickens et al., and Drake et al. reasonably well except that the data of Dickens et al. are larger than the calculated data for incident energies greater than 10 MeV.

4.13 GAMMA-RAY PRODUCTION CROSS SECTIONS AND SPECTRAL COMPARISONS

The calculated gamma-ray production cross sections are compared to data measured by Rogers et al. (RO77), Morgan (MO79), Dickens et al. (DI73), and Chapman (CH76) in Figs. 58-70. Although the measurements, as well as the calculations by TNG, were made at numerous incident energies, comparisons are shown only for energies of 5.5, 9.5, and 14.5 MeV. The calculated secondary spectra were smeared by a Gaussian function corresponding to the resolution of the detector for the data of Dickens et al. (DI73), Chapman (CH76), and Morgan (MO79). For comparisons of the calculated spectra with the data of Rogers et al. (RO77), the resolution used was the same as that used for comparisons with the Morgan data. Similarly, for comparisons with the data of Drake et al. (DR78), the resolution used was the same as that used for comparisons with the data of Dickens et al. and Chapman.

Before looking at the comparisons between the calculated gamma-ray production spectra and various measurements cited above, we should first mention the energy-conservation constraint imposed in the calculation. In each reaction, the sum of the energies of the outgoing particles (including the recoiled heavy particles) and gamma rays equals the incident neutron energy plus the Q value of the reaction. Because there is good overall

agreement between calculation and experiment in various partial reaction cross sections and particle production spectra, the calculated gamma-ray production spectra can be regarded as the most consistent possible with these data. Detailed discussions on the comparisons shown in Figs. 58-70 follow.

For E_n = 5.5 MeV (Figs. 58, 61, 64, 68) and for $E_\gamma < 2$ MeV, the calculation is in good agreement with the data of Rogers et al. and the data of Dickens et al., but in disagreement with Morgan and with Chapman. For $E_\gamma > 2$ MeV, the data of Rogers et al. differ with both the calculation and the other 3 sets.

For E_n = 9.5 MeV (Figs. 59, 62, 65, 69), the four data sets are not in good agreement with one another. The calculation agrees best with the data of Rogers et al. for $E_\gamma < 1.5$ MeV and with Chapman for $E_\gamma > 1.5$ MeV.

For E_n = 14.5 MeV (Figs. 60, 63, 66, 67, 70), the five data sets are generally in disagreement. The calculation represents a good compromise. At this incident neutron energy, the gamma rays produced in the (n,2n) reaction have large contribution for $E_\gamma < 0.2$ MeV, a gamma-ray energy region not covered by any of the experimental measurements.

5. COMPARISON OF CALCULATION WITH ENDF/B-V

The TNG calculations are compared to a representative set of cross sections from the ENDF/B-V for copper (MAT 1329) in Figs. 71-81. In each figure, the curves labeled "TNG Calculation" include the sum of the calculated cross sections for each isotope multiplied by its fractional natural abundance. Comparison of the total inelastic scattering cross section is given in Fig. 71. The total integrated yield of secondary neutrons as a function of incident neutron energy is shown in Fig. 72. Although the agreement appears quite reasonable in Fig. 72, a look at the neutron emission spectra for incident neutron energies of 5.5, 9.5, and 14.5 in Figs. 73-75 reveals significant differences. The evaluated spectra do not project enough high-energy secondary neutrons, especially for E_n=14.5 MeV. This lack can be understood because the ENDF/B-V evaluation does not include a precompound component. It should be noted that the elastic cross section has not been included in Figs. 72-75. Comparison of the (n,p) and (n,α) cross sections are given in Figs. 76 and 77, respectively.

Marked differences are seen when comparing the TNG calculations for gamma rays with the ENDF/B-V values as shown in Figs. 78-81. The total integrated yields of secondary gamma rays from the calculations and from ENDF/B-V are shown in Fig. 78. The computed gamma-ray production cross sections are compared to ENDF/B-V for incident neutron energies of 5.5, 9.5, and 14.5 MeV in Figs. 79-81. In these plots, the secondary spectra were smeared by a Gaussian function; the resolution width used was arbitrarily taken from the work of Morgan (M079). The ENDF/B-V evaluation was influenced by the data of Chapman (Figs. 68-70), which shows a large peak near 0.3 MeV. From the data shown in Figs. 51-56, we are certain that a large-yield discrete gamma ray near 0.3 MeV is nonexistent at least for E_n = 5.5 MeV.

6. SUMMARY

This report has presented the nuclear models and parameters used in computing neutron-induced reactions on ^{63,65}Cu between 1 and 20 MeV. The calculations were made using the multistep Hauser-Feshbach/precompound model code TNG. Input parameters for TNG, including optical-model sets, discrete level information, level-density parameters, giant dipole resonance parameters and direct reaction model parameters, were discussed. Once the input parameters were determined for TNG no other parameter adjustments were performed in the model calculations for any of the incident neutron energies for which reactions were computed. The resulting calculated cross section sets are consistent and energy balance is ensured.

Calculated results were compared extensively to available measured data. The overall quality of the comparisons leads to the acceptance of the TNG calculations as reliable, especially for those reactions for which no measured data exist. Also, it should be recognized from the comparisons that TNG can be used to resolve discrepancies among experimental data sets. The present work verifies that advanced nuclear model codes can lead to internally consistent evaluations that are in good overall agreement with measured data.

The computed data were compared to cross sections from the present ENDF/B-V evaluation for Cu. The comparisons reveal serious problems in the current ENDF/B-V evaluation for natural copper neutron-emission cross sections and spectra, as well as gamma-ray production cross sections and spectra. These problems probably lead to known difficulties with energy balance in the ENDF/B-V Cu evaluation, which can cause erroneous results for the KERMA (Kinetic Energy Release in Material) factor, as noted by FU (FU80b).

Table 1. Neutron Optical-Model Parameters

$V(MeV) = 51.725 - 0.447E$		$A = 1048.0$
$W(MeV) = 0.0$		$B = 2.47$
$W_D(MeV) = 8.44 + 0.055E$		$C = -0.46$
$U(MeV) = 8.0$		
$r_V(fm) = 1.221$	$a_V(fm) = 0.683$	
$r_W(fm) = 1.223$	$a_W(fm) = 0.507$	
$r_U(fm) = 1.221$	$a_U(fm) = 0.683$	

E = incident energy (MeV),

V = real well depth,

W = imaginary well depth (Wood-Saxon),

W_D = imaginary well depth (Wood-Saxon derivative),

U = spin-orbit potential depth,

r_V, r_W, r_U = radii for various potentials,

a_V, a_W, a_U = diffuseness for various potentials,

A,B,C = parameters used to compute $\sigma_{CE}(E)$ in Eq. (1).

Table 2. Proton Optical-Model Parameters*

$V(MeV) = 58.4 - 0.55E + \left[\frac{0.4Z}{A^{1/3}} + 27.0\left(\frac{N-Z}{A}\right)\right]$		
$W(MeV) = 0.0$	$r_W(fm) = 1.25$	$a_W(fm) = 0.47$
$W_D(MeV) = 13.5 - 0.15E$	$r_V(fm) = 1.25$	$a_V(fm) = 0.65$
	$r_c(fm) = 1.25$	

*Parameter definitions are as in Table 1; r_c is the Coulomb radius.

Table 3. Alpha Optical-Model Parameters*

$V(MeV) = 193.0 - 0.15E$	$r_V(fm) = 1.37$	$a_V(fm) = 0.56$
$W(MeV) = 0.0$	$r_W(fm) = 1.37$	$a_W(fm) = 0.56$
$W_D(MeV) = 21.0 + 0.25E$	$r_c(fm) = 1.40$	

*Parameter definitions are as in Tables 1 and 2.

Table 4. Deformation Parameters of ^{63}Cu Levels

Level	J^{π}	β_{ℓ}^{2}	$\beta_{\ell}'^{2}$
0.669	$1/2^{-}$	0.059	0.0059
0.962	$5/2^{-}$	0.0702	0.021
1.327	$7/2^{-}$	0.0548	0.022
1.412	$5/2^{-}$	0.0121	0.0036
2.506	$9/2^{+}$	0.0408	0.015
3.30	$7/2^{+}$	0.0441	0.012
3.48	$5/2^{+}$	0.0392	0.009
3.70	$3/2^{+}$	0.04[a]	0.006

[a]Assumed value.

Table 5. Deformation Parameters of ^{65}Cu Levels

Level	J^{π}	β_{ℓ}^{2}	$\beta_{\ell}'^{2}$
0.771	$1/2^{-}$	0.04	0.004
1.116	$5/2^{-}$	0.0484	0.015
1.482	$7/2^{-}$	0.038	0.015
1.623	$5/2^{-}$	0.0061	0.0018
2.534	$9/2^{+}$	0.0408	0.015
3.08	$7/2^{+}$	0.04[a]	0.012
3.35	$5/2^{+}$	0.0424	0.009
3.50	$3/2^{+}$	0.04[a]	0.006

[a]Assumed value.

Table 6. Energy Levels and Gamma-Ray Branching Ratios of ^{63}Cu

Initial State			Branching Ratios to State N										
N	J^{π}	E(keV)	1	2	3	4	5	6	7	8	9	11	17
1	$3/2^-$	0											
2	$1/2^-$	669	100										
3	$5/2^-$	962	100										
4	$7/2^-$	1327	84		16								
5	$5/2^-$	1412	72	6	22								
6	$3/2^-$	1547	80	2	18								
7	$7/2^-$	1861	57		43								
8	$3/2^-$	2011	56	13	31								
9	$(1/2^-)$	2062	20	50				30					
10	$5/2^-$	2081	39		19	34		8					
11	$7/2^-$	2093	10		47	43							
12	$9/2^-$	2208			43	57							
13	$5/2^-$	2337	62	1	25		7		5				
14	$7/2^-$	2405	3		45	30	22						
15	$3/2^-$	2497	83	17									
16	$9/2^+$	2506				27			40			33	
17	$(5/2^-)$	2536	25	8	6	5	42	2	6			6	
18	$(3/2^-)$	2696	34	47				16		3			
19	$(7/2^-)$	2717	15	4	5	49		11				16	
20	$(7/2^-)$	2780	53	21				8					18
21	$(3/2^-)$	2806	71			29							
22	$(3/2^-)$	2858	45	22			33						
23	$(5/2^-)$	2889	22	26	52								
24	$(7/2^+)$	3300					(100)						
25	$(5/2^+)$	3480						(100)					
26	$(3/2^+)$	3700								(100)			

Table 7. Energy Levels and Gamma-Ray Branching Ratios of ^{63}Ni

Initial State			Branching Ratios to State N			
N	J^{π}	E(keV)	1	2	3	4
1	$1/2^-$	0				
2	$5/2^-$	87	100			
3	$3/2^-$	156	100			
4	$3/2^-$	518	10	2	88	
5	$1/2^-$	1001	3		51	46
6	$(5/2^-)$	1069	10	56	34	

Table 8. Energy Levels and Gamma-Ray Branching Ratios of ^{60}Co

Initial State			Branching Ratios to State N								
N	J^{π}	E(keV)	1	2	3	4	5	6	7	8	10
1	5^+	0									
2	2^+	59	100								
3	4^+	277	100								
4	3^+	288	100								
5	5^+	436	46		54						
6	3^+	506	100								
7	$(2)^+$	543		43	57						
8	3^+	614		97	3						
9	1^+	739		60					40		
10	4^+	786	52			42	3	2		1	
11	(3^+)	1004	8	48	24				19		1
12	4^+	1006			26					71	3

Table 9. Energy Levels and Gamma-Ray Branching Ratios of ^{62}Ni

Initial State			Branching Ratios to State N		
N	J^{π}	E(keV)	1	2	4
1	0^+	0			
2	2^+	1173	100		
3	0^+	2049	100		
4	2^+	2302	45	55	
5	4^+	2336		100	
6	0^+	2891		100	
7	2^+	3059		30	70
8	2^+	3158	34	33	33
9	4^+	3177		100	
10	2^+	3258		100	

Table 10. Energy Levels and Gamma-Ray Branching Ratios of ^{59}Co

Initial State			Branching Ratios to State N							
N	J^{π}	E(keV)	1	2	3	4	6	7	8	10
1	$7/2^-$	0								
2	$3/2^-$	1100	100							
3	$5/2^-$	1191	100							
4	$3/2^-$	1292	96	4						
5	$1/2^-$	1434		100						
6	$11/2^-$	1460	91		9					
7	$5/2^-$	1482	77	23						
8	$7/2^-$	1745	49		42			9		
9	$7/2^-$	2062	12		43			45		
10	$(5/2)^-$	2087	55			45				
11	$(11/2)^-$	2154					100			
12	$(7/2)^-$	2182	14		75	11				
13	$(7/2)^-$	2205	23			26		51		
14	$(9/2)^-$	2394	26				25		49	
15	$(5/2)^-$	2478	100							
16	$(5/2^-)$	2540	45						55	
17	$(7/2^-)$	2583	54		36					10
18	$(1/2^-)$	2713		100						
19	$(7/2^-)$	2781	85	15						
20	$(7/2^-)$	2825	64	36						

Table 11. Energy Levels and Gamma-Ray Branching Ratios of ^{62}Cu

Initial State			Branching Ratios to State N					
N	J^{π}	E(keV)	1	2	3	4	5	6
1	1^+	0						
2	2^+	41	100					
3	2^+	243	100					
4	1^+	288		100				
5	4^+	390		96	4			
6	3^+	426		100				
7	1^+	548	48	48		4		
8	1^+	637		43	6	51		
9	(2^+)	645	100					
10	3^+	675		37	44		19	
11	2^+	698		39	35			26
12	2^+	728		36	54	10		
13	(2^+)	756	100					
14	$(1)^+$	915	19		15			66
15	$(4)^+$	983		45			35	20
16	$(2)^+$	1023	53		47			

Table 12. Energy Levels and Gamma-Ray Branching Ratios of ^{65}Cu

Initial State			Branching Ratios to State N								
N	J^{π}	E(keV)	1	2	3	4	5	6	7	9	10
1	$3/2^-$	0									
2	$1/2^-$	771	100								
3	$5/2^-$	1116	100								
4	$7/2^-$	1482	80		20						
5	$5/2^-$	1623	55	10	35						
6	$3/2^-$	1725	75		25						
7	$7/2^-$	2094	30		55	15					
8	$5/2^-$	2108	15	10	40	30		5			
9	$1/2^-$	2213	40	60							
10	$7/2^-$	2278	(5)		(95)						
11	$3/2^-$	2327	40	45	15						
12	$9/2^-$	2407			(35)	(40)			(25)		
13	$(5/2^-)$	2533	(20)	(45)		(35)					
14	$9/2^+$	2534				(30)			(50)		(20)
15	$(7/2^+)$	3080					(100)				
16	$(5/2^+)$	3350						(100)			
17	$(3/2^+)$	3500								(100)	

Table 13. Energy Levels and Gamma-Ray Branching Ratios of ^{65}Ni

Initial State			Branching Ratios to State N		
N	J^{π}	E(keV)	1	2	3
1	$5/2^-$	0			
2	$1/2^-$	64	100		
3	$(3/2)^-$	311	98	2	
4	$(3/2)^-$	692	16	77	7
5	$(9/2)^+$	1013	(100)		

Table 14. Energy Levels and Gamma-Ray Branching Ratios of ^{62}Co

Initial State			Branching Ratios to State N	
N	J^{π}	E(keV)	1	2
1	2^+	0		
2	5^+	22	100	
3	(3^+)	230	(100)	
4	(3^+)	244	(100)	
5	1^+	506	100	
6	(1^+)	530	(100)	
7	5^+	610		100

Table 15. Energy Levels and Gamma-Ray Branching Ratios of ^{64}Ni

Initial State			Branching Ratios to State N	
N	J^{π}	E(keV)	1	2
1	0^+	0		
2	2^+	1346	100	
3	$(0)^+$	2277		100
4	4^+	2608		100
5	(0^+)	2865		100

Table 16. Energy Levels and Gamma-Ray Branching Ratios of ^{61}Co

Initial State			Branching Ratios to State N			
N	J^{π}	E(keV)	1	2	3	4
1	$7/2^-$	0				
2	$3/2^-$	1027	100			
3	$(5/2)^-$	1205	100			
4	$(9/2^-)$	1286	100			
5	$(1/2)^-$	1325		81	19	
6	$7/2^-$	1619	55			45
7	$(5/2)^-$	1646	88	12		

Table 17. Energy Levels and Gamma-Ray Branching Ratios of ^{64}Cu

Initial State			Branching Ratios to State N						
N	J^{π}	E(keV)	1	2	3	4	5	7	10
1	1^+	0							
2	2^+	159	100						
3	2^+	278	100						
4	1^+	343	96	4					
5	3^+	362	2	98					
6	4^+	575		6			94		
7	2^+	609	82	8	4	6			
8	1^+	663	32	27	35	6			
9	2^+	739		77	6	4	13		
10	3^+	746			71		29		
11	(0^+)	879	55	3		42			
12	3^+	896	11	40	49				
13	1^+	927	11	16	73				
14	2^+	1241	36	25				14	25

Table 18. Energy Levels of ^{66}Cu

N	J^{π}	E(keV)
1	1^+	0
2	$(2)^+$	186
3	(1^+)	238
4	$(3)^+$	275
5	$(1)^+$	386
6	$(2)^+$	465
7	$(4)^+$	591
8	$(3)^+$	730
9	$(3)^+$	822
10	$(2)^+$	1009
11	$(3)^+$	1017
12	$(1)^+$	1053
13	$(6)^-$	1154
14	$(2)^+$	1213
15	$(3)^-$	1247

Table 19. Level Density Parameters

Residual Nuclei	T (MeV)	E_o (MeV)	a (MeV^{-1})	Δ (MeV)	c	E_c (MeV)	E_x (MeV)
^{63}Cu	0.89	0.081	10.0	1.41	23.12	2.89	6.291
^{63}Ni	0.906	-0.439	10.0	1.20	23.12	1.256	6.327
^{60}Co	0.791	-1.069	11.0	0.0	24.61	0.79	4.169
^{64}Cu	0.81	-0.879	10.3	0.0	24.06	1.288	3.958
^{62}Ni	0.912	1.119	9.67	2.61	22.12	3.262	7.529
^{59}Co	0.963	0.002	9.0	1.29	19.91	2.91	6.332
^{62}Cu	0.97	-1.668	9.17	0.0	20.97	1.052	5.325
^{65}Cu	0.833	0.366	10.5	1.5	24.78	2.594	5.937
^{65}Ni	0.848	-0.302	10.7	1.2	25.25	1.143	6.008
^{62}Co	0.735	-0.78	11.3	0.0	25.84	0.701	3.561
^{66}Cu	0.762	-0.745	10.75	0.0	25.63	1.344	3.597
^{64}Ni	0.850	1.522	10.31	2.7	24.084	2.971	7.245
^{61}Co	0.905	0.066	9.82	1.41	22.217	1.89	6.369

T = nuclear temperature,

E_o = parameter for matching lower energy level density to the higher one,

a = π^2 g/6 (g=density of uniformly spaced single particle states),

Δ = pairing energy correction,

c = spin cut-off parameter,

E_c = continuum cutoff,

E_x = tangency point.

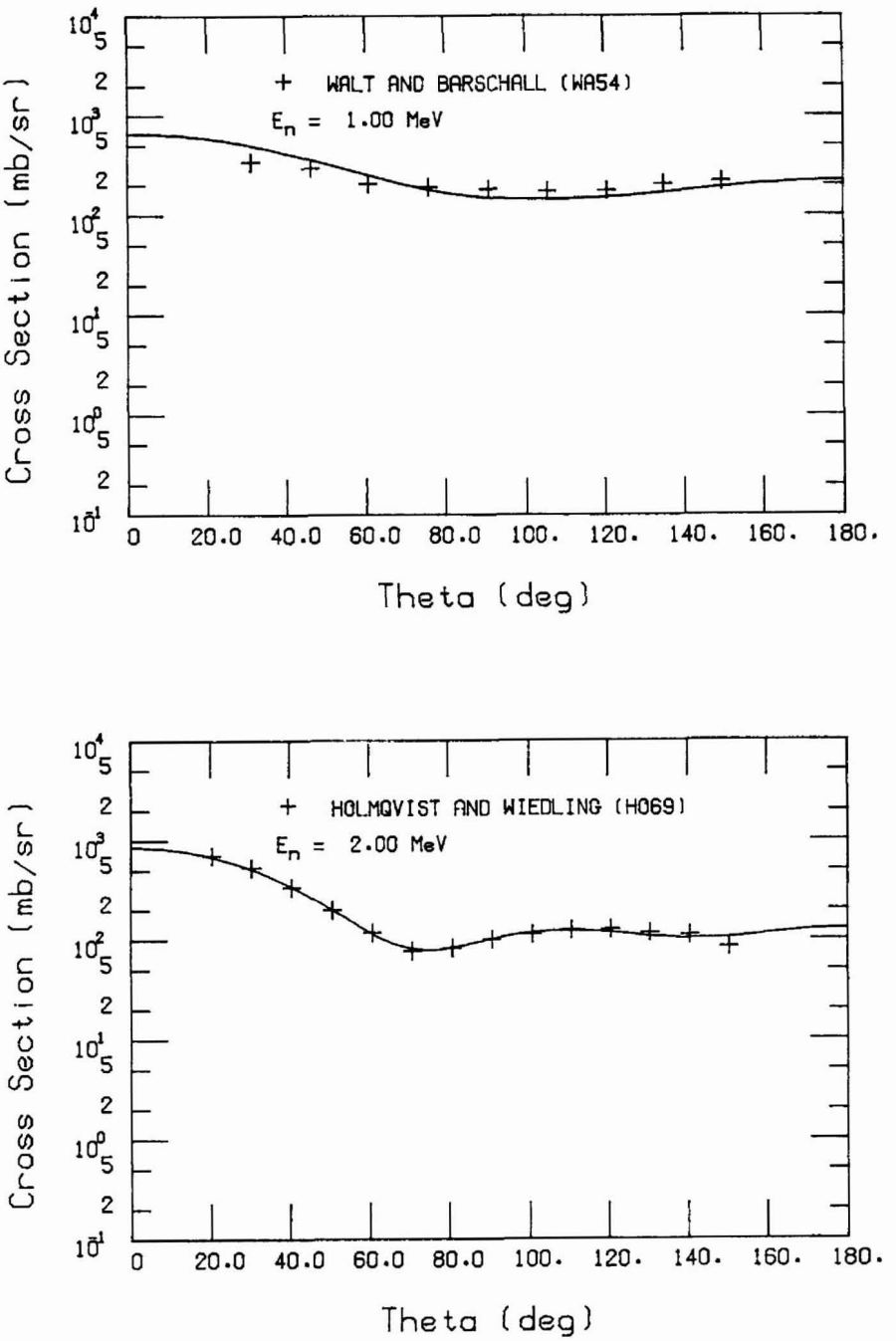

Fig. 1. Comparison of final optical-model fit with data of Walt and Barschall (WA54) and Holmqvist and Wiedling (H069) for Cu at 1.0 and 2.0 MeV.

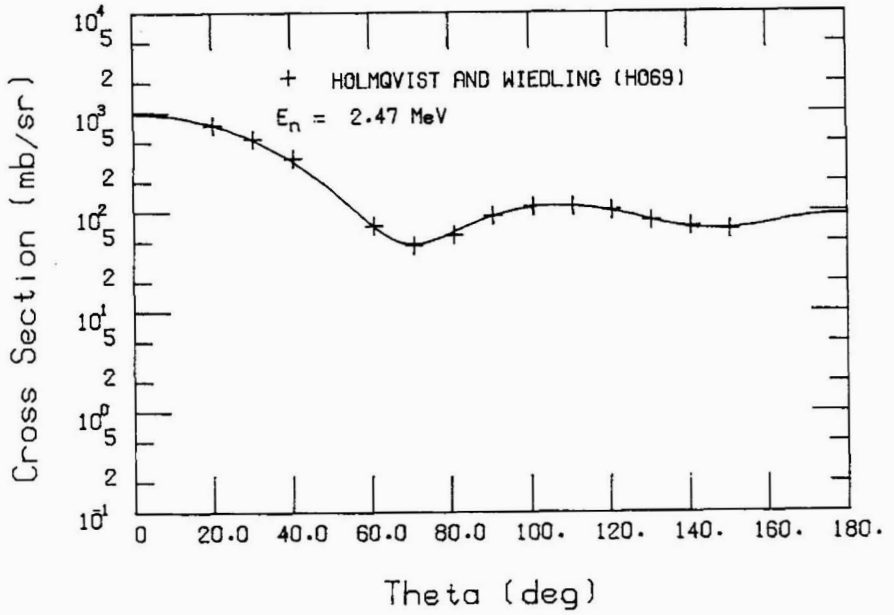

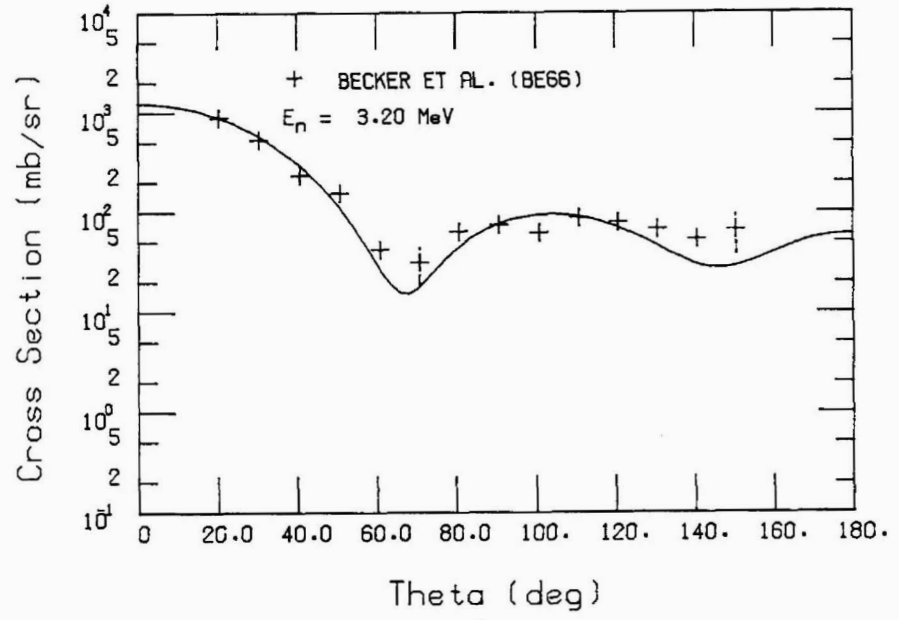

Fig. 2. Comparison of final optical-model fit with data of Holmqvist and Wiedling (HO69) and Becker et al. (BE66) for Cu at 2.47 and 3.2 MeV.

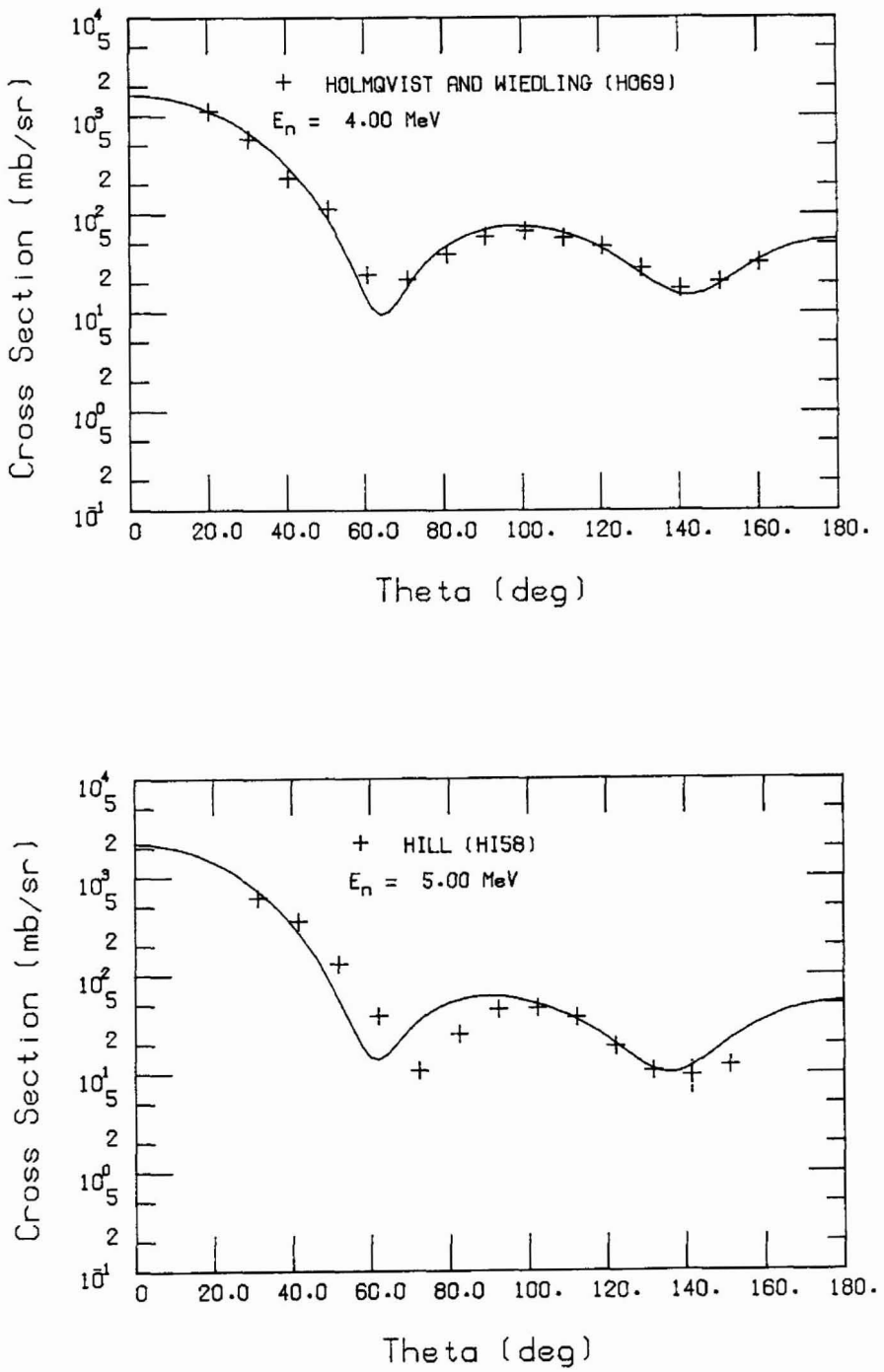

Fig. 3. Comparison of final optical-model fit with data of Holmqvist and Wiedling (H069) and Hill (HI58) for Cu at 4.0 and 5.0 MeV.

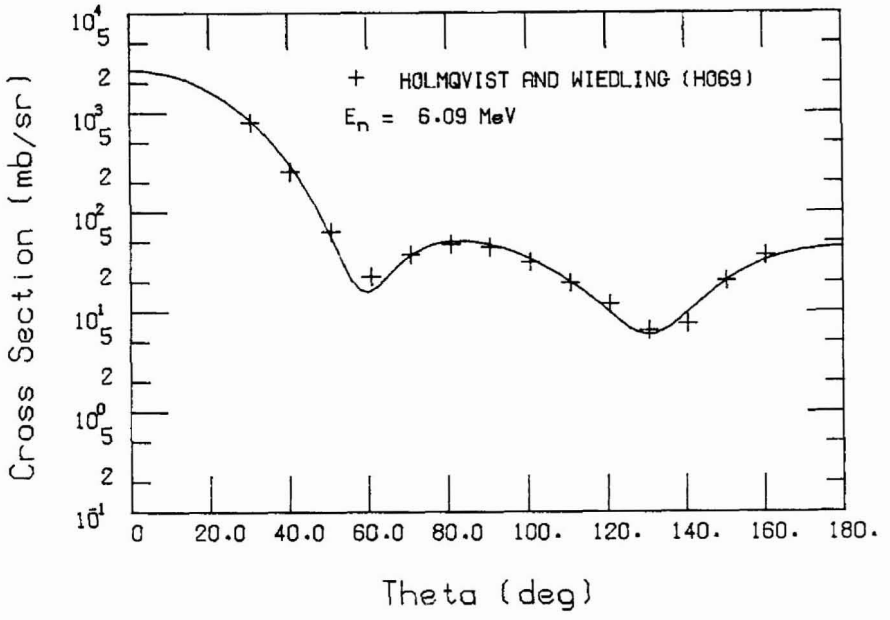

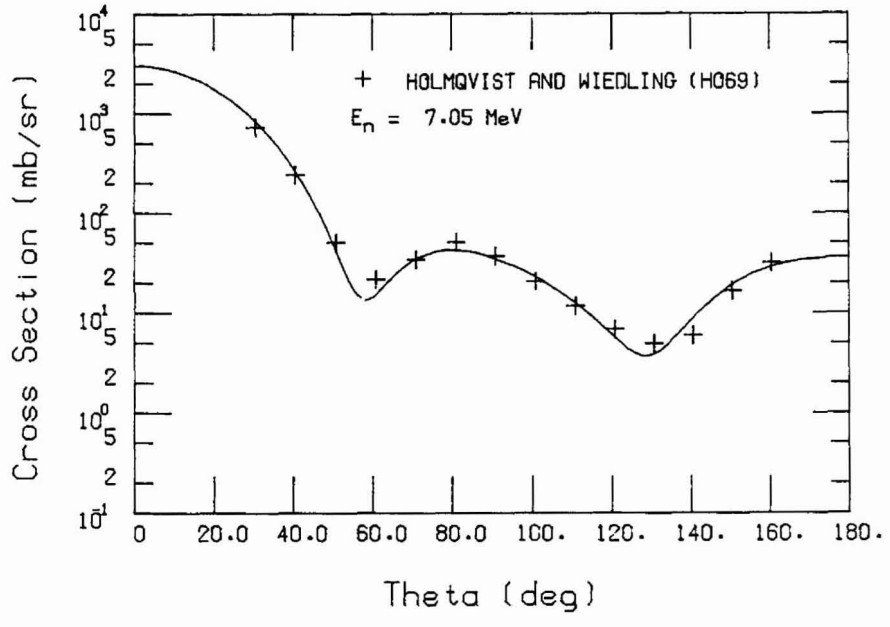

Fig. 4. Comparison of final optical-model fit with data of Holmqvist and Wiedling (H069) for Cu at 6.09 and 7.05 MeV.

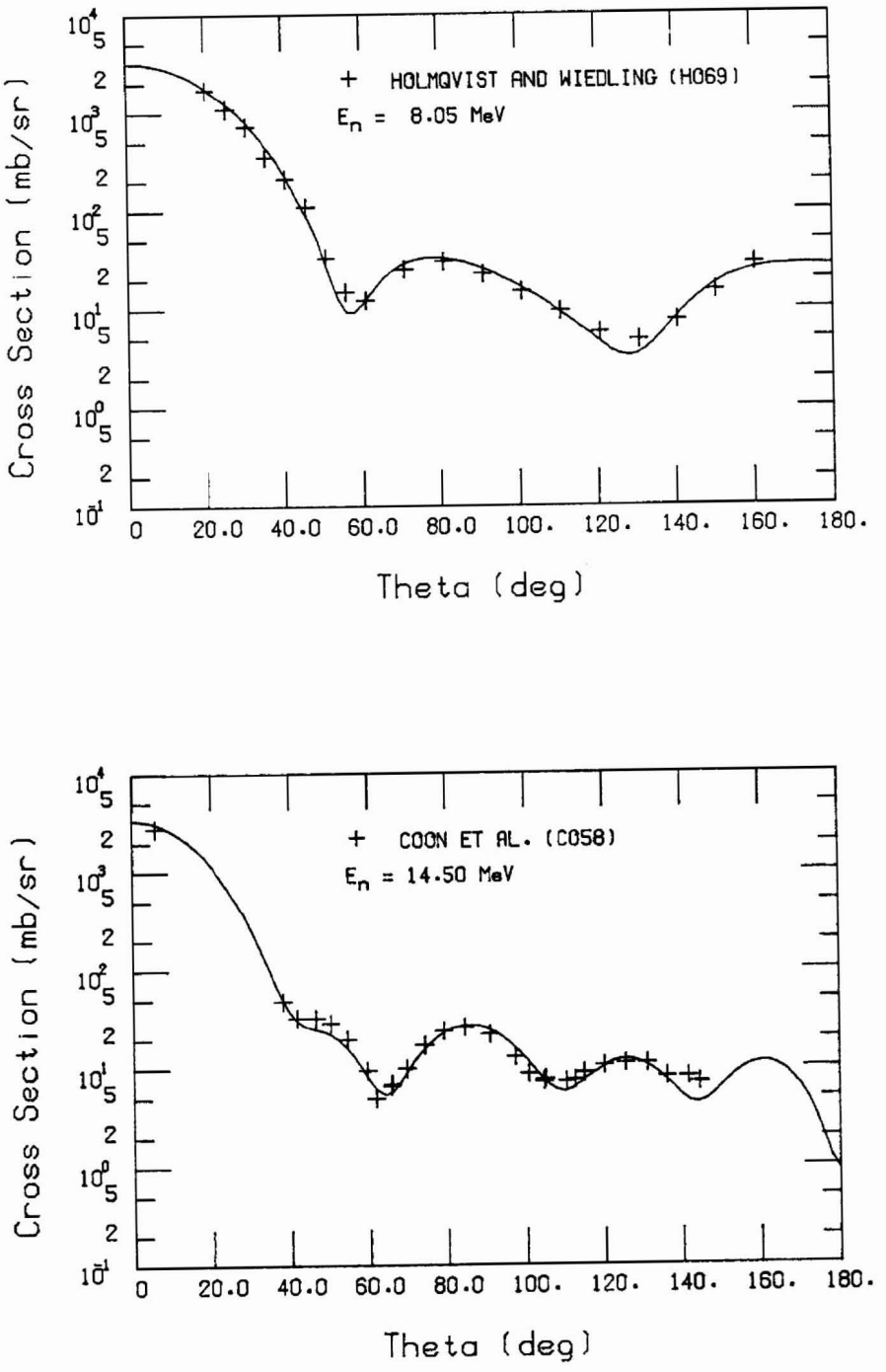

Fig. 5. Comparison of final optical-model fit with data of Holmqvist and Wiedling (H069) and Coon et al. (C058) for Cu at 8.05 and 14.5 MeV.

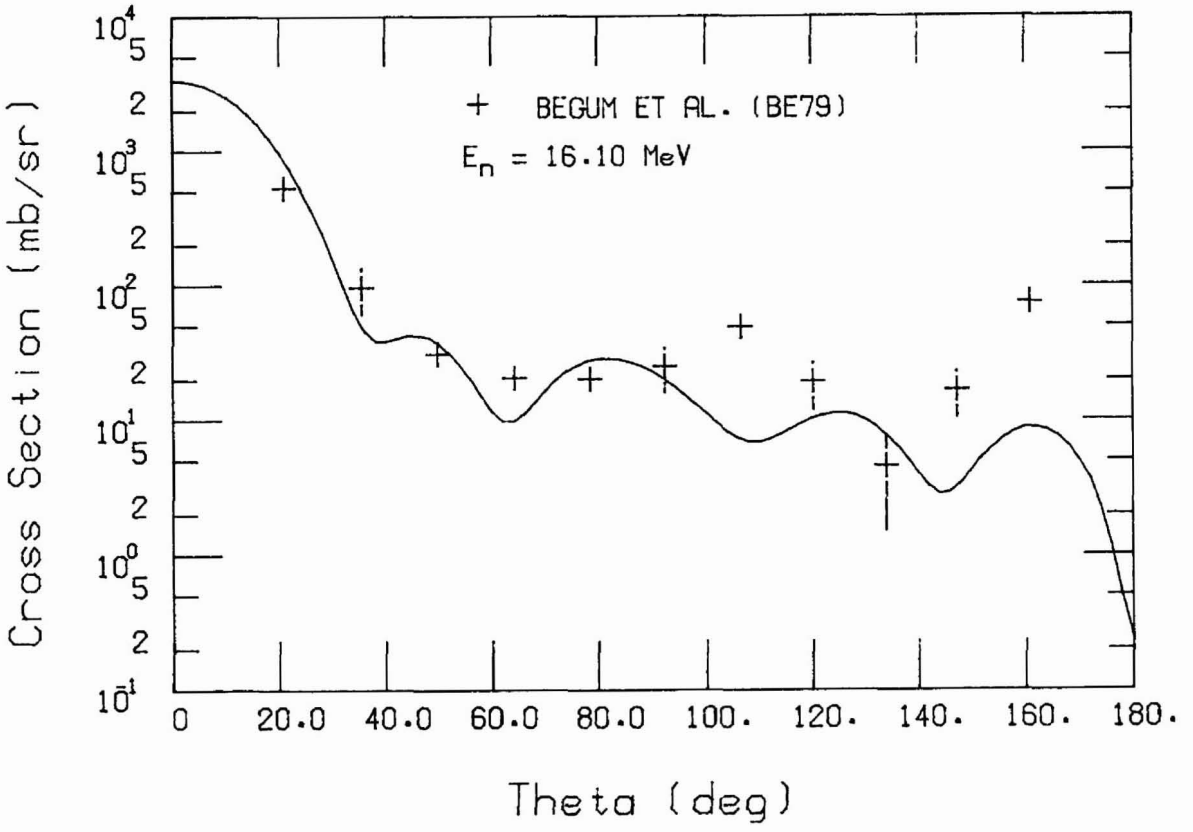

Fig. 6. Comparison of final optical-model fit with data of Begum et al. (BE79) for Cu at 16.1 MeV.

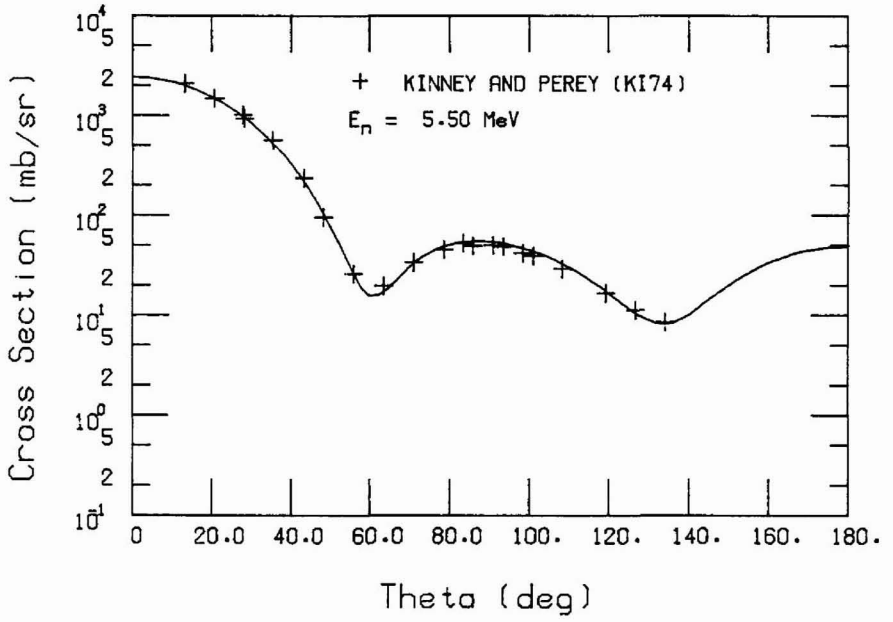

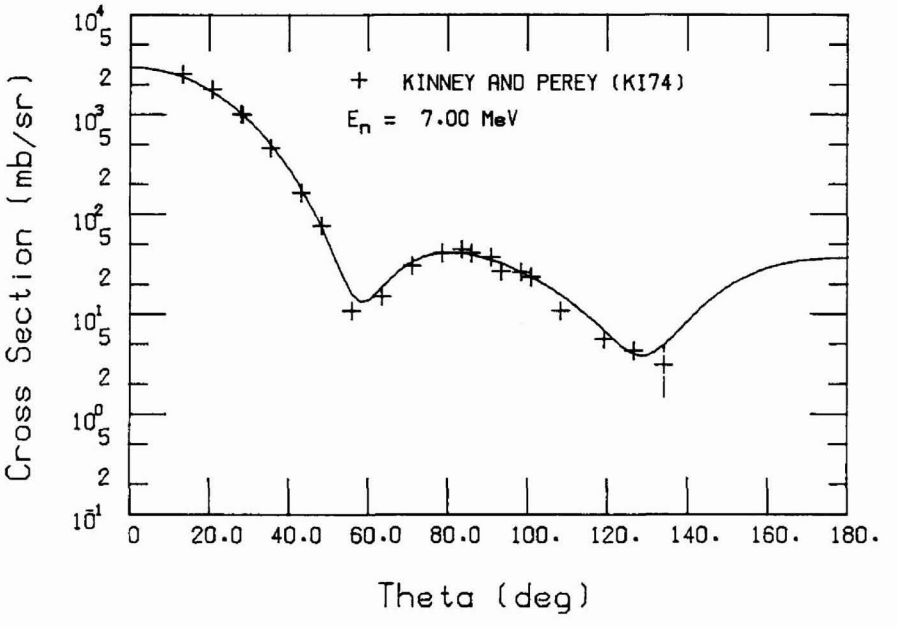

Fig. 7. Comparison of final optical-model fit with data of Kinney and Perey (KI74) for ^{63}Cu at 5.5 and 7.0 MeV.

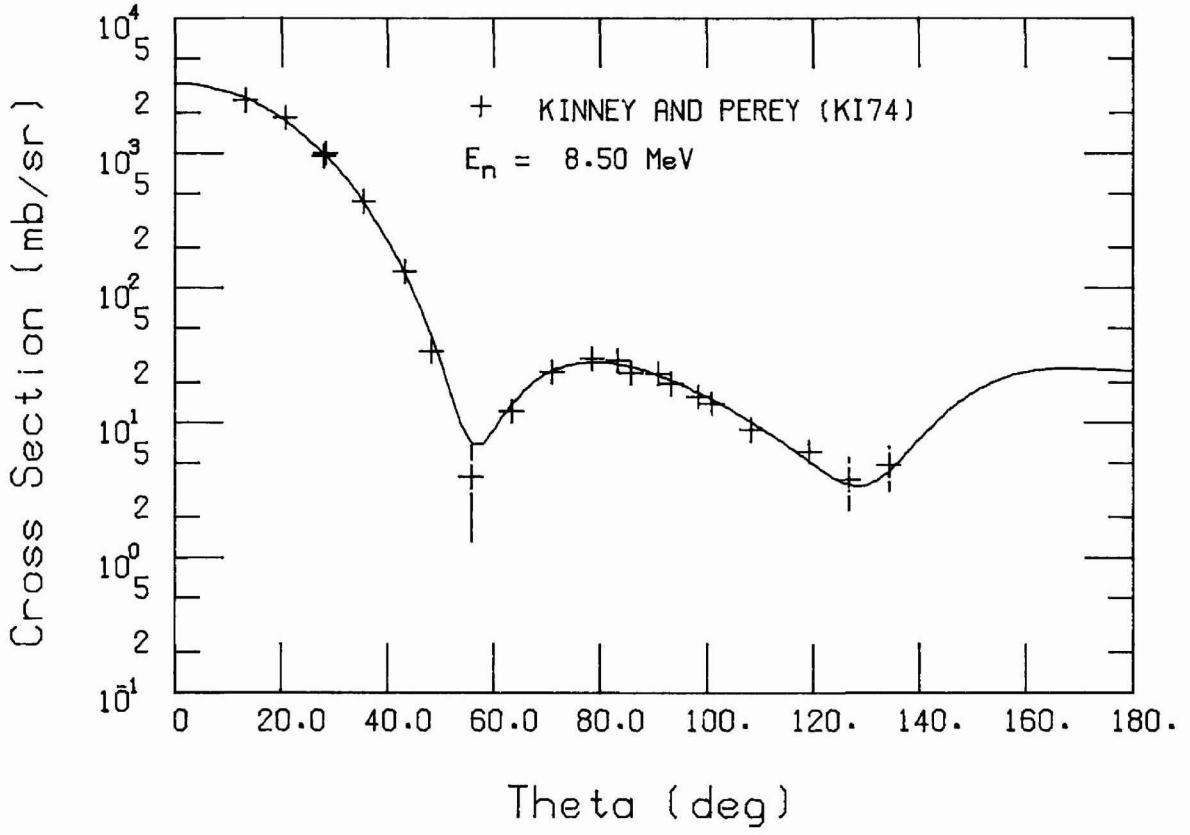

Fig. 8. Comparison of final optical-model fit with data of Kinney and Perey (KI74) for ^{63}Cu at 8.5 MeV.

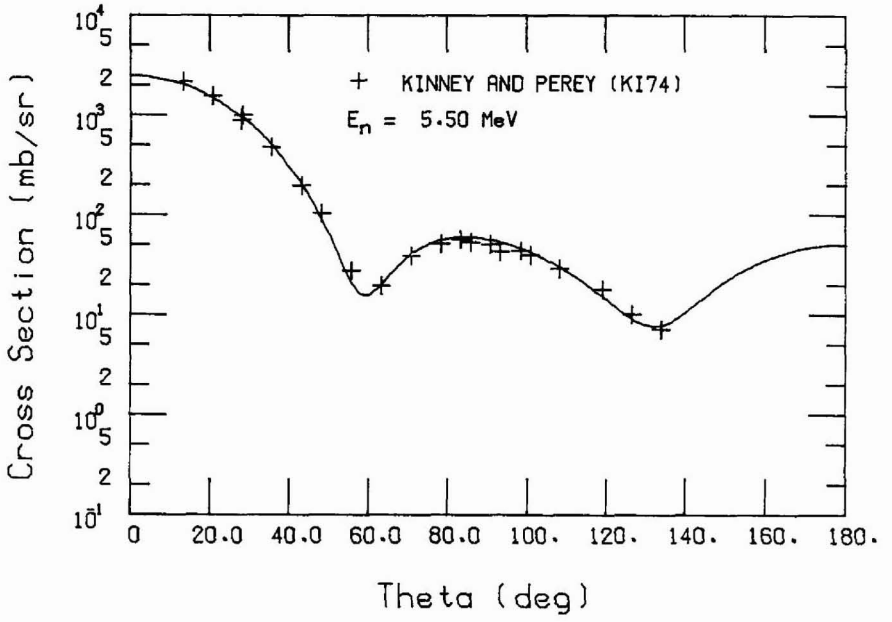

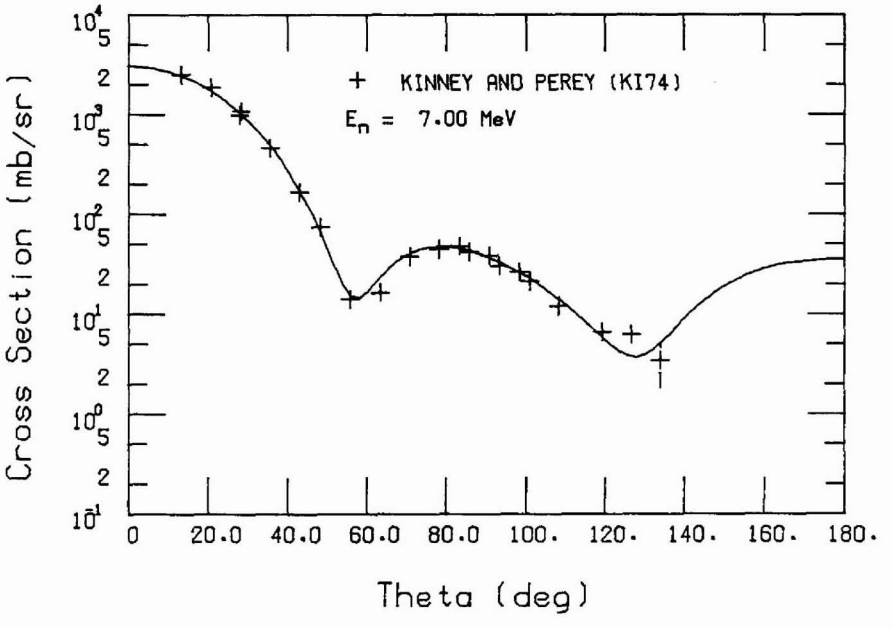

Fig. 9. Comparison of final optical-model fit with data of Kinney and Perey (KI74) for ^{65}Cu at 5.5 and 7.0 MeV.

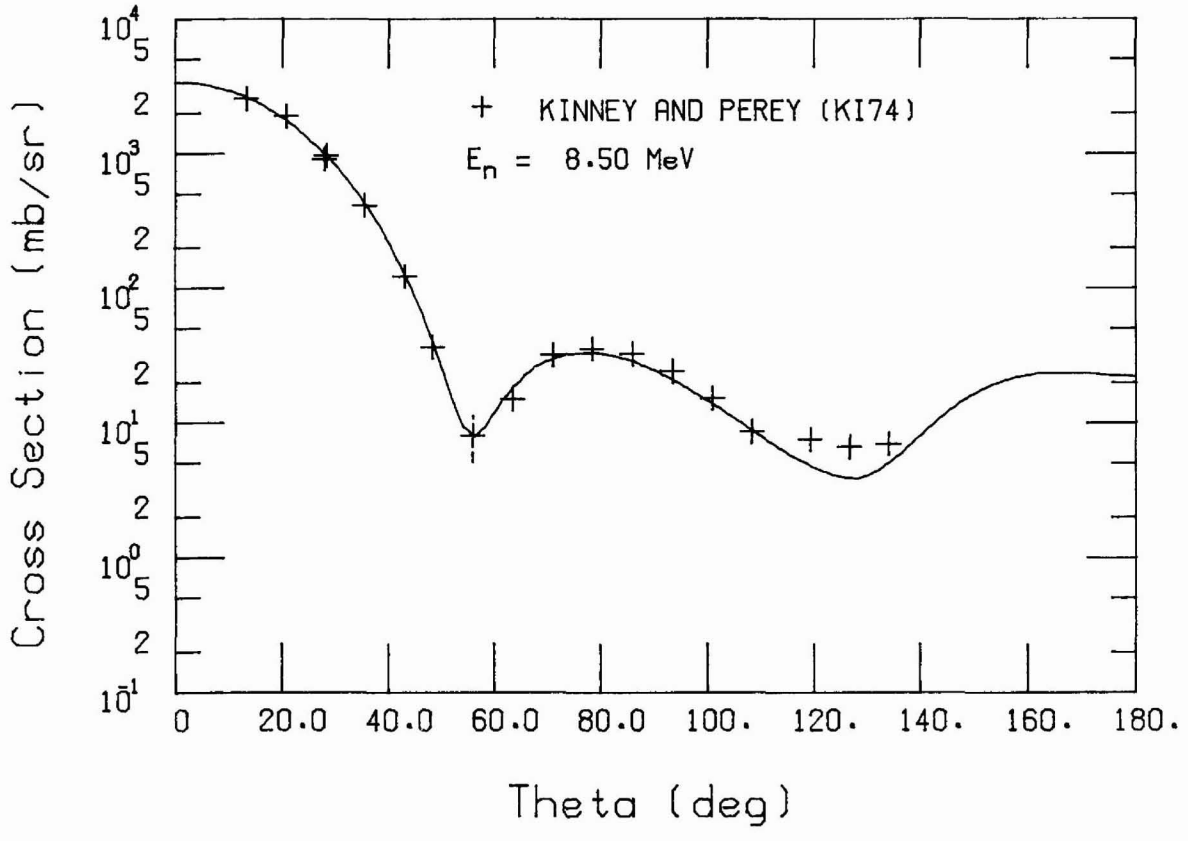

Fig. 10. Comparison of final optical-model fit with data of Kinney and Perey (KI74) for ^{65}Cu at 8.5 MeV.

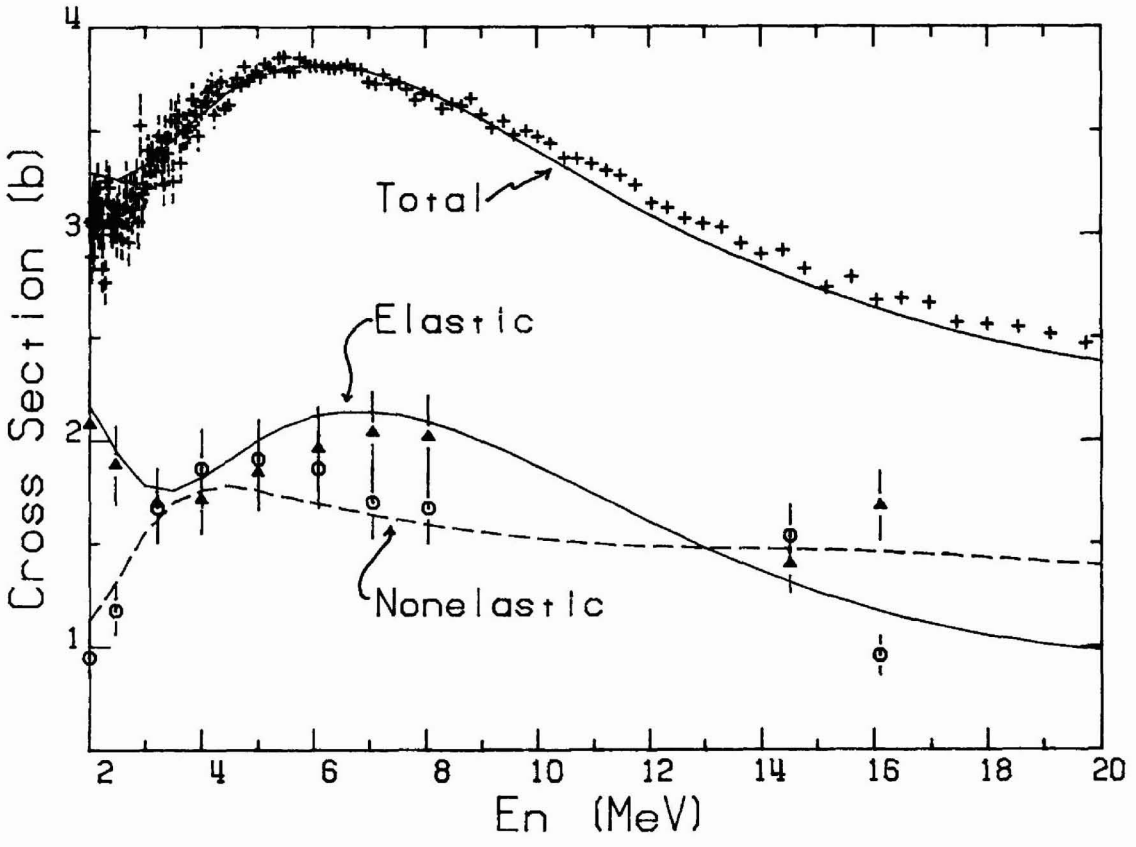

Fig. 11. Comparison of calculated Cu cross sections from optical-model analyses with data of Walt and Barschall (WA54), Holmqvist and Wiedling (HO69), Becker et al. (BE66), Hill (HI58), Coon et al. (CO58), and Begum et al. (BE79) for elastic and nonelastic, and Larson (LA80) for total.

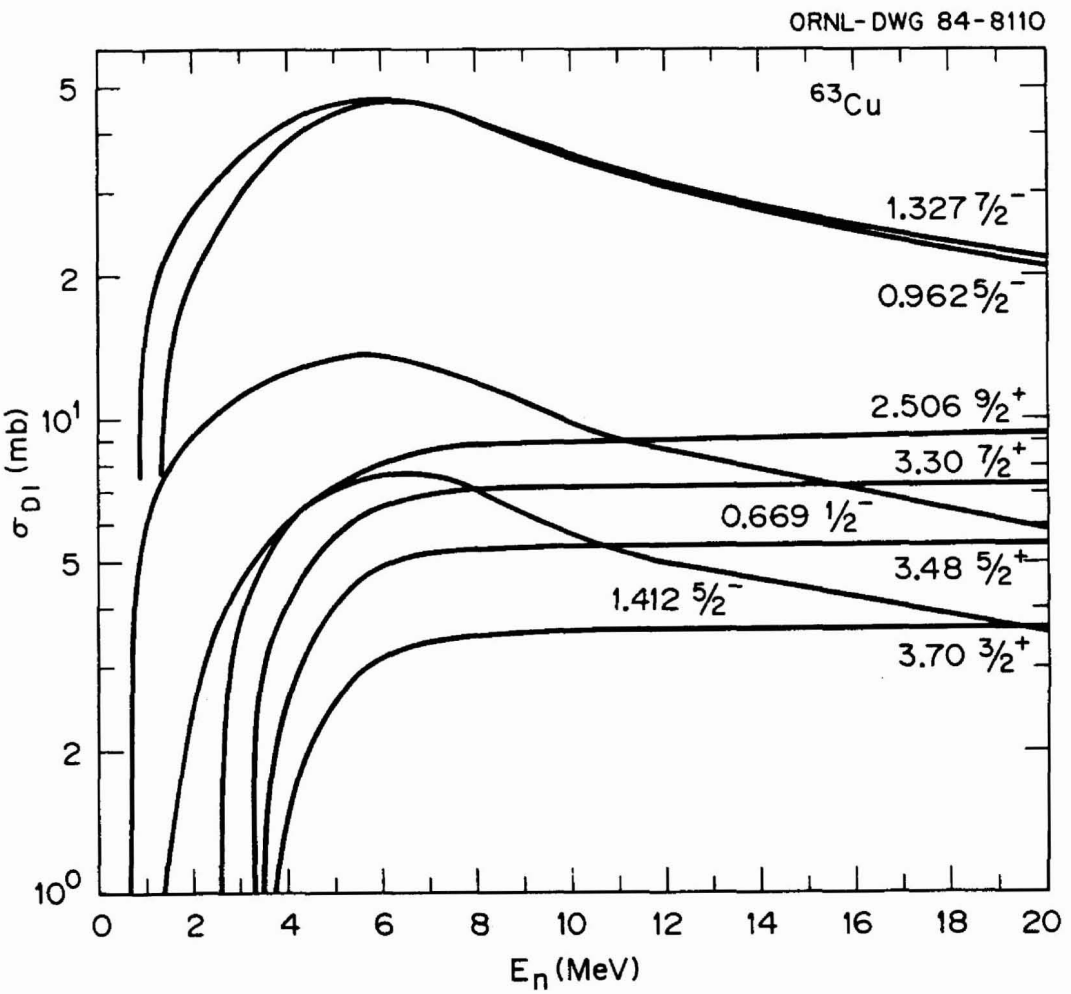

Fig. 12. Calculated direct inelastic excitation cross sections for ^{63}Cu.

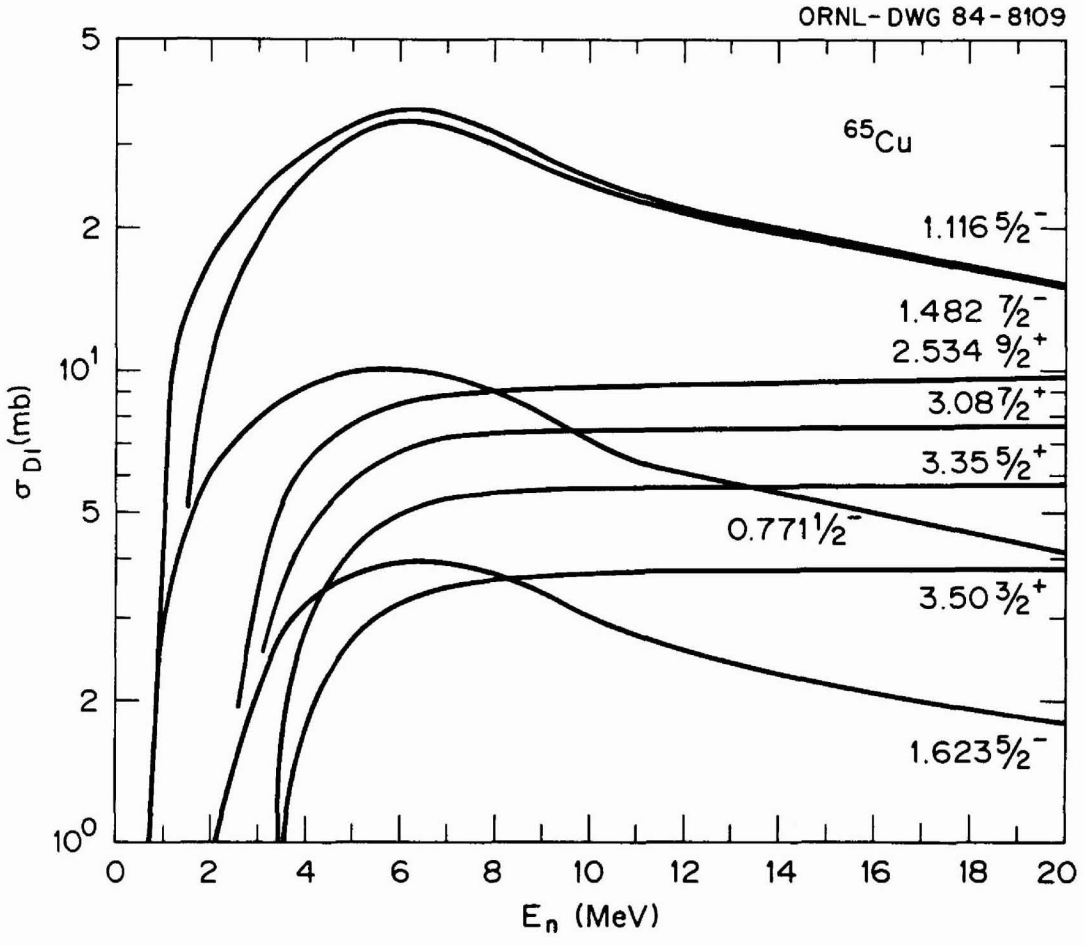

Fig. 13. Calculated direct inelastic excitation cross sections for ^{65}Cu.

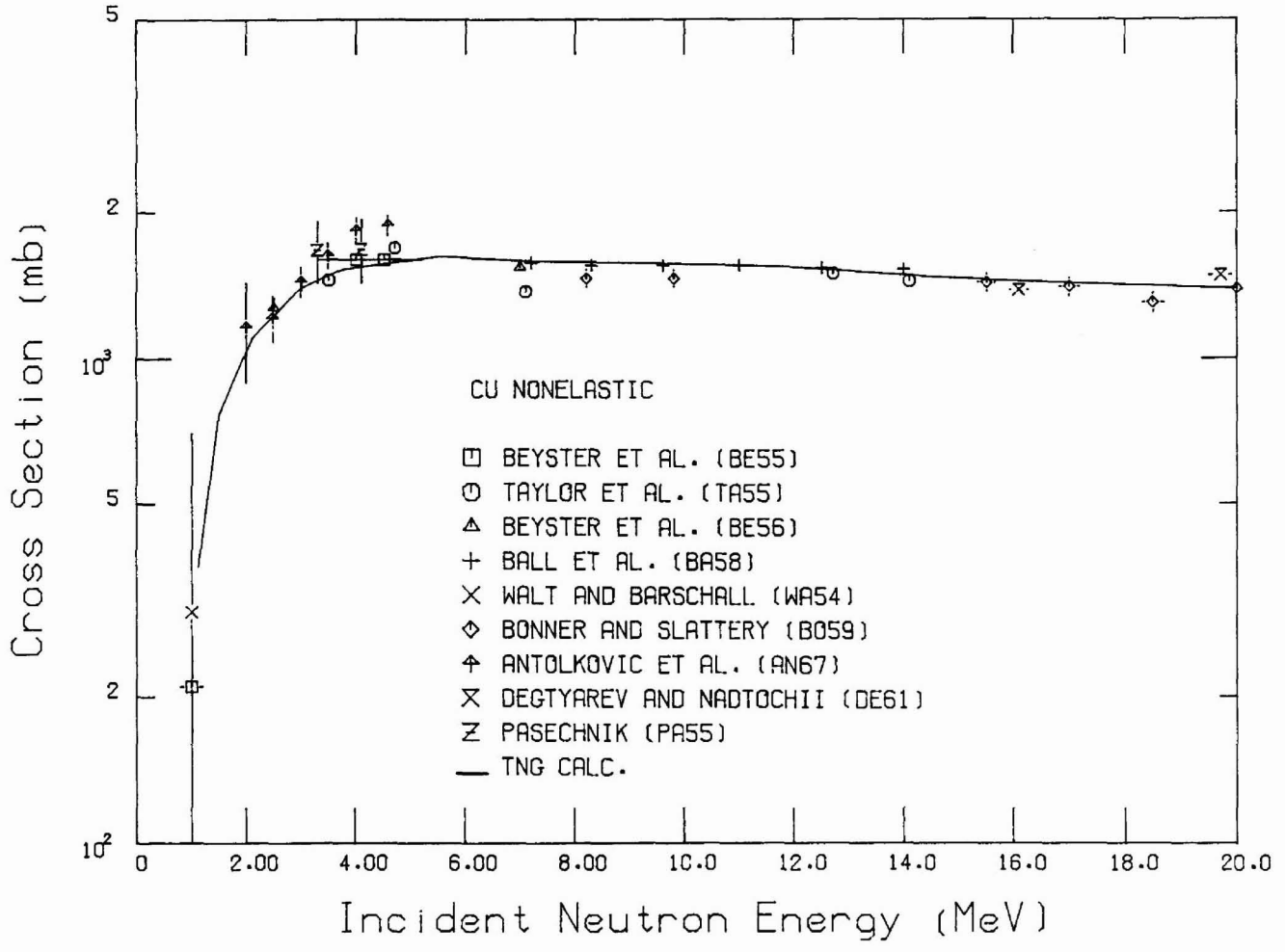

Fig. 14. Comparison of calculated and experimental nonelastic cross sections for Cu.

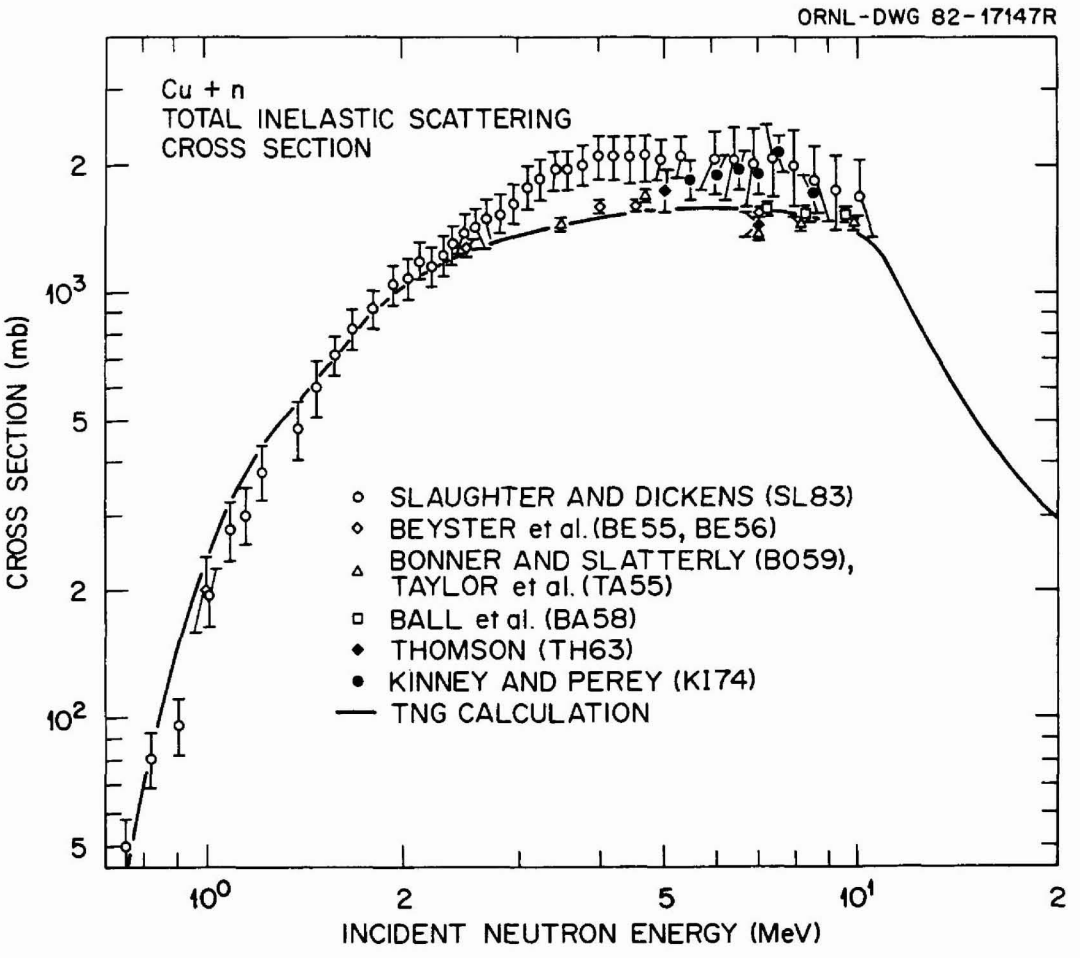

Fig. 15. Comparison of calculated and experimental total inelastic scattering cross sections for Cu.

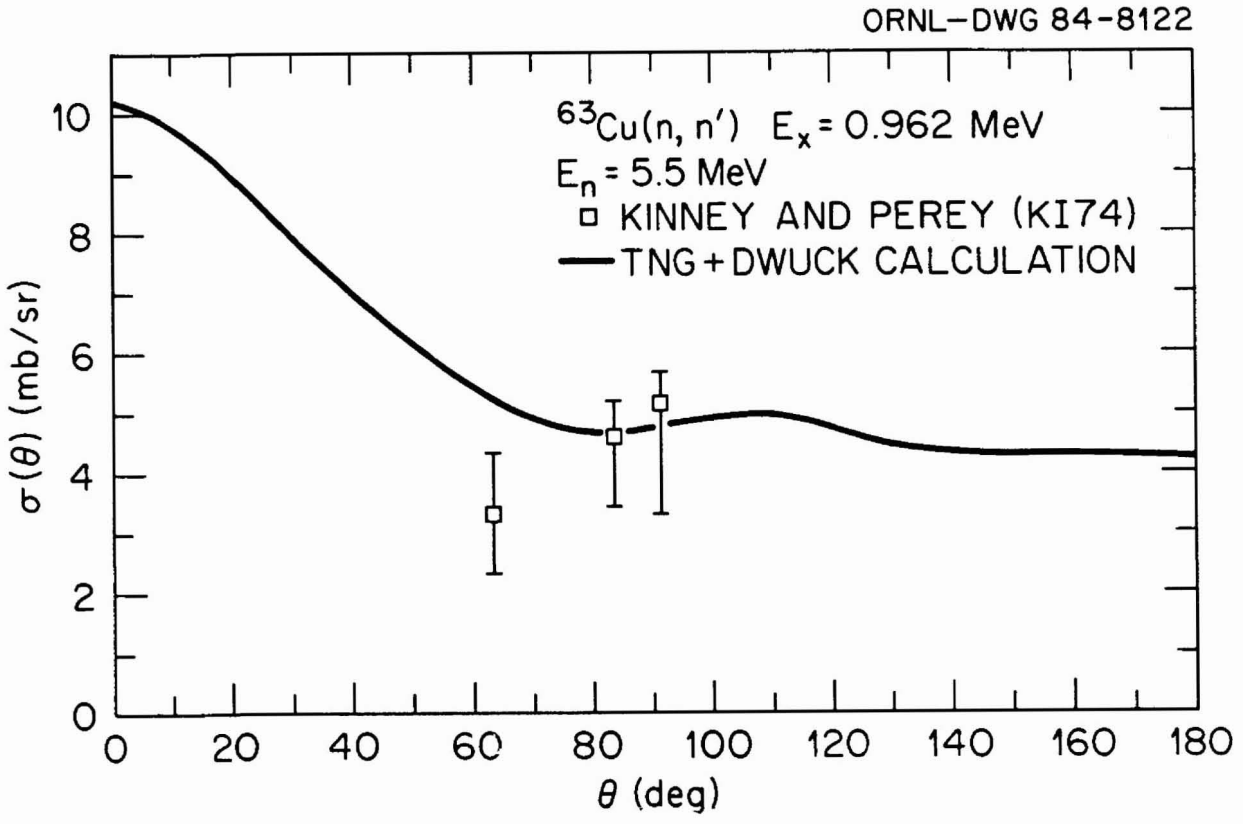

Fig. 16. Comparison of calculated and experimental differential cross sections for exciting the 0.962-MeV level at E_n=5.5 MeV.

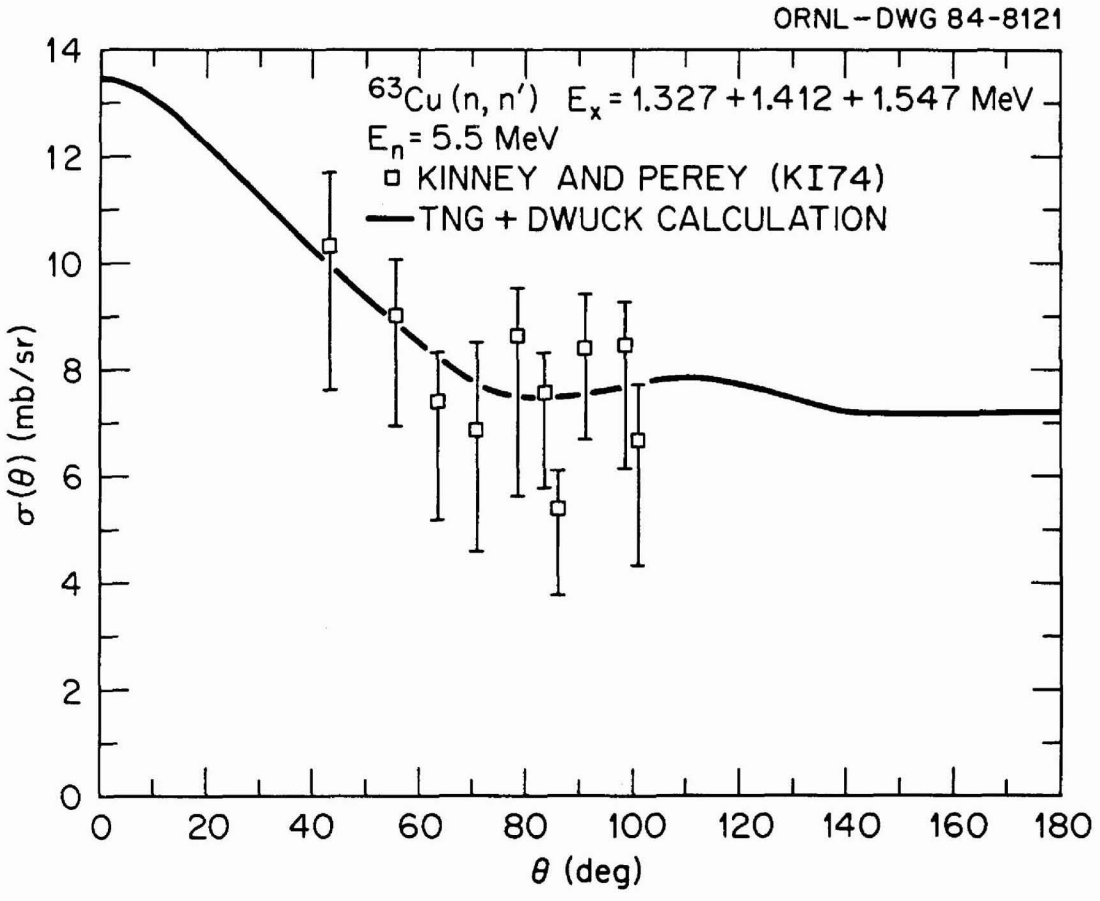

Fig. 17. Comparison of calculated and experimental differential cross sections for exciting the 1.327-, 1.412-, and 1.547-MeV levels at E_n=5.5 MeV.

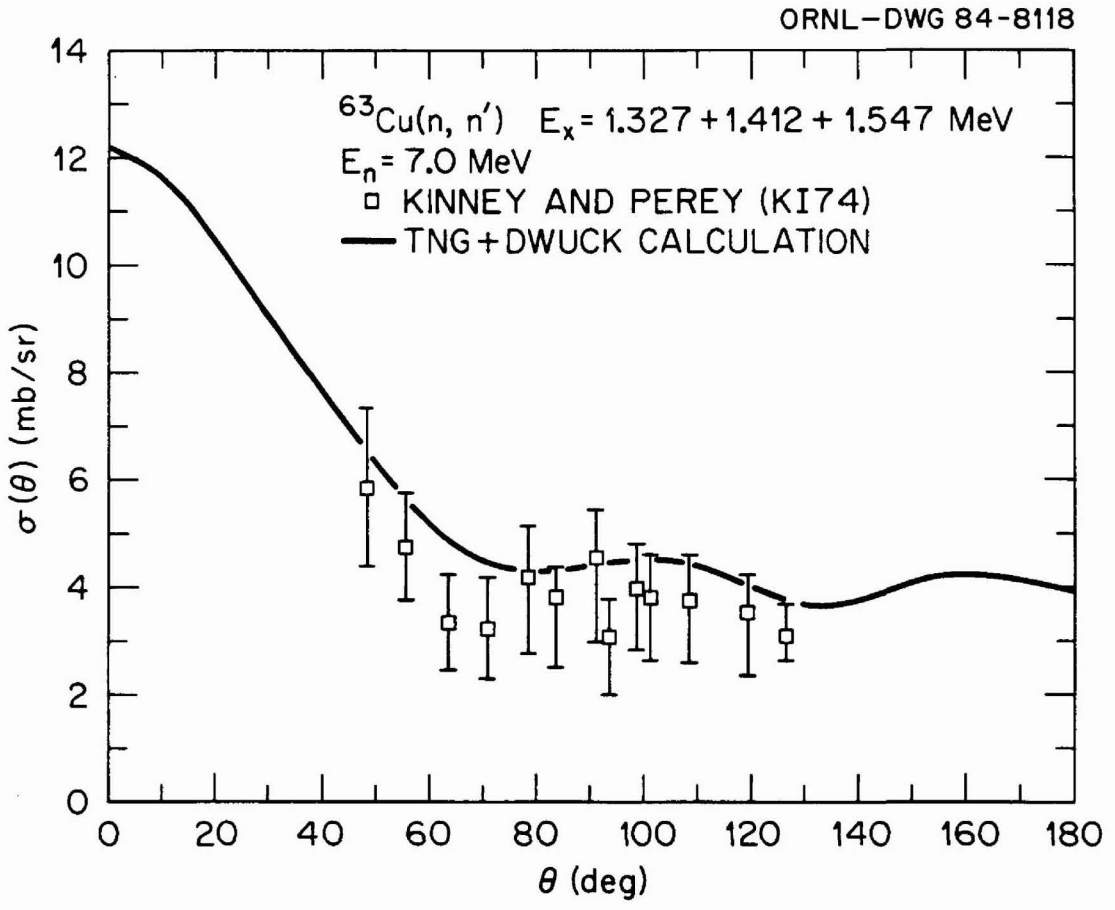

Fig. 18. Comparison of calculated and experimental differential cross sections for exciting the 1.327-, 1.412-, and 1.547-MeV levels at E_n=7.0 MeV.

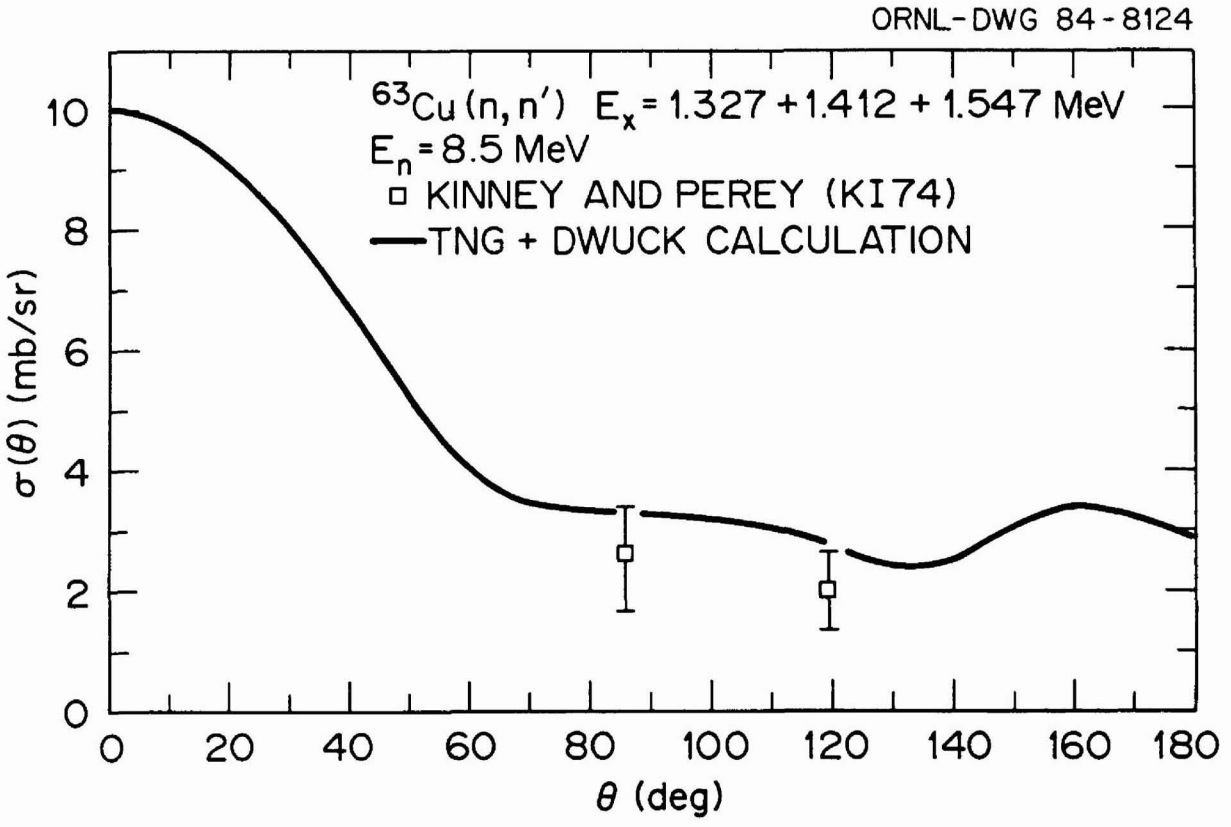

Fig. 19. Comparison of calculated and experimental differential cross sections for exciting the 1.327-, 1.412-, and 1.547-MeV levels at E_n=8.5 MeV.

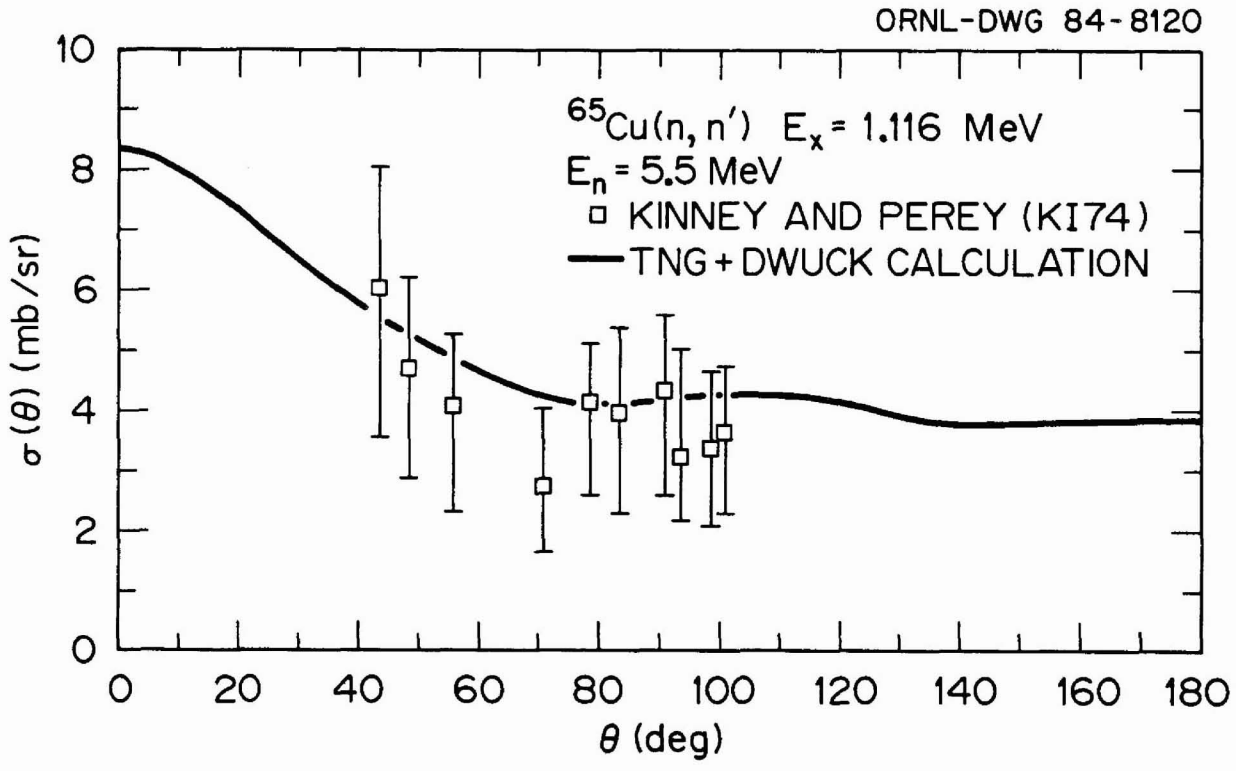

Fig. 20. Comparison of calculated and experimental differential cross sections for exciting the 1.116-MeV level at E_n=5.5 MeV.

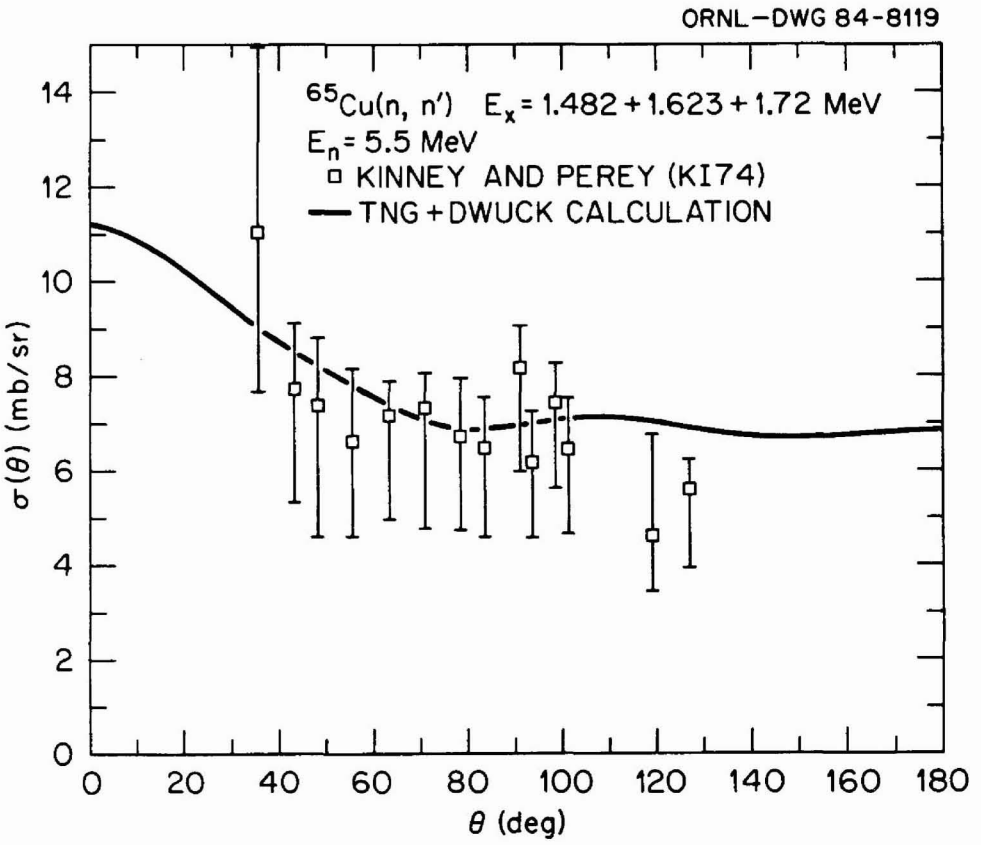

Fig. 21. Comparison of calculated and experimental differential cross sections for exciting the 1.482-, 1.623-, and 1.72-MeV levels at E_n=5.5 MeV.

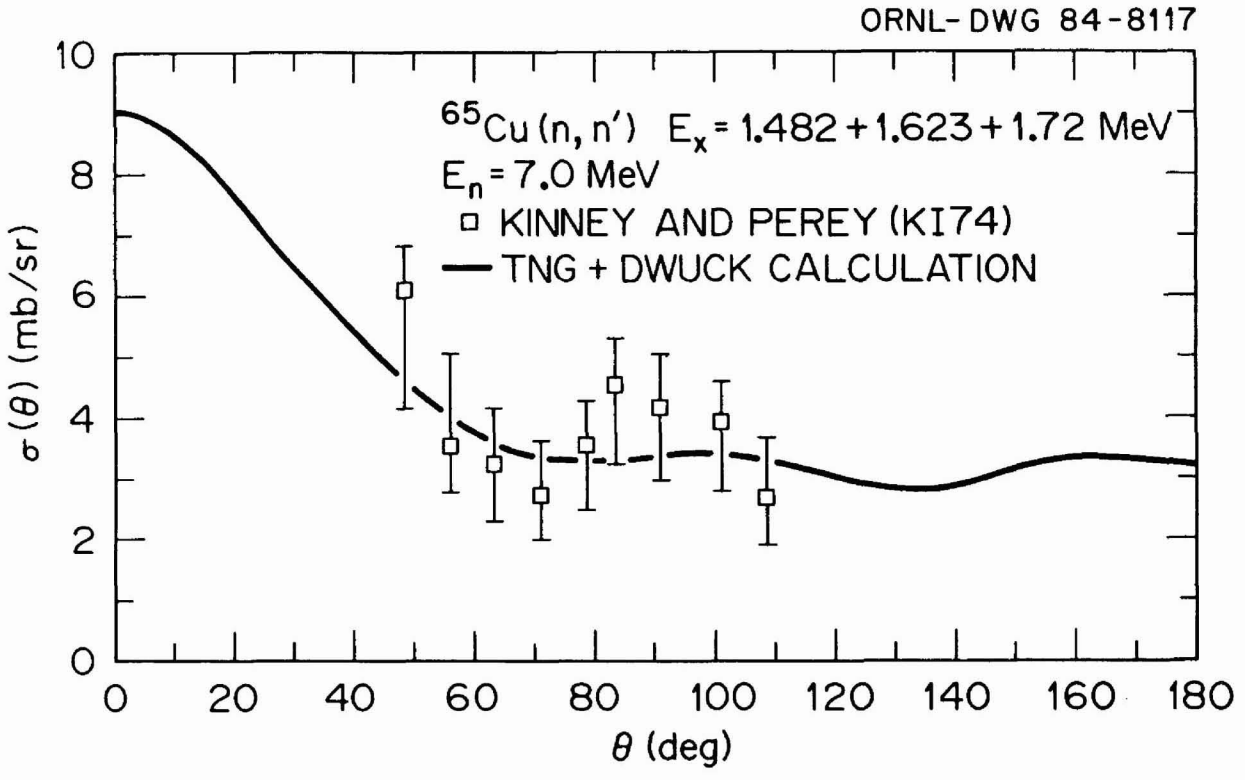

Fig. 22. Comparison of calculated and experimental differential cross sections for exciting the 1.482-, 1.623-, and 1.72-MeV levels at E_n=7.0 MeV.

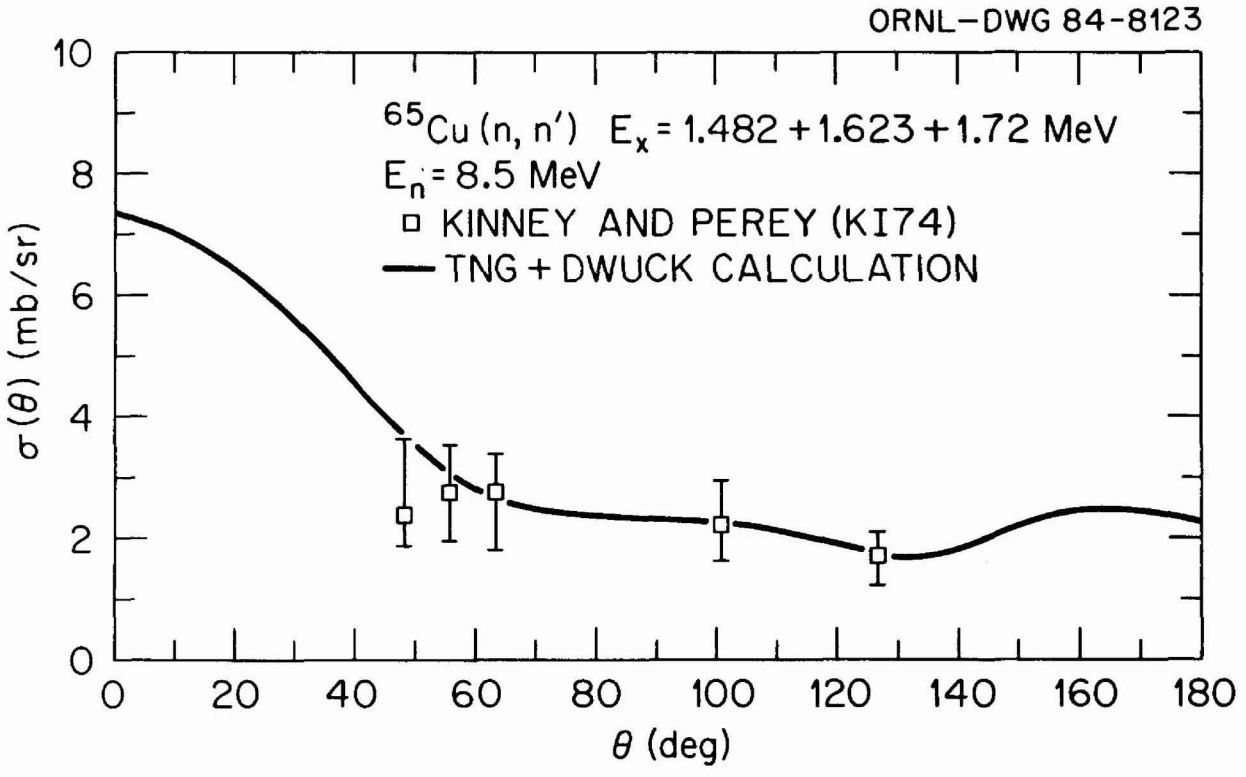

Fig. 23. Comparison of calculated and experimental differential cross sections for exciting the 1.482-, 1.623-, and 1.72-MeV levels at E_n=8.5 MeV.

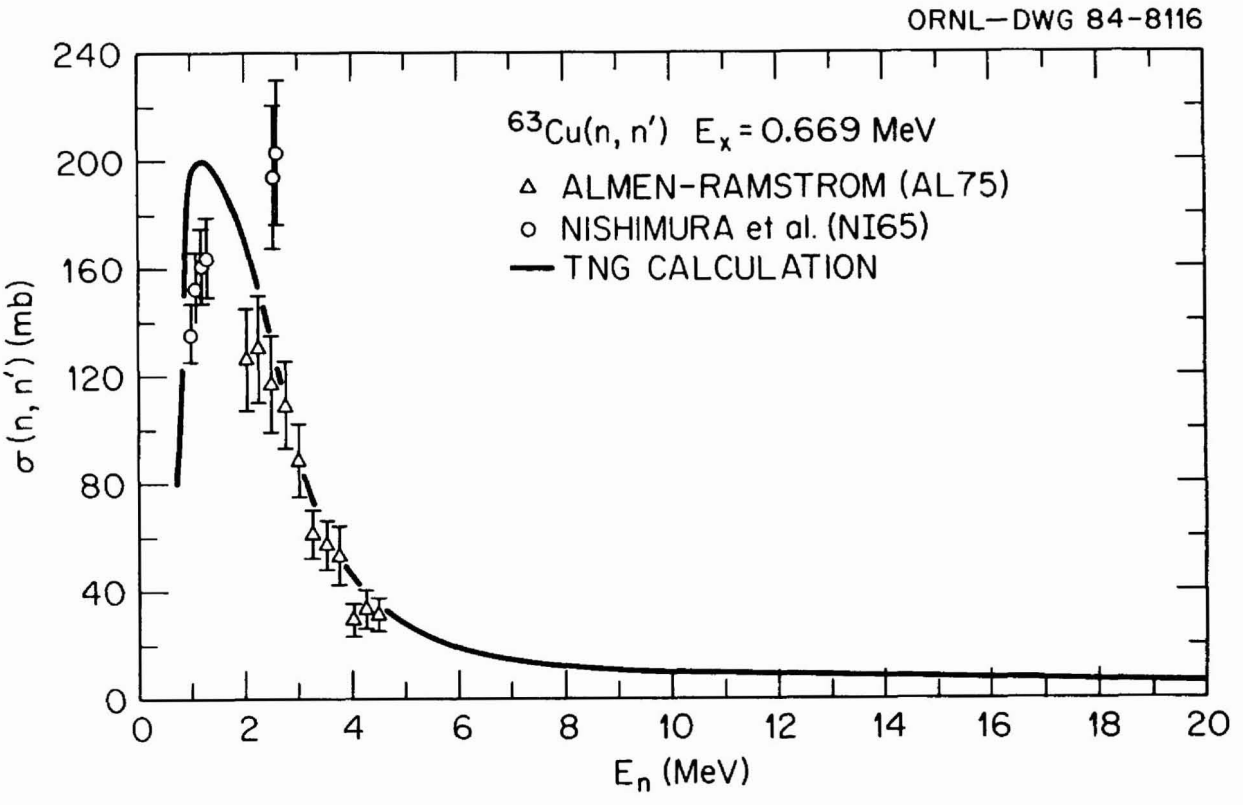

Fig. 24. Comparison of calculated and experimental ^{63}Cu(n,n') cross sections for exciting the 0.669-MeV level.

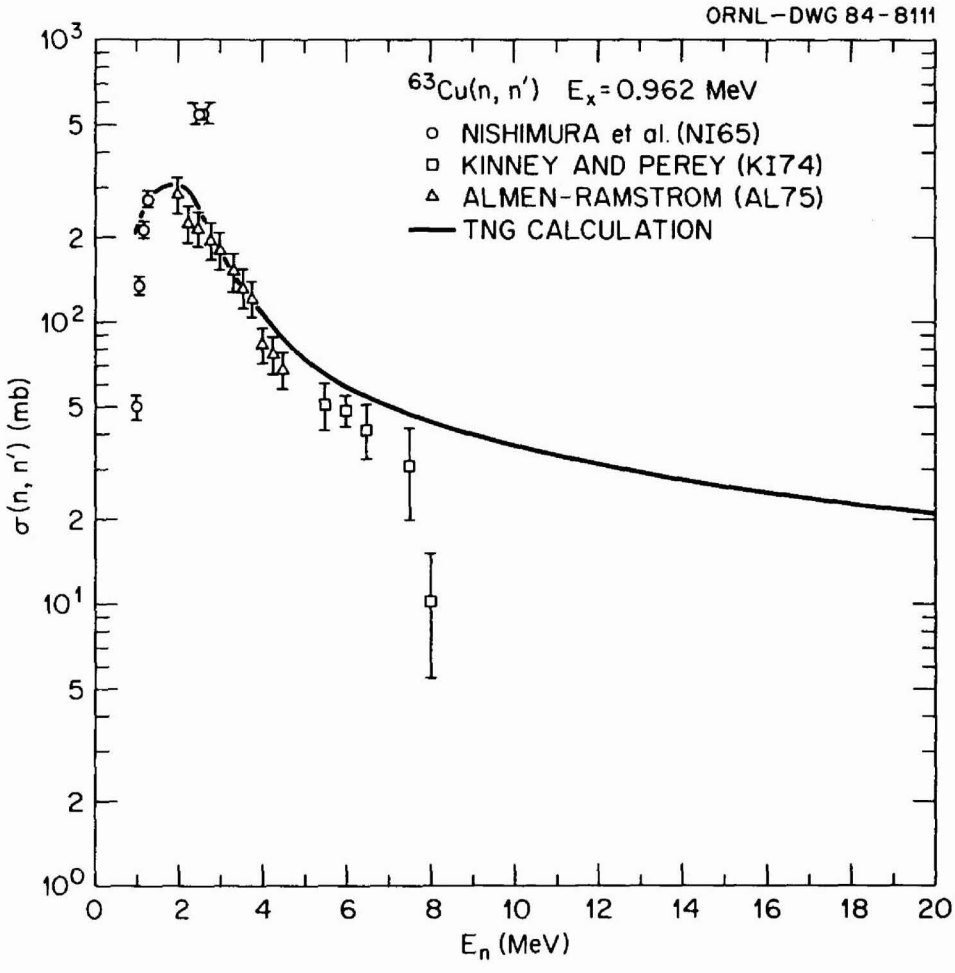

Fig. 25. Comparison of calculated and experimental ^{63}Cu(n,n') cross sections for exciting the 0.962-MeV level.

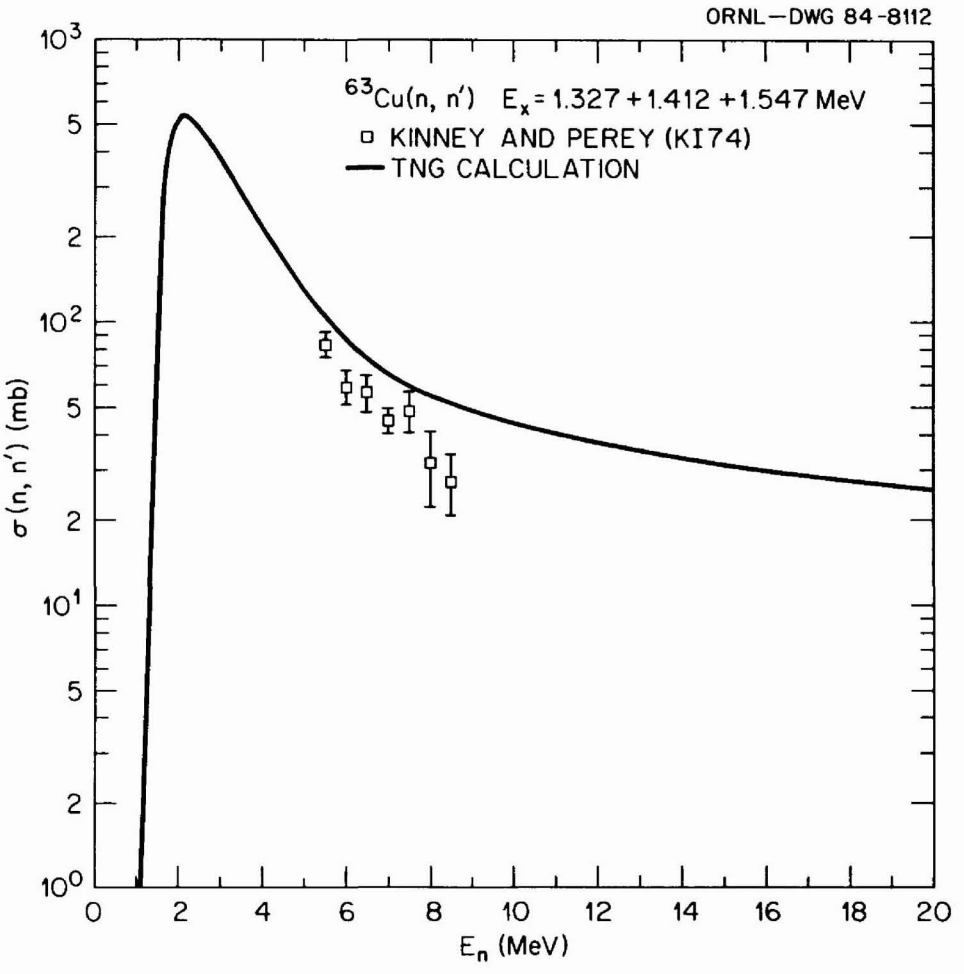

Fig. 26. Comparison of calculated and experimental ^{63}Cu(n,n') cros sections for exciting the 1.327-, 1.412-, and 1.547-MeV levels.

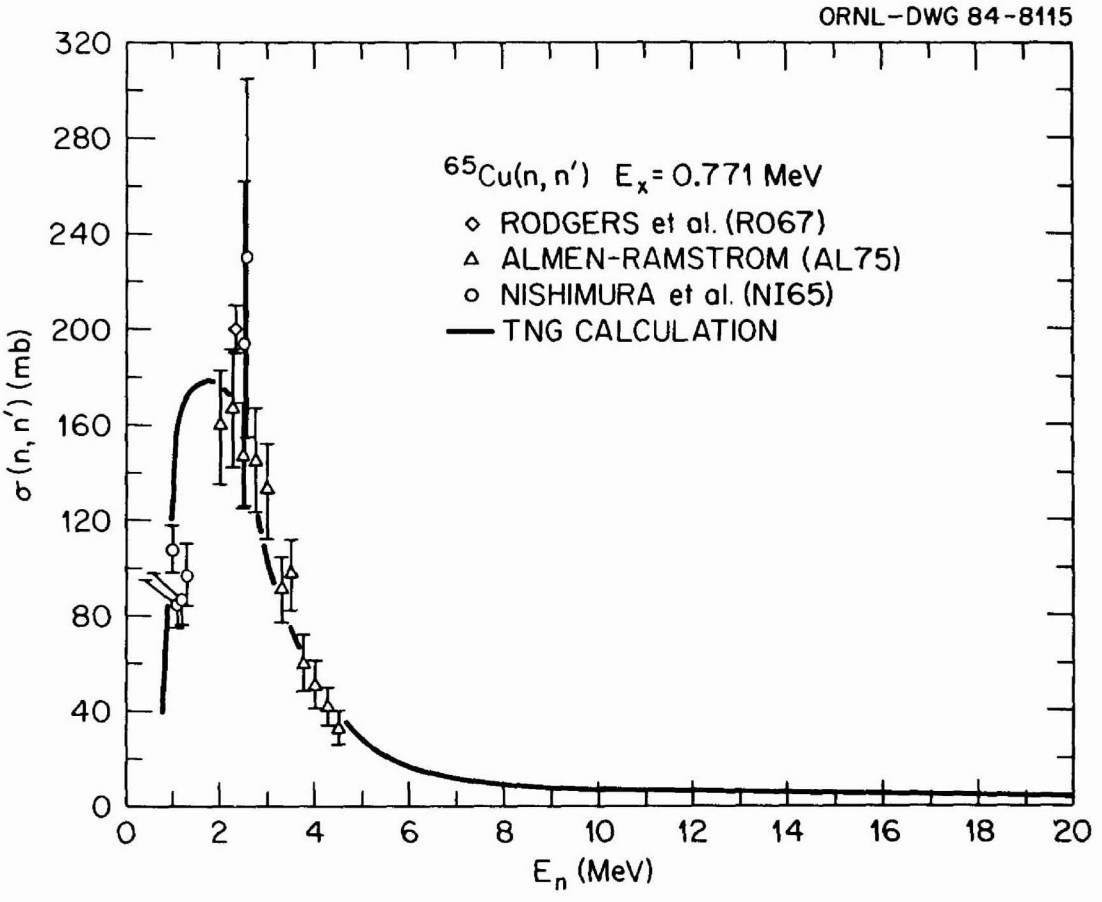

Fig. 27. Comparison of calculated and experimental ^{65}Cu(n,n') cross sections for exciting the 0.771-MeV level.

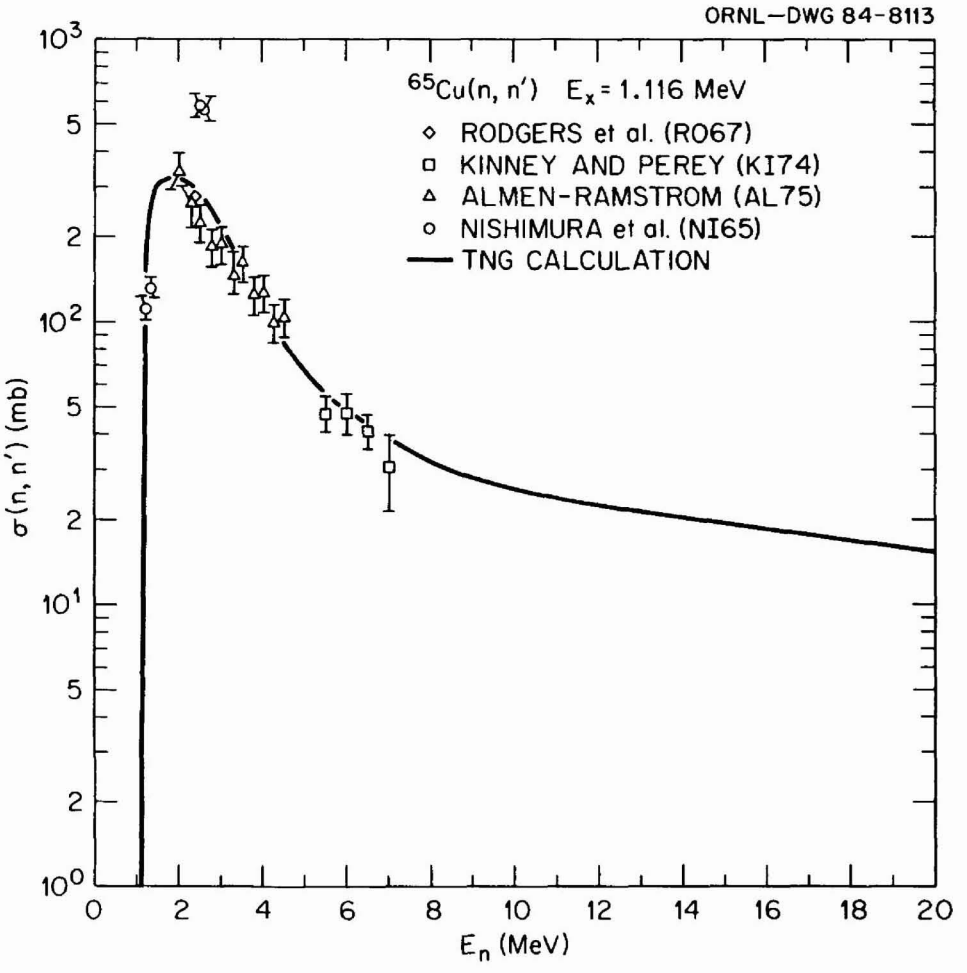

Fig. 28. Comparison of calculated and experimental ^{65}Cu(n,n') cross sections for exciting the 1.116-MeV level.

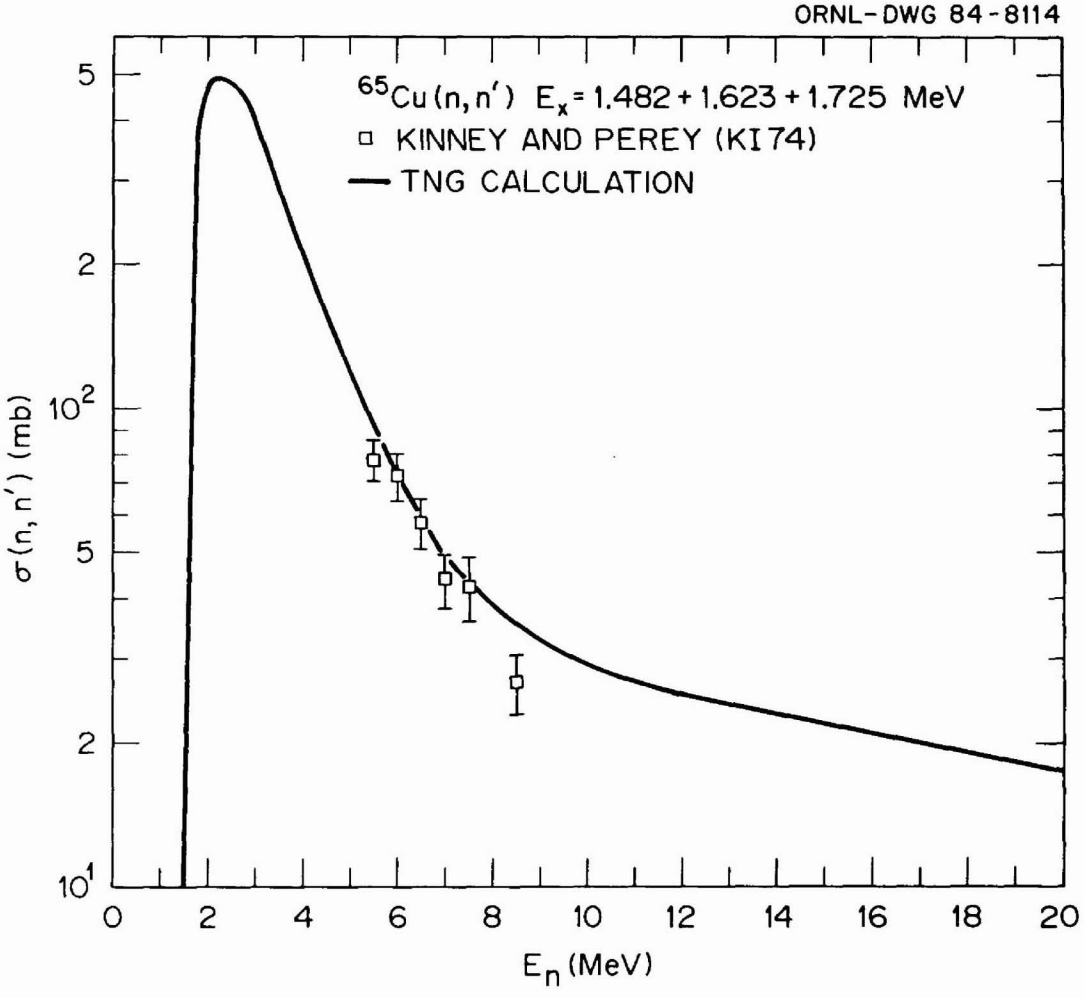

Fig. 29. Comparison of calculated and experimental ^{65}Cu(n,n') cross sections for exciting the 1.482-, 1.623-, and 1.725-MeV levels.

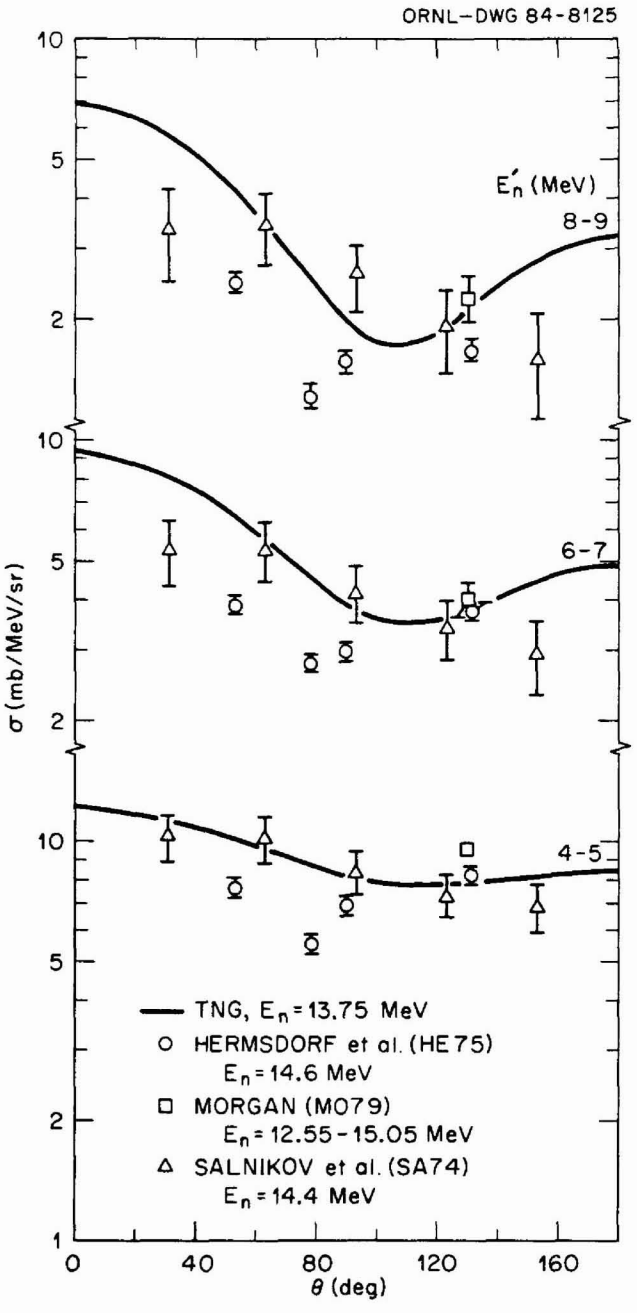

Fig. 30. Comparison of calculated and experimental neutron production cross sections.

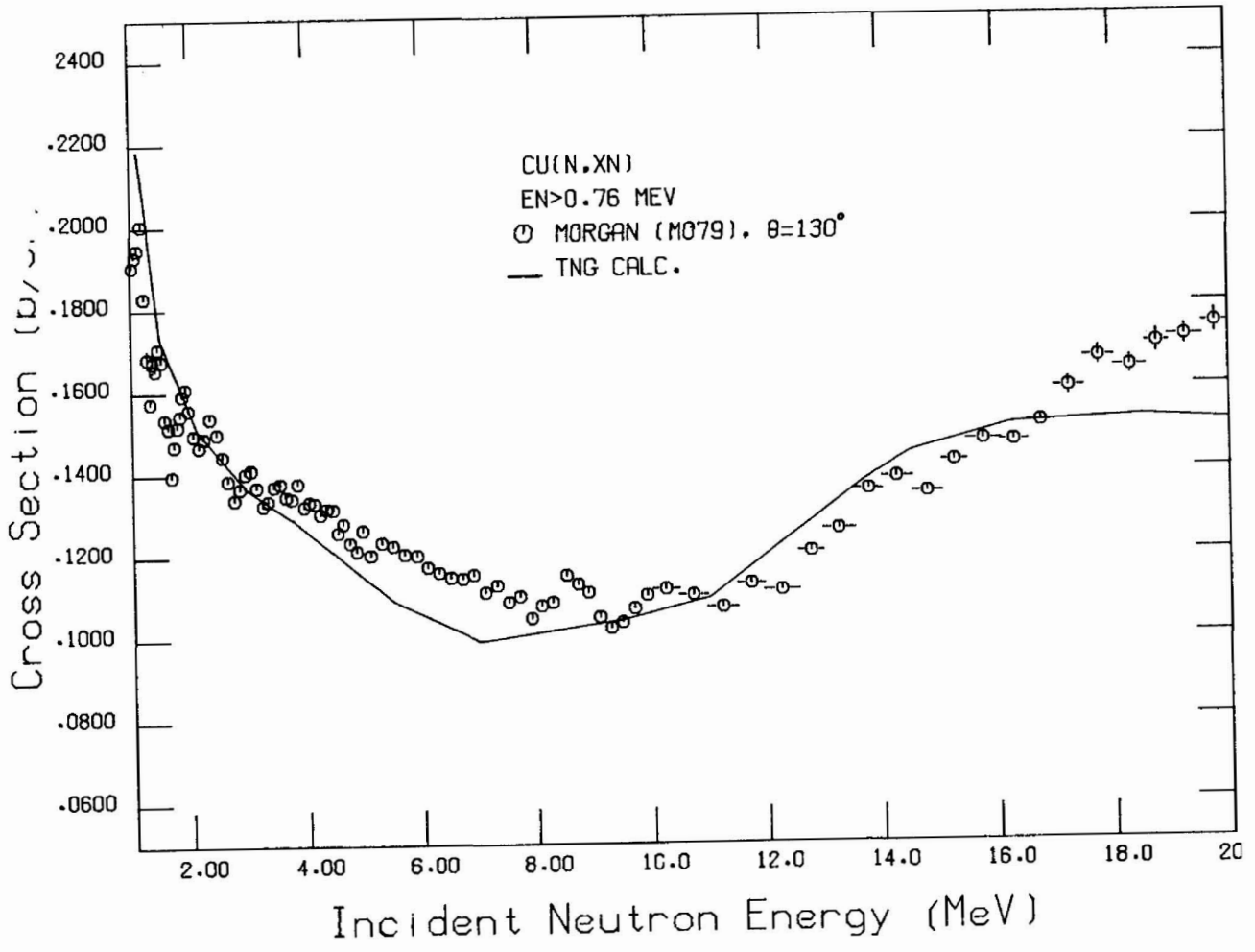

Fig. 31. Integrated yield of secondary neutrons with $E_n' > 0.76$ MeV as a function of incident neutron energy. The data of Morgan (M079) were measured at 130°, whereas the TNG code computes results for all angles.

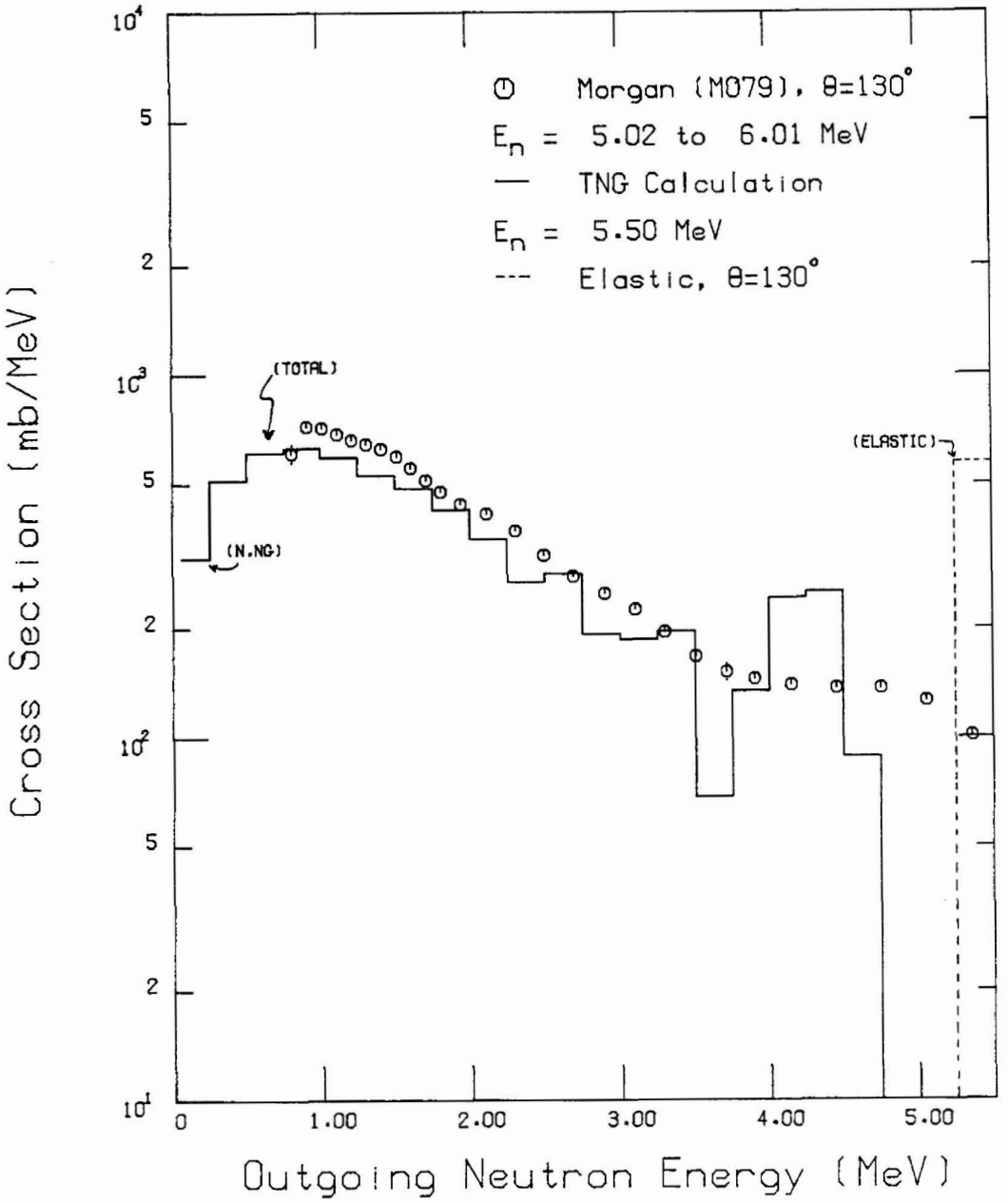

Fig. 32. Neutron emission spectra from the TNG calculation compared with the data of Morgan (M079). The calculated elastic cross section (θ=130°) is not smeared and is not in phase with the data.

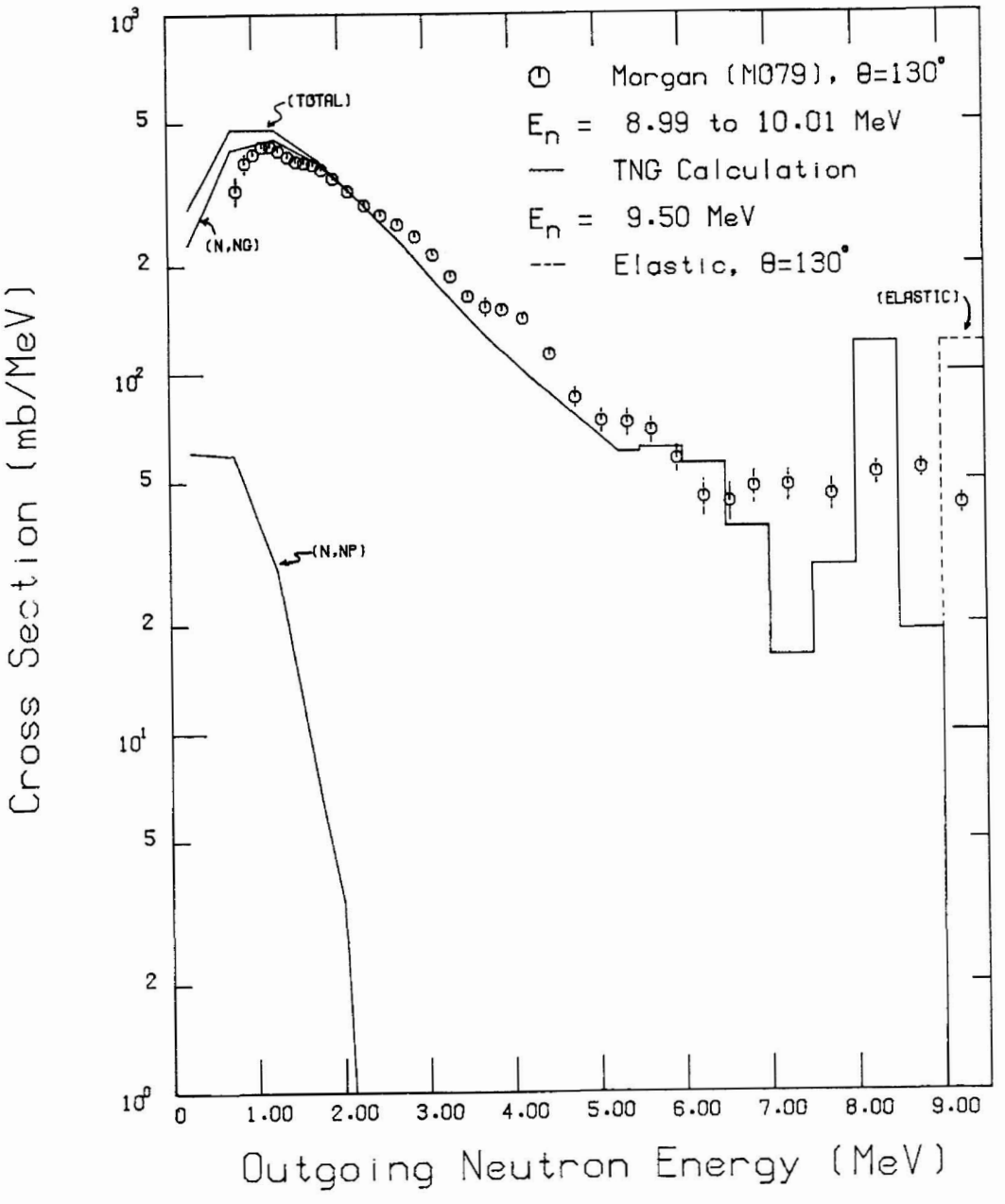

Fig. 33. Neutron emission spectra from the TNG calculation compared with the data of Morgan (M079). The calculated elastic cross section (θ=130°) is not smeared and is not in phase with the data. Contributions from the various neutron-producing components are shown (they sum to the total). The curve labeled (n,np) includes the (n,pn) component.

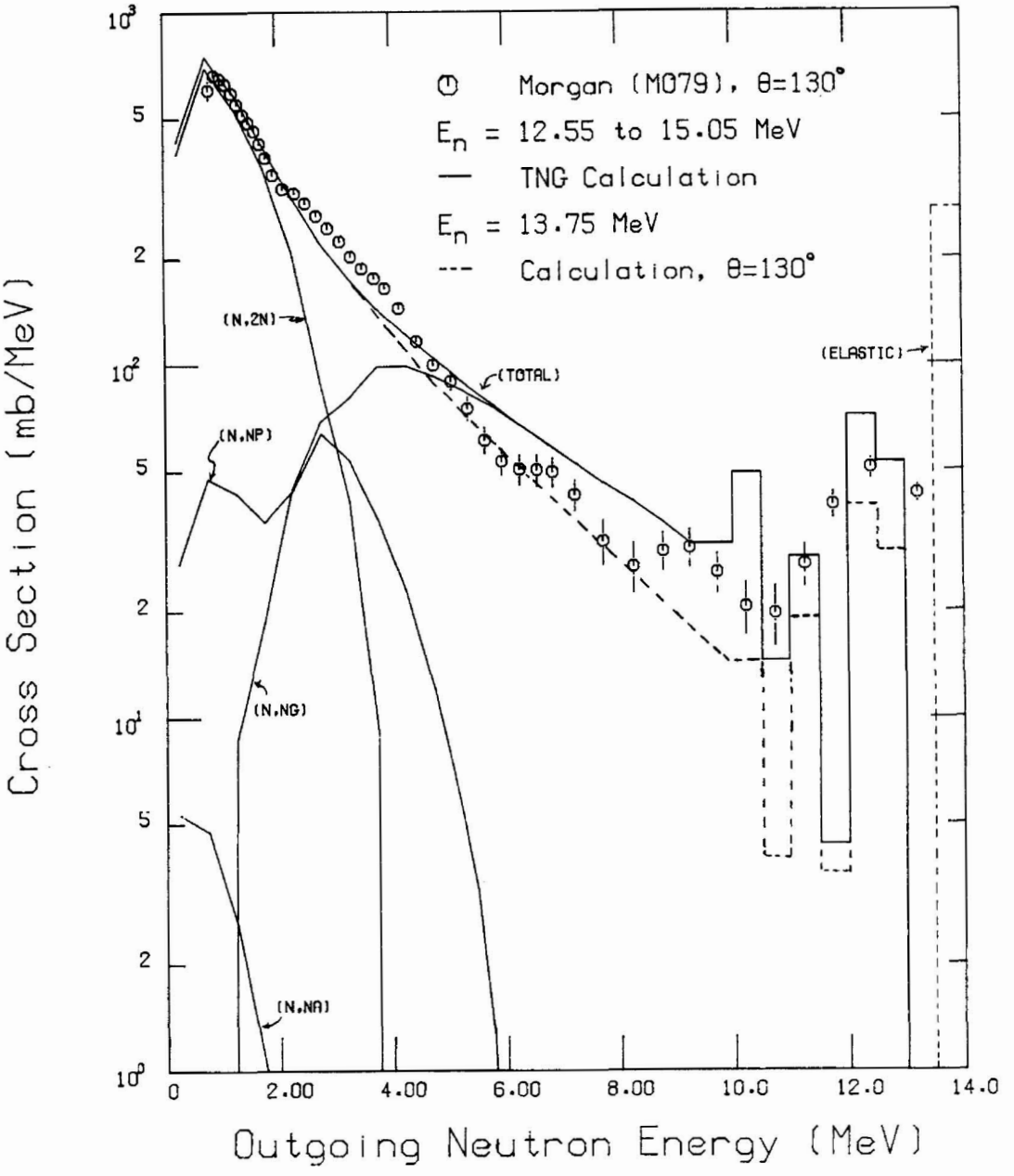

Fig. 34. Neutron emission spectra from the TNG calculation compared with the data of Morgan (M079). Also shown is the calculation for $\theta=130^{o}$. The calculated elastic cross section is not smeared and is not in phase with the data. Contributions from the various neutron-producing components are shown (they sum to the total). The curves labeled (n,np) and (n,nα) include the (n,pn) and (n,αn) components, respectively.

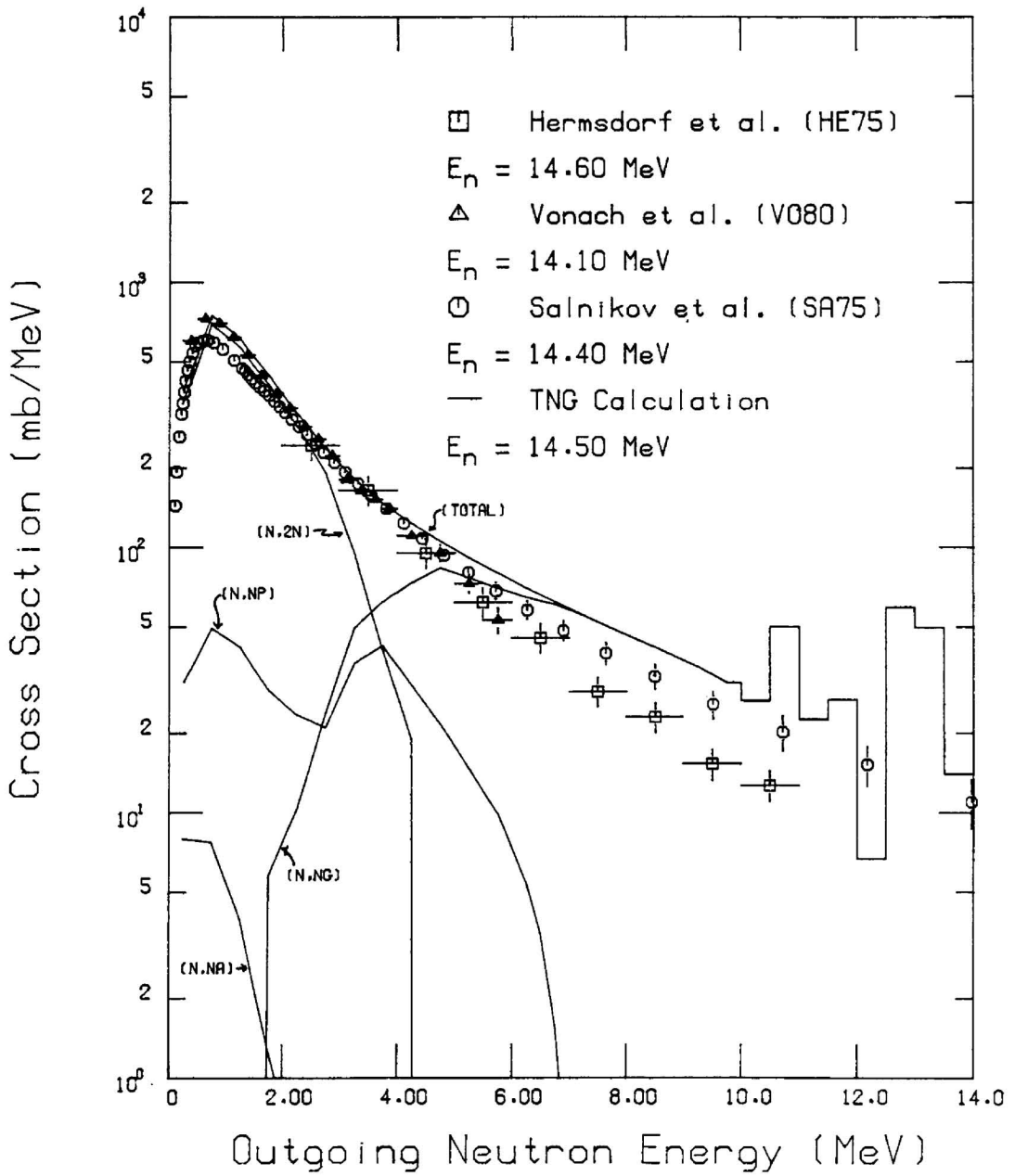

Fig. 35. Neutron emission spectra from the TNG calculation compared with the data of Hermsdorf et al. (HE75), Vonach et al. (V080), and Salnikov et al. (SA75). All data shown are angle integrated. Contributions from the various neutron-producing components are shown (they sum to the total). The curves labeled (n,np) and (n,nα) include the (n,pn) and (n,αn) components, respectively.

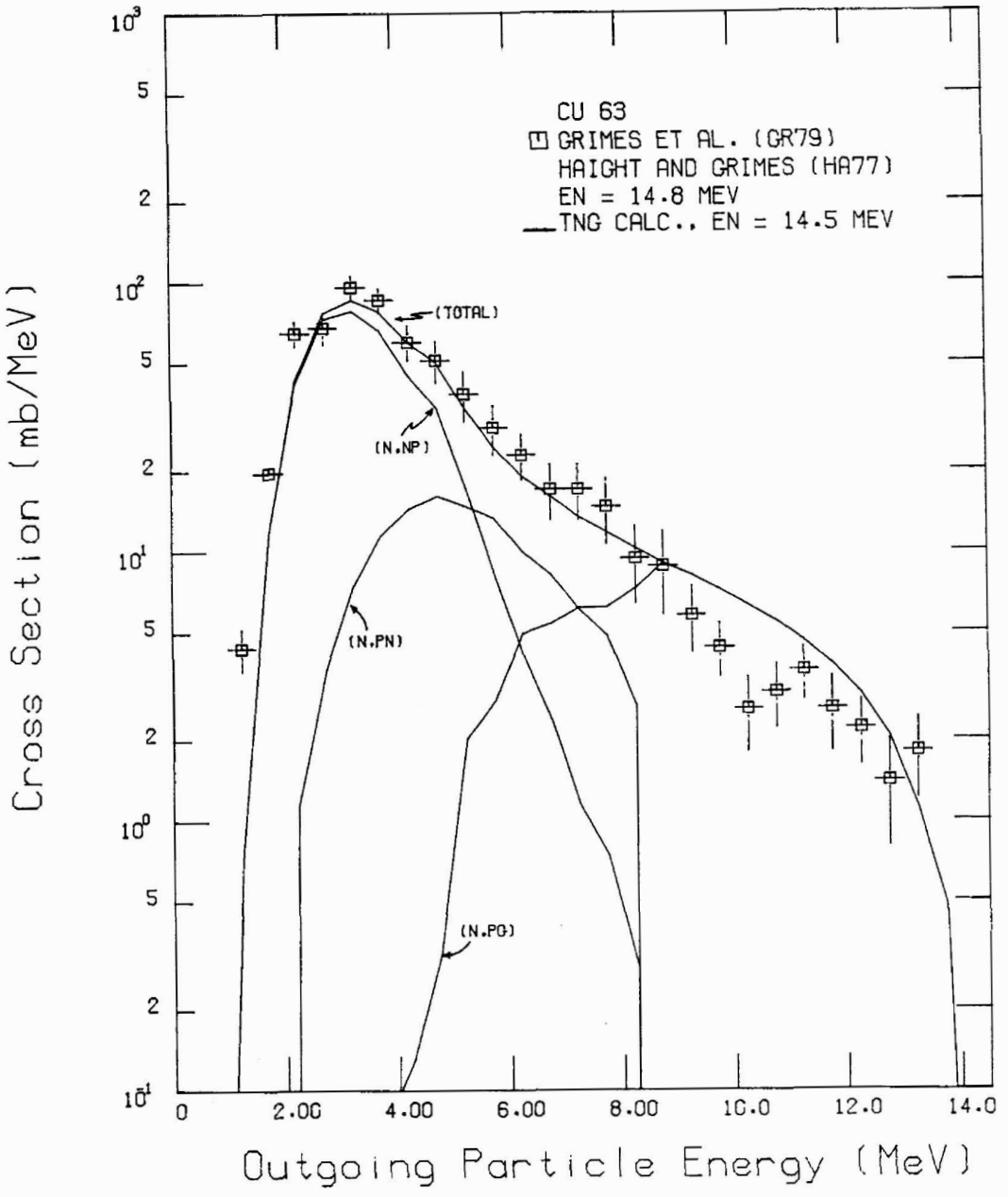

Fig. 36. Comparison of calculated and experimental proton production spectra for ^{63}Cu. The measurement was taken at an incident energy of 14.8 MeV, the TNG calculation was for E_n=14.5 MeV.

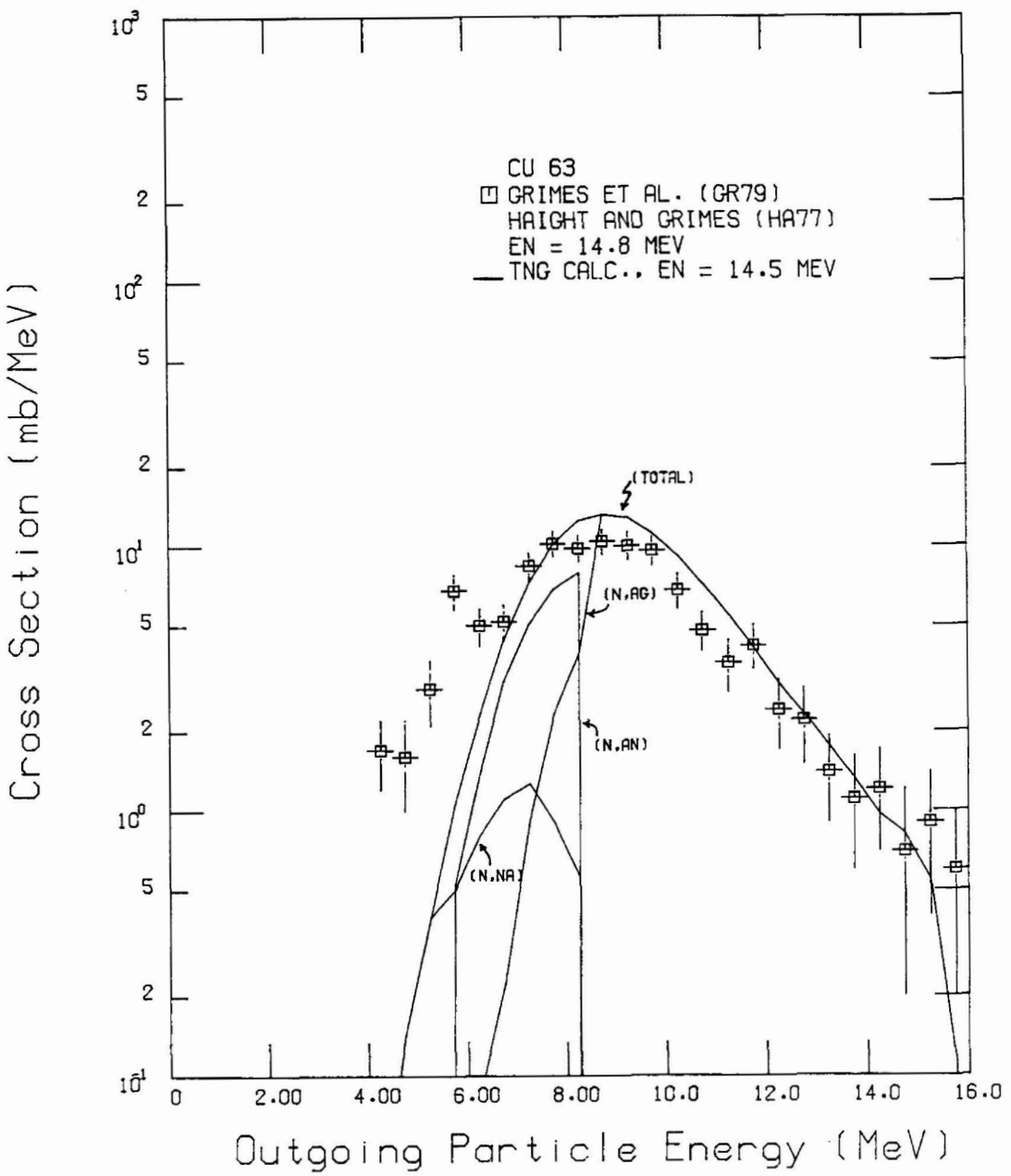

Fig. 37. Comparison of calculated and experimental alpha production spectra for ^{63}Cu. The measurement was taken at an incident energy of 14.8 MeV, the TNG calculation was for E_n=14.5 MeV.

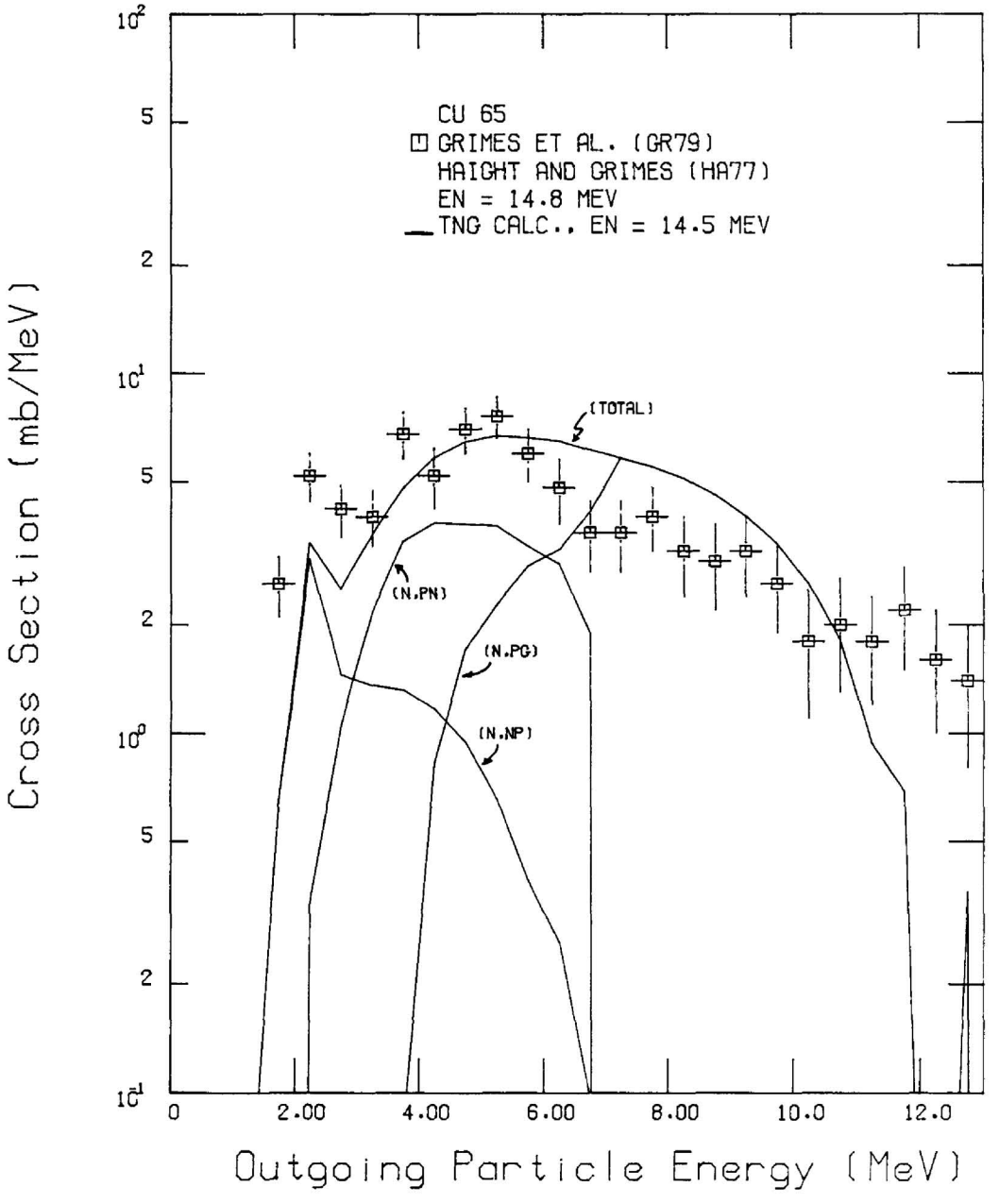

Fig. 38. Comparison of calculated and experimental proton production spectra for ^{65}Cu. The measurement was taken at an incident energy of 14.8 MeV, the TNG calculation was for E_n=14.5 MeV.

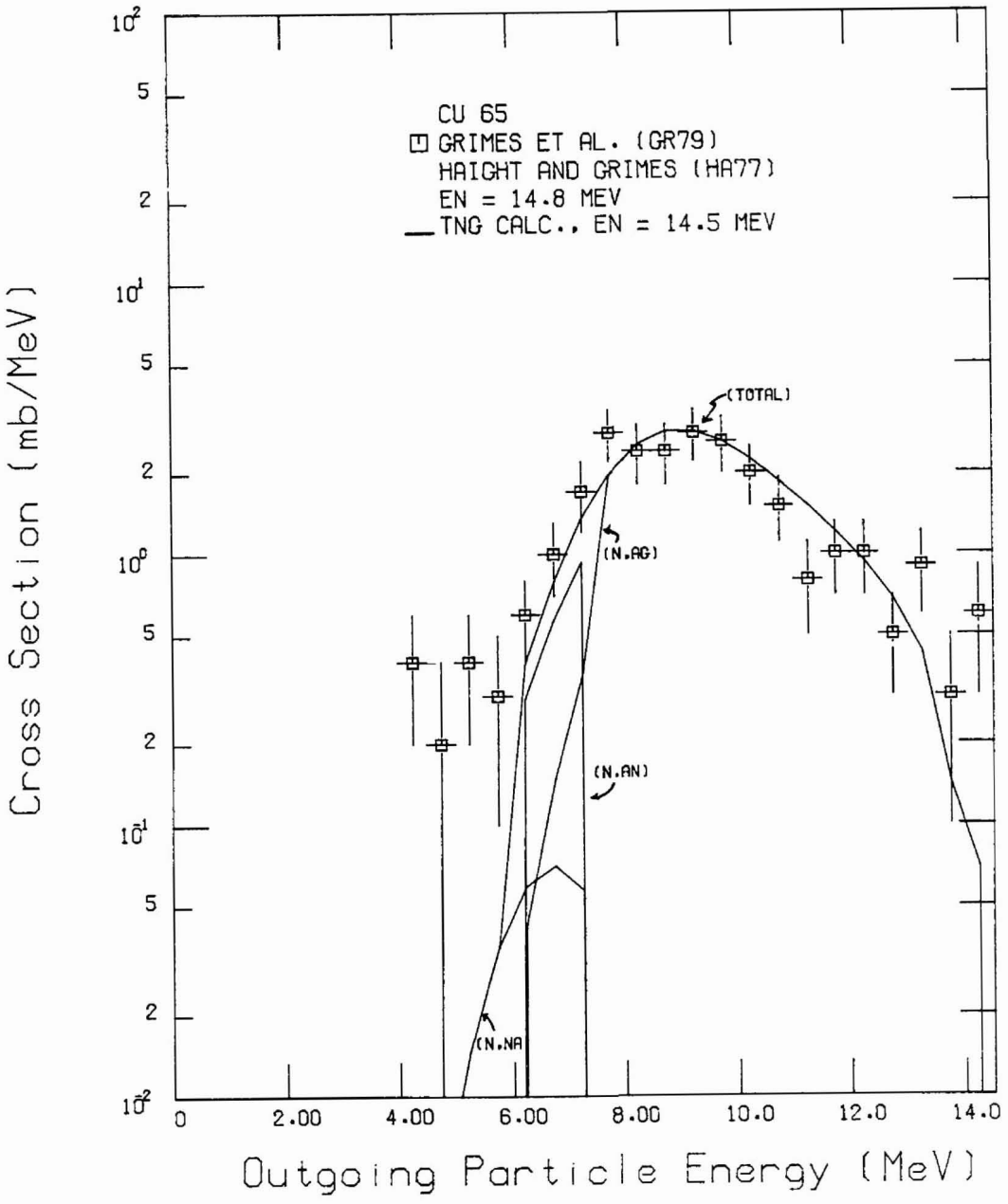

Fig. 39. Comparison of calculated and experimental alpha production spectra for ^{65}Cu. The measurement was taken at an incident energy of 14.8 MeV, the TNG calculation was for E_n=14.5 MeV.

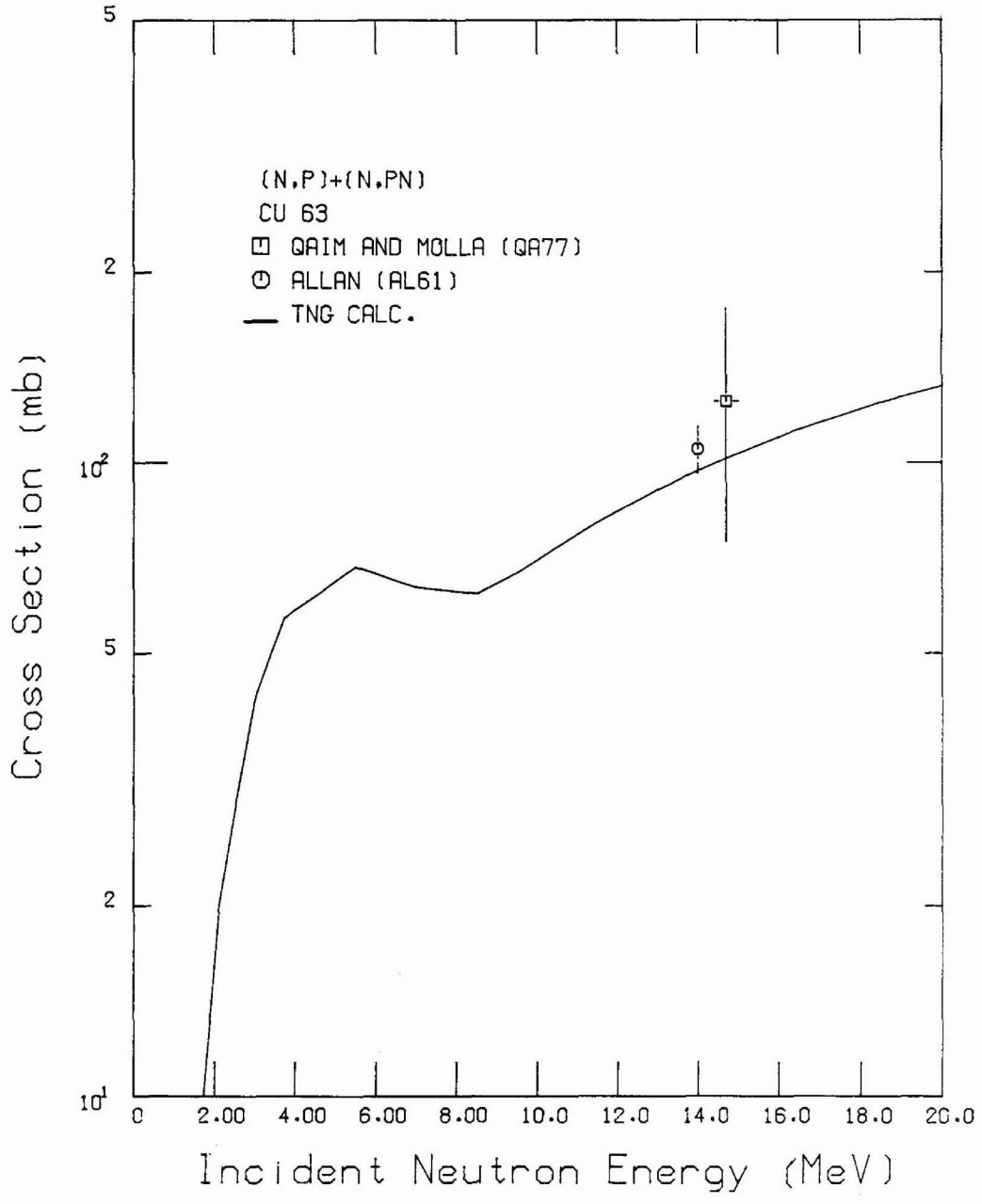

Fig. 40. Comparison of calculated and experimental $^{63}Cu(n,p)+(n,pn)$ cross sections.

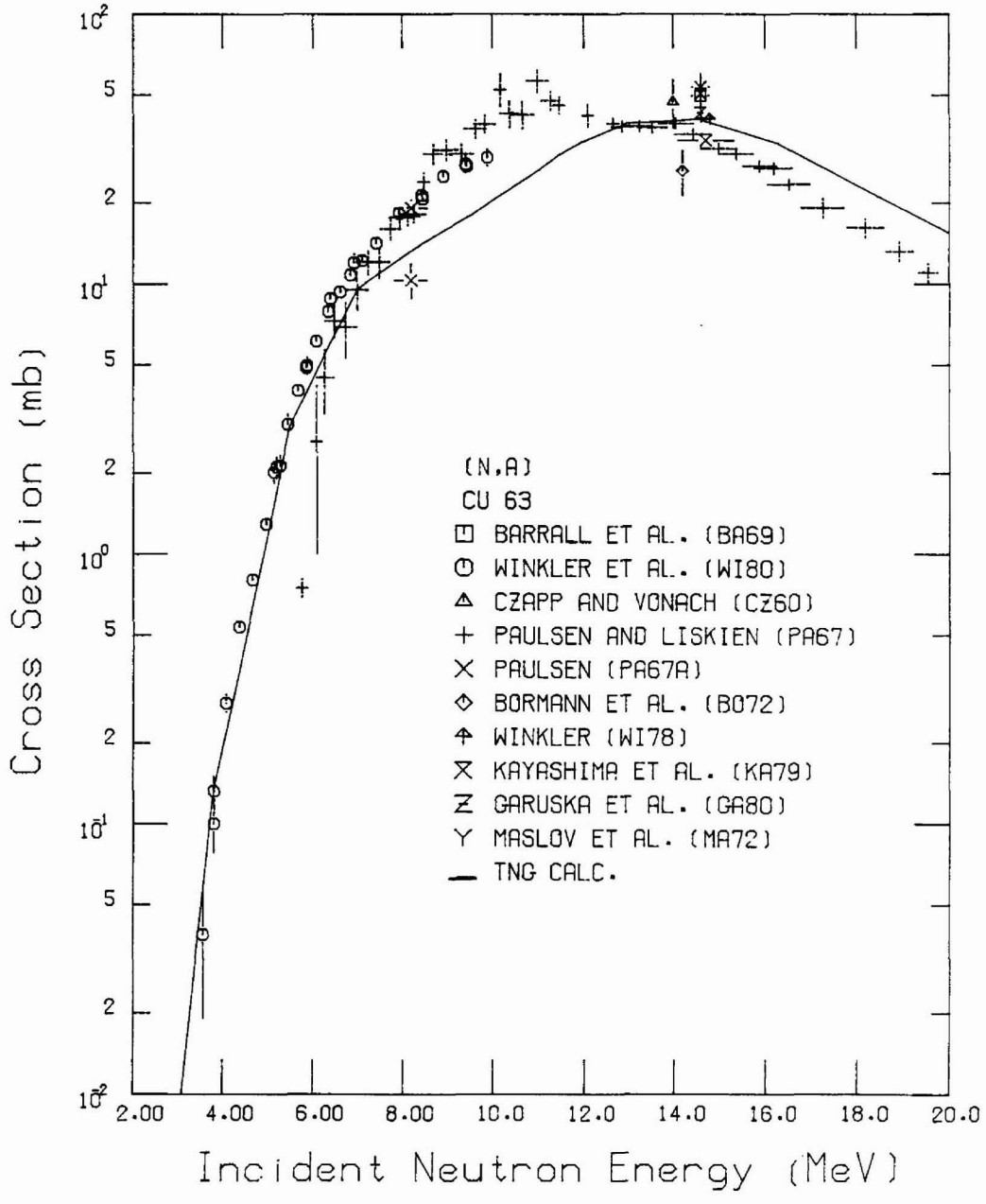

Fig. 41. Comparison of calculated and experimental $^{63}Cu(n,\alpha)$ cross sections.

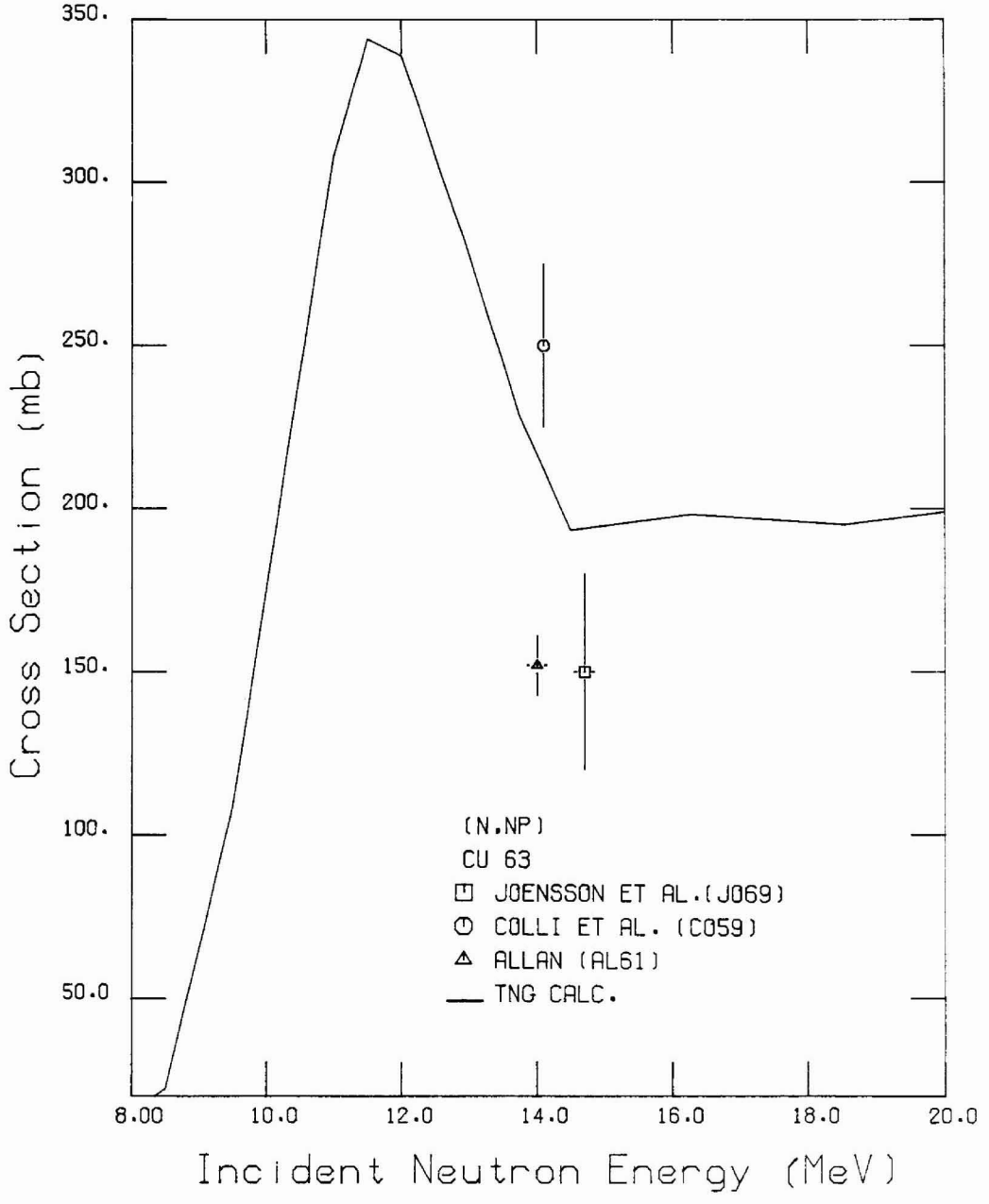

Fig. 42. Comparison of calculated and experimental $^{63}Cu(n,np)$ cross sections. This does not include the (n,pn) component.

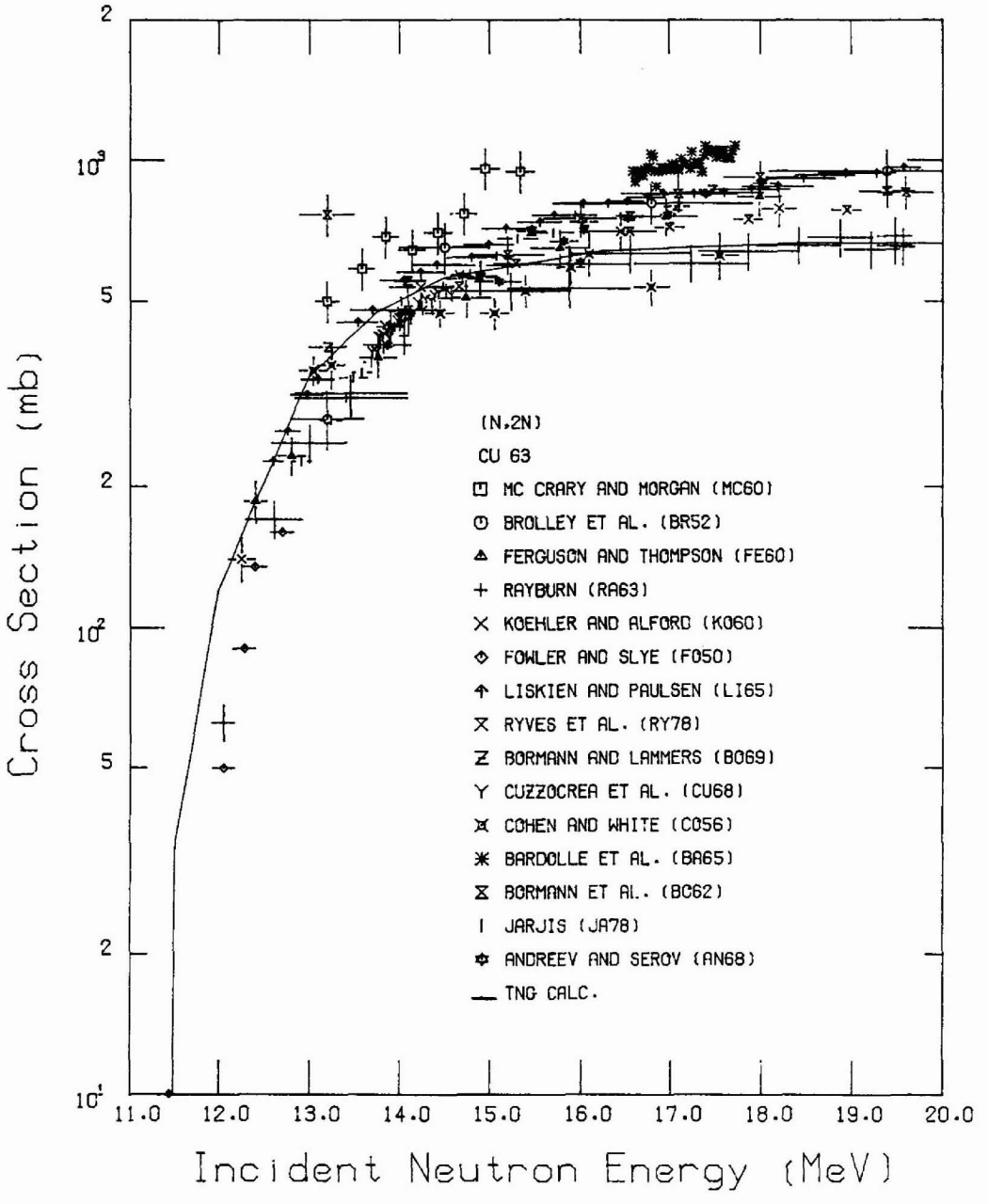

Fig. 43. Comparison of calculated and experimental $^{63}Cu(n,2n)$ cross sections.

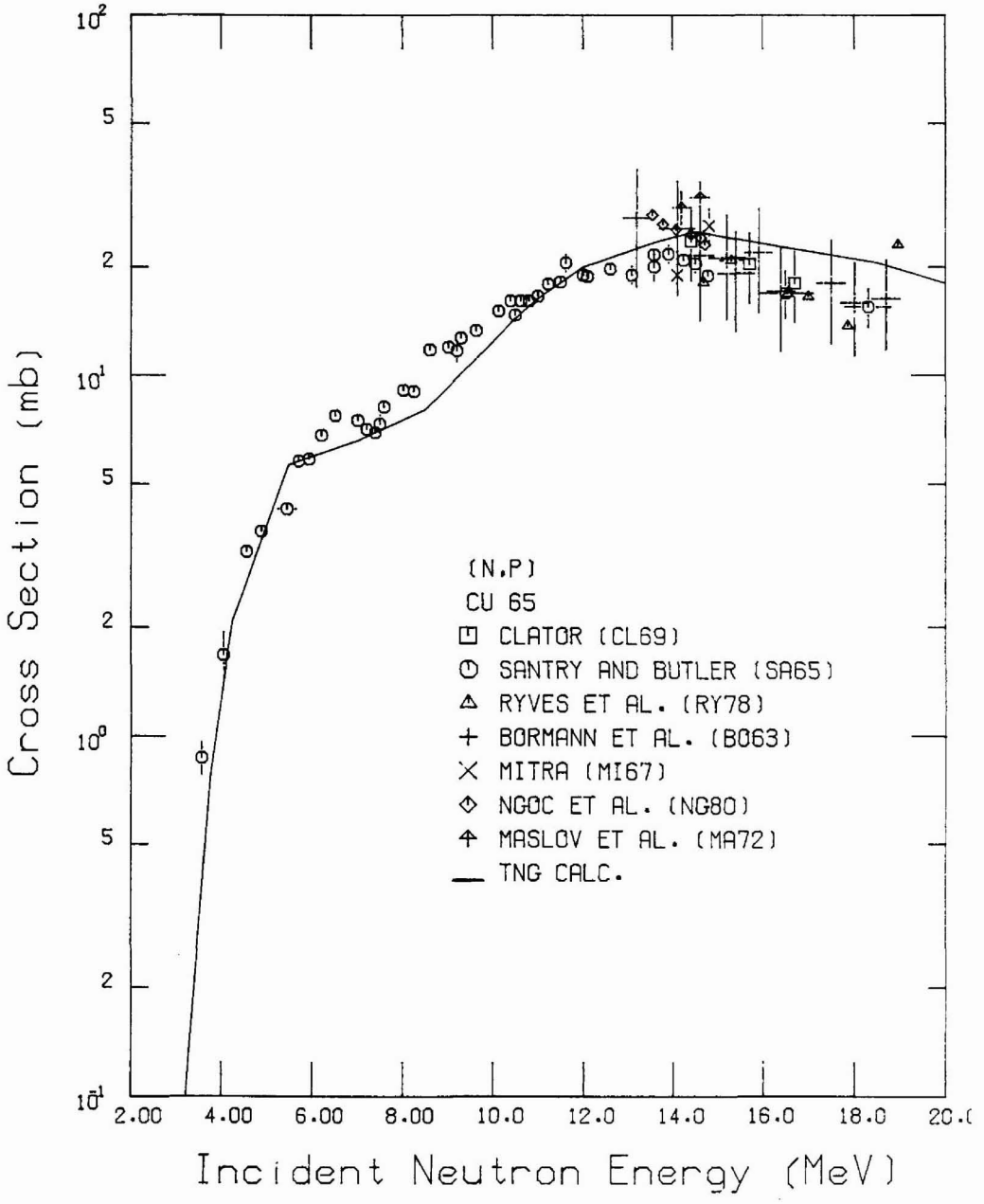

Fig. 44. Comparison of calculated and experimental $^{65}Cu(n,p)$ cross sections.

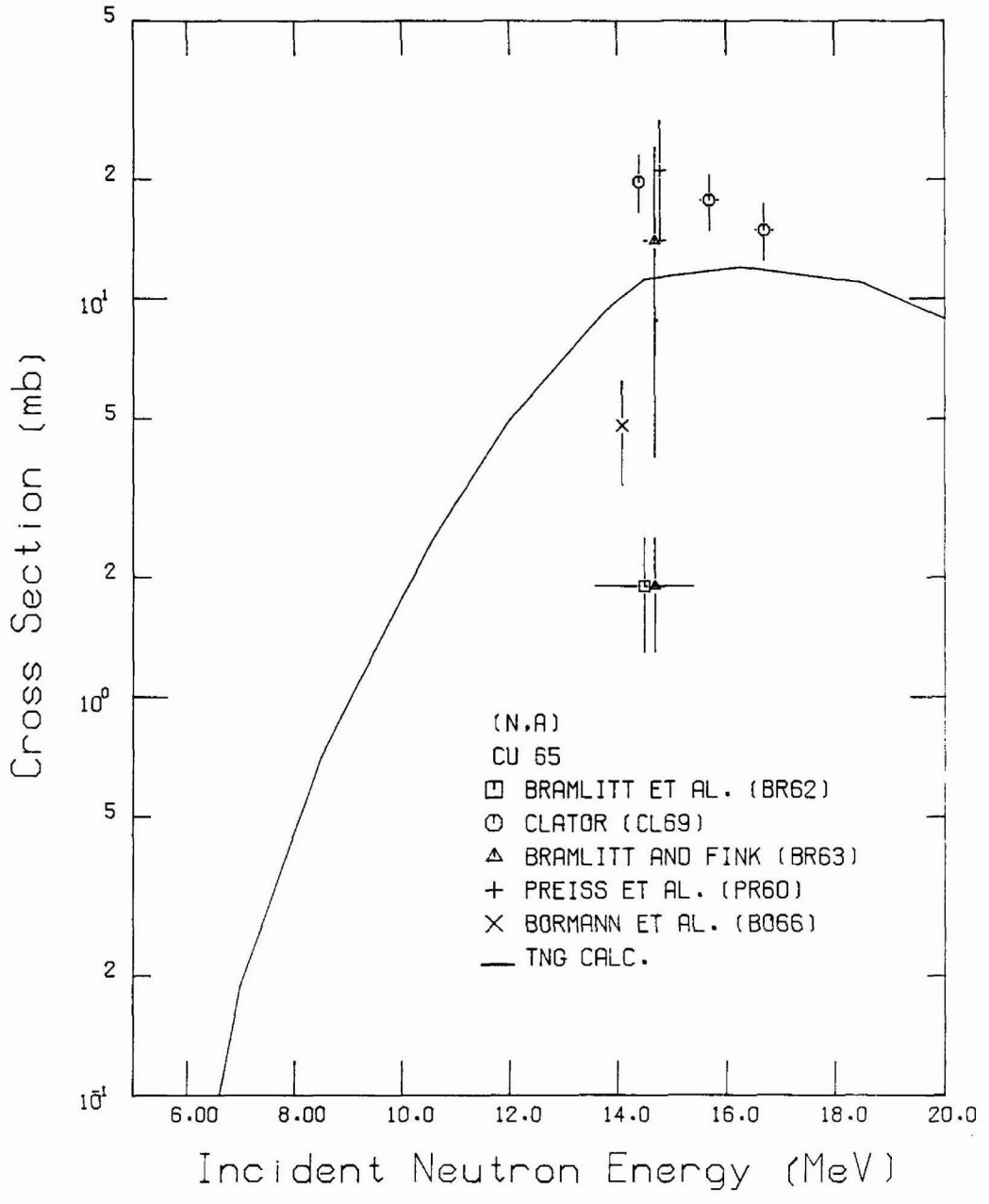

Fig. 45. Comparison of calculated and experimental $^{65}Cu(n,\alpha)$ cross sections.

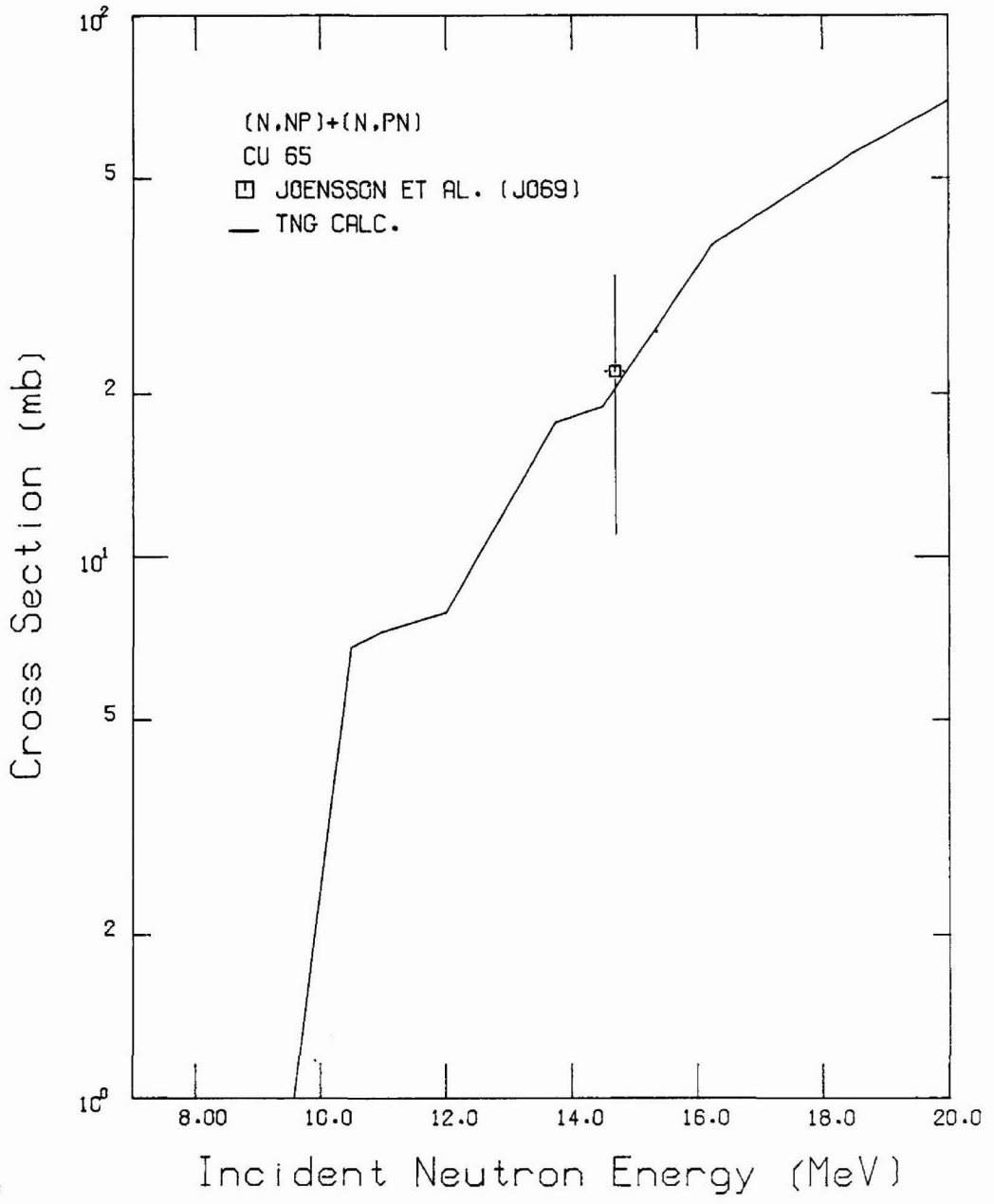

Fig. 46. Comparison of calculated and experimental $^{65}Cu(n,np)+(n,pn)$ cross sections.

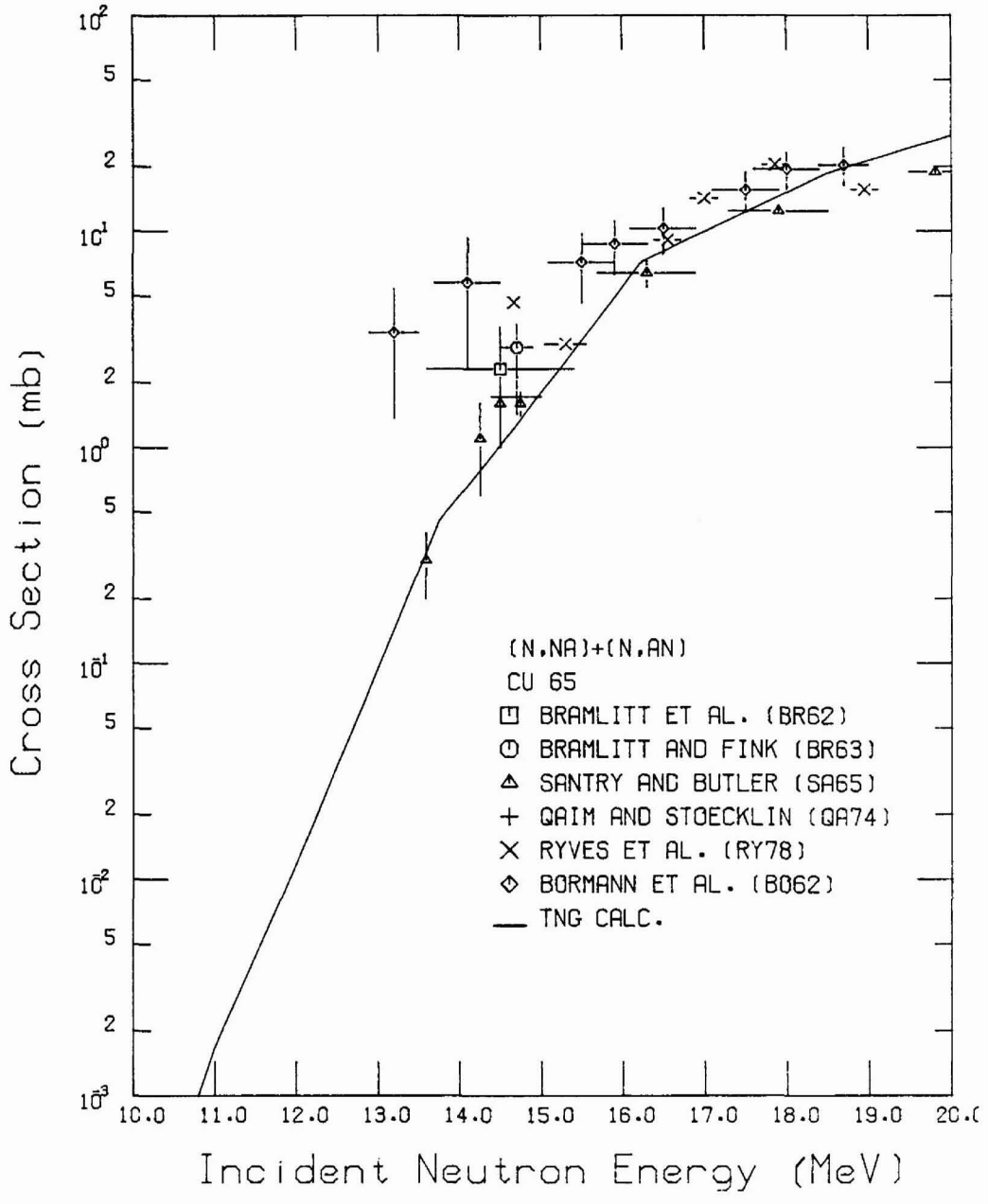

Fig. 47. Comparison of calculated and experimental $^{65}Cu(n,n\alpha)+(n,\alpha n)$ cross sections.

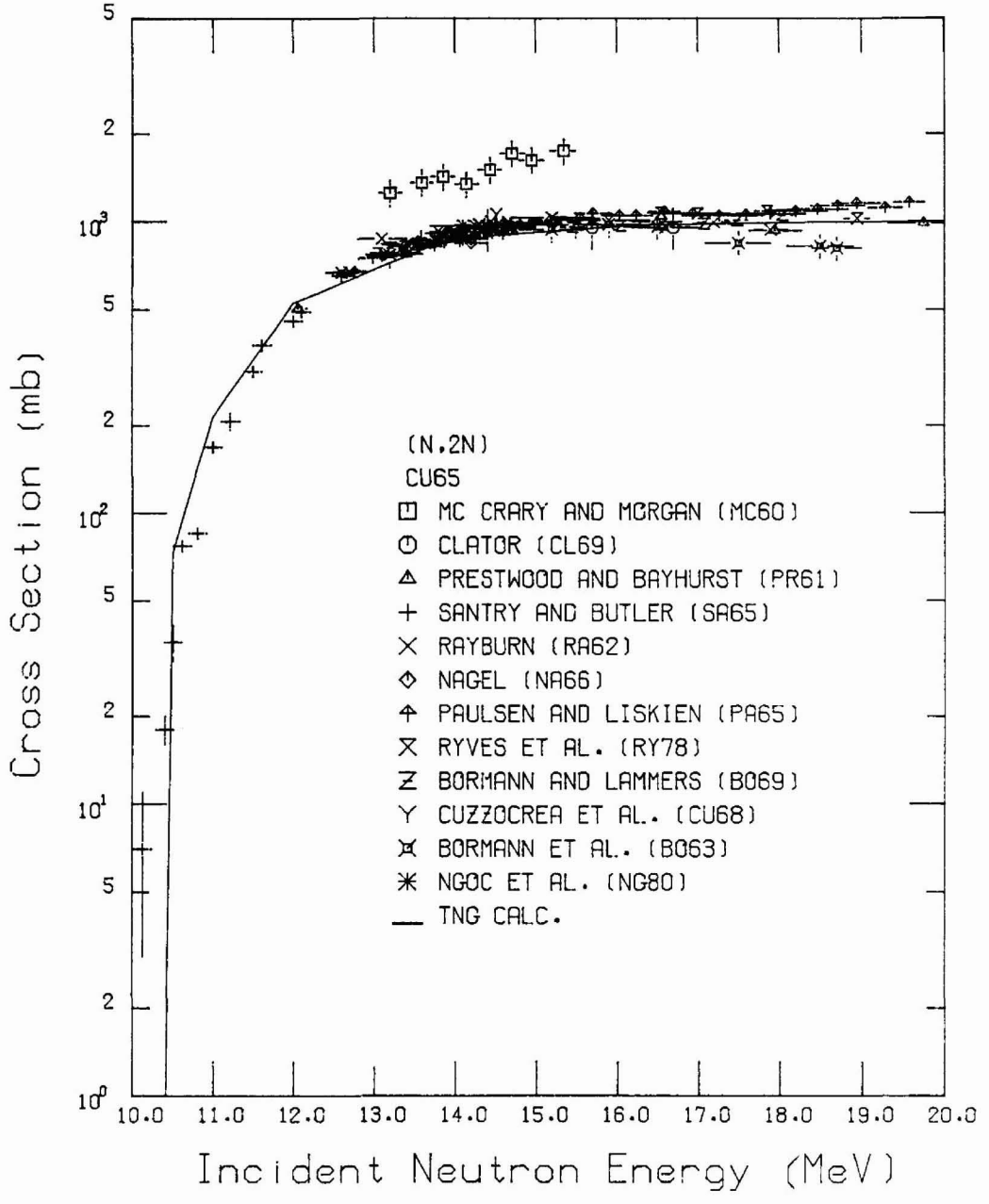

Fig. 48. Comparison of calculated and experimental $^{65}Cu(n,2n)$ cross sections.

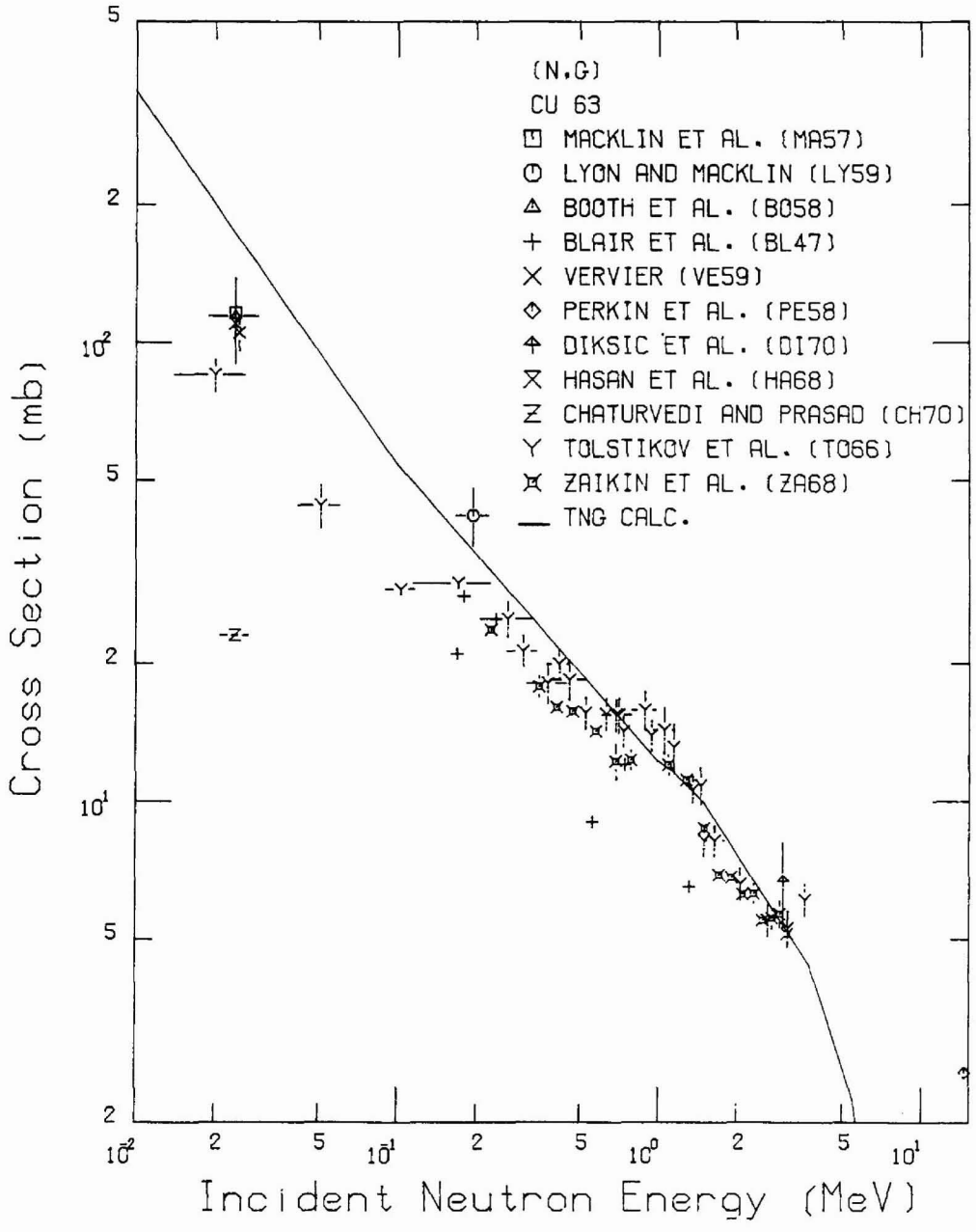

Fig. 49. Comparison of calculated and experimental $^{63}Cu(n,\gamma)$ cross sections.

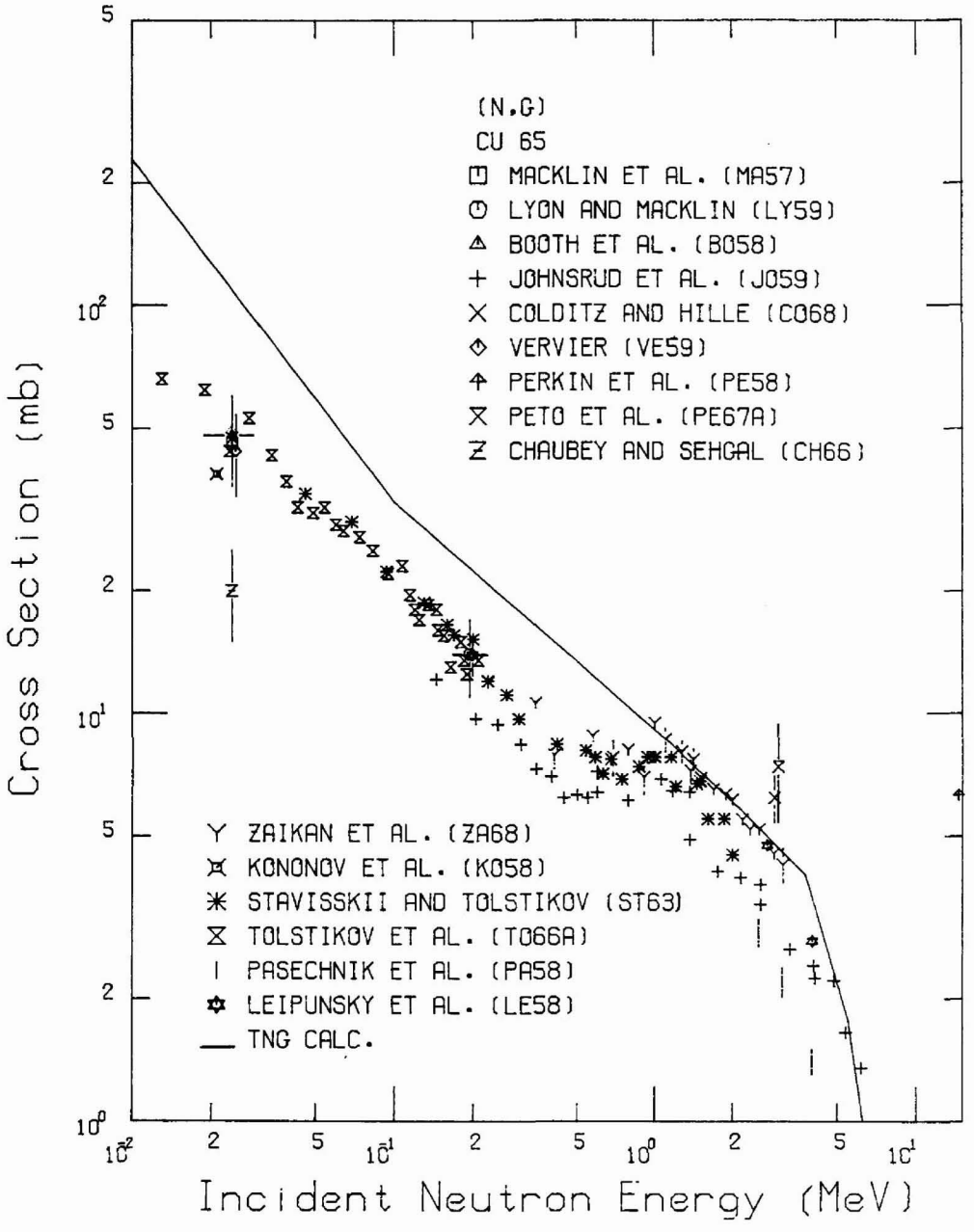

Fig. 50. Comparison of calculated and experimental $^{65}Cu(n,\gamma)$ cross sections.

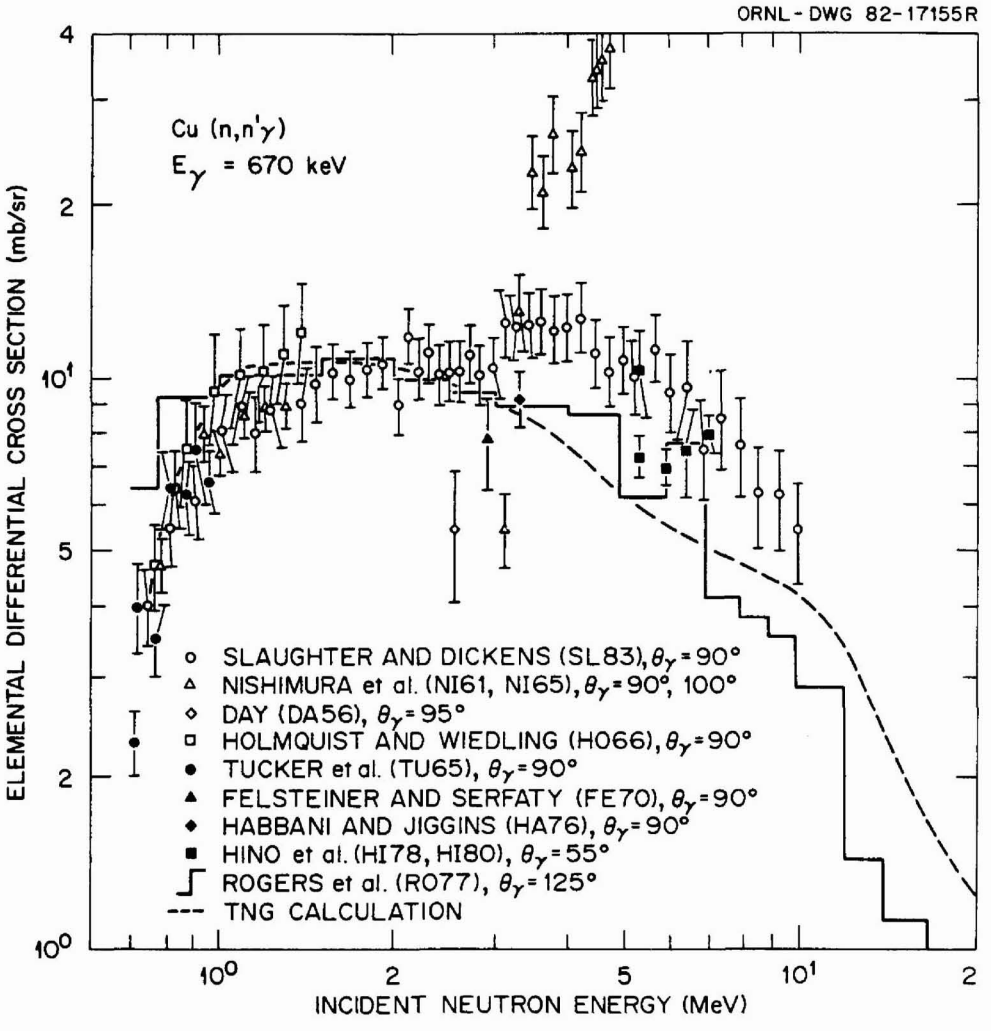

Fig. 51. Excitation function for the E_γ=670 keV transition following Cu(n,n'γ). Gamma-ray scattering angles θ_γ are given in the legend. The data of Hino et al. (HI78,HI80), Rogers et al. (RO77), and Slaughter and Dickens (SL83) were obtained using Ge(Li) detectors; the other experiments used NaI scintillation detectors.

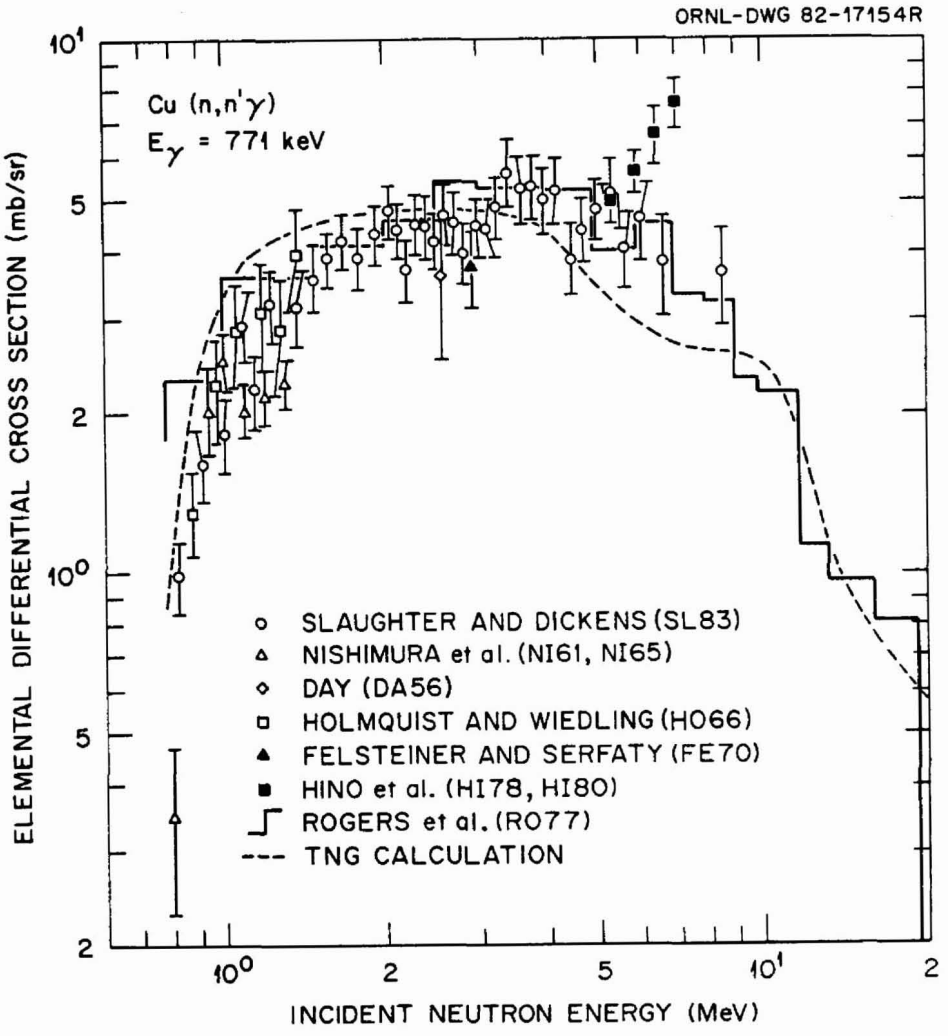

Fig. 52. Excitation function for the E_γ=771 keV transition following Cu(n,n'γ). See caption to Fig. 51 for more details.

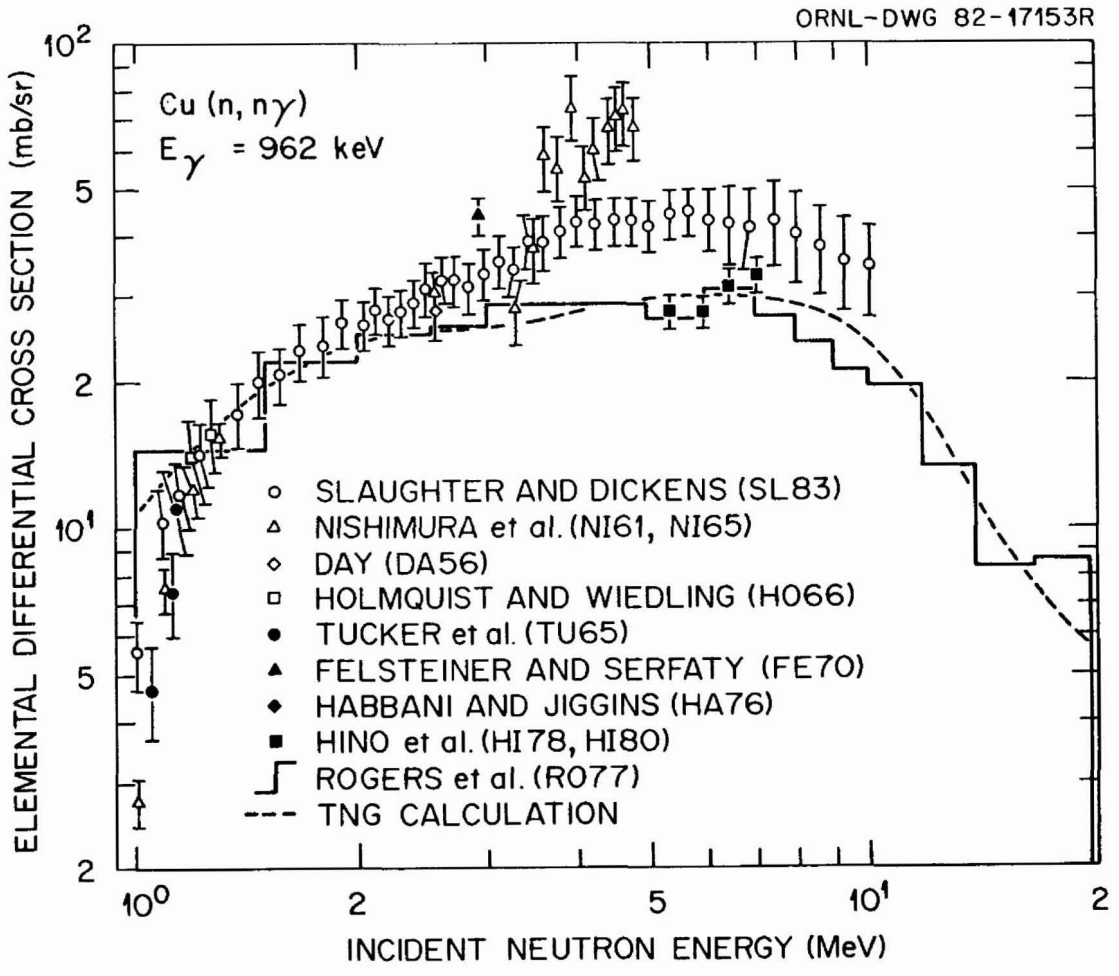

Fig. 53. Excitation function for the E_γ=962 keV transition following Cu(n,n'γ). See caption to Fig. 51 for more details.

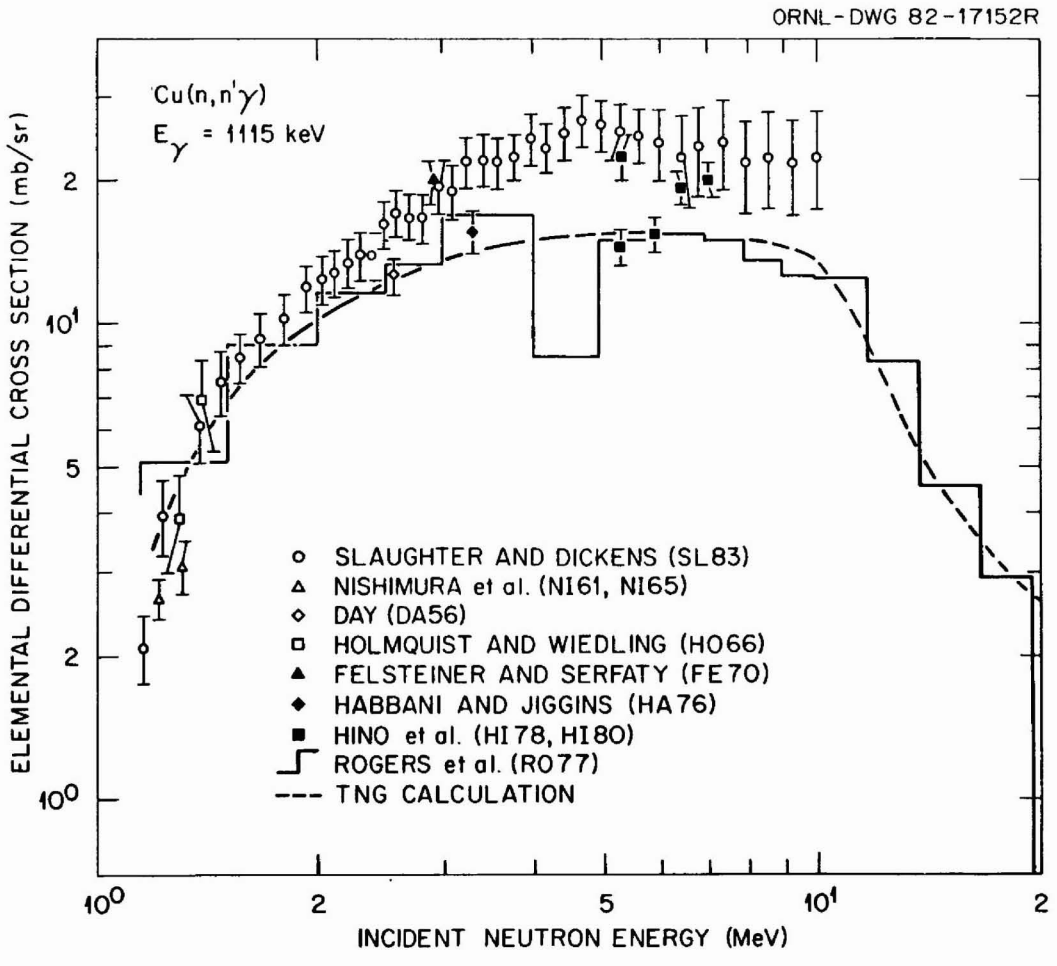

Fig. 54. Excitation function for the E_γ=1115 keV transition following Cu(n,n'γ). See caption to Fig. 51 for more details.

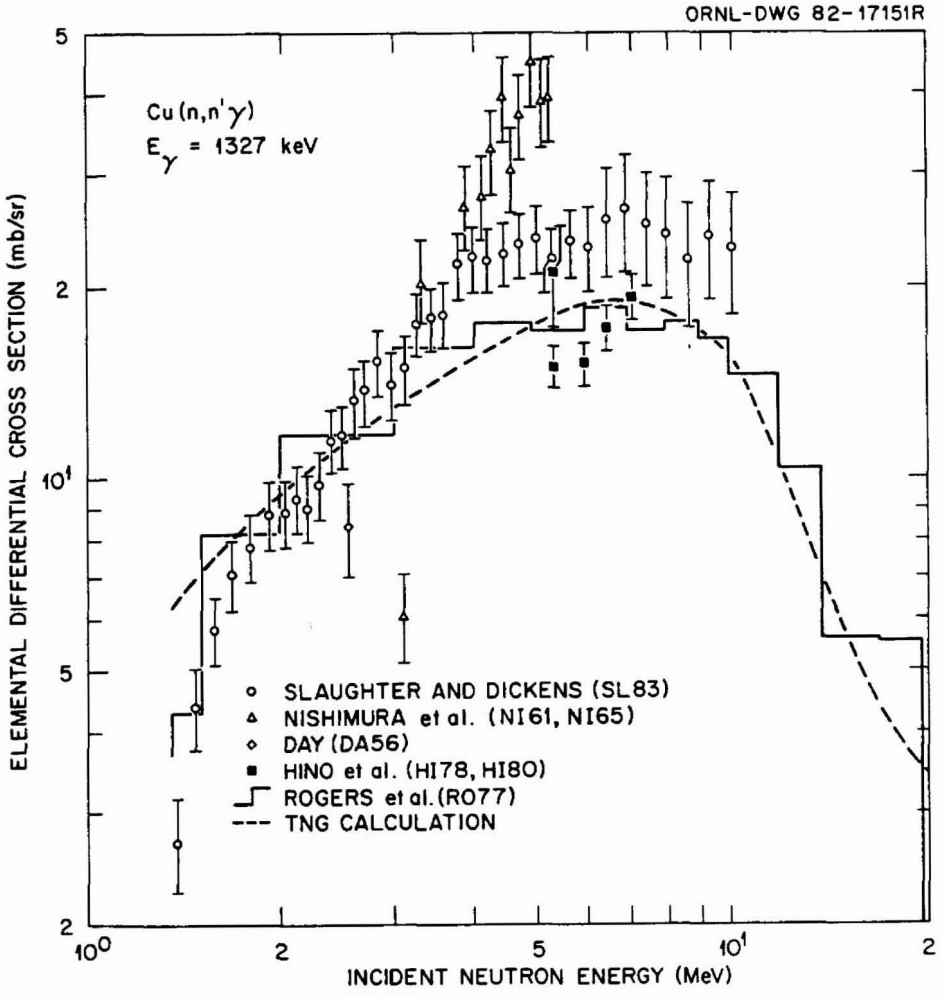

Fig. 55. Excitation function for the E_γ=1327 keV transition following Cu(n,n'γ). See caption to Fig. 51 for more details.

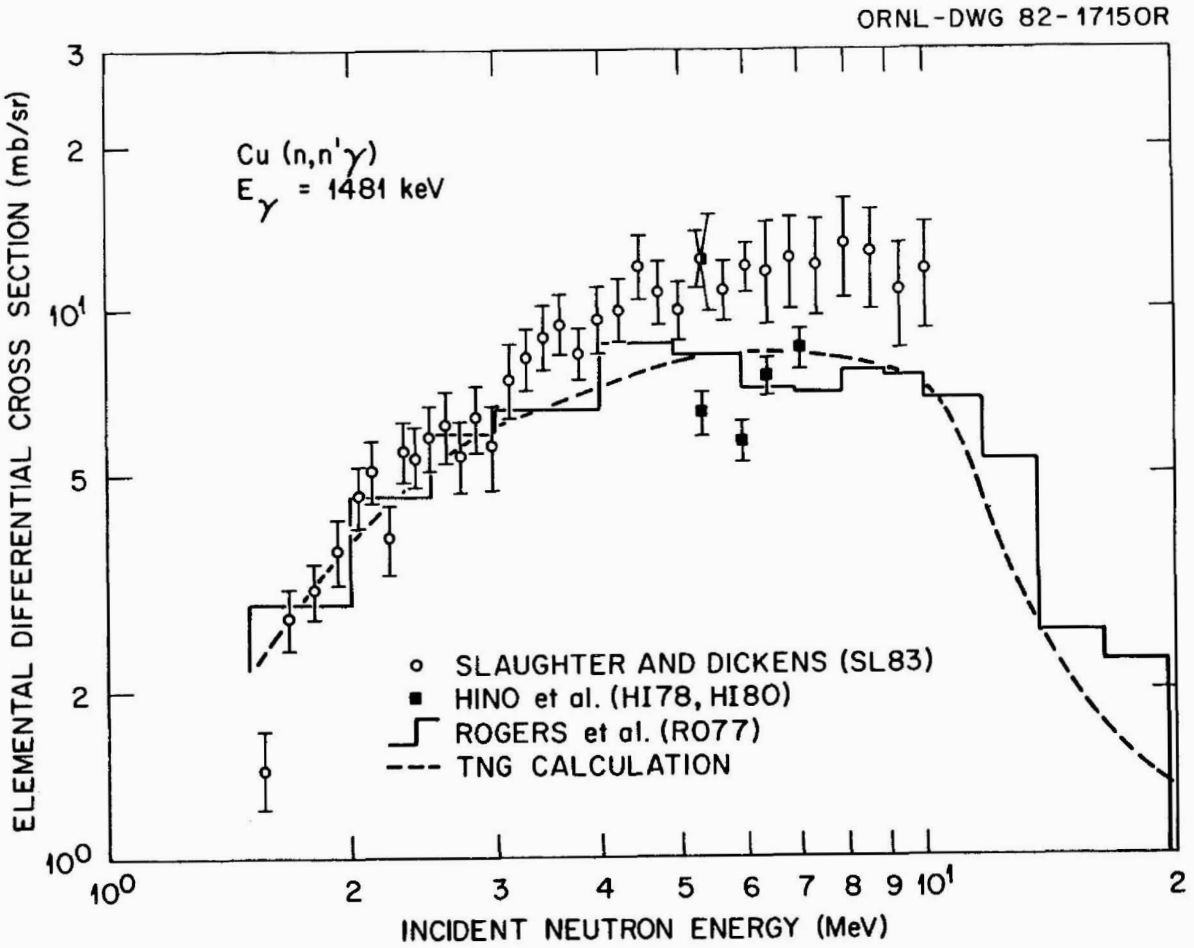

Fig. 56. Excitation function for the E_γ=1481 keV transition following Cu(n,n'γ). See caption to Fig. 51 for more details.

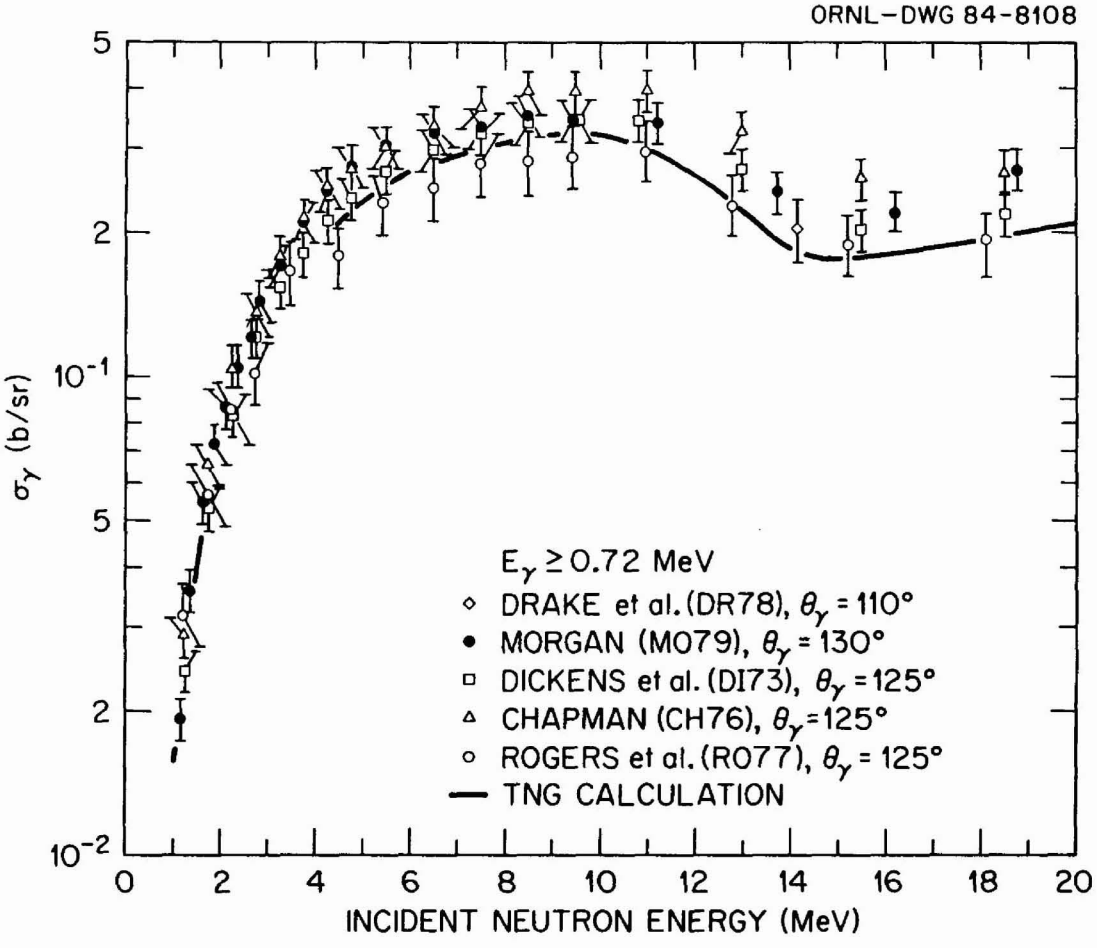

Fig. 57. Integrated yield of secondary gamma rays with $E_\gamma > 0.72$ MeV as a function of incident neutron energy. Gamma-ray scattering angles θ_γ are given in the legend.

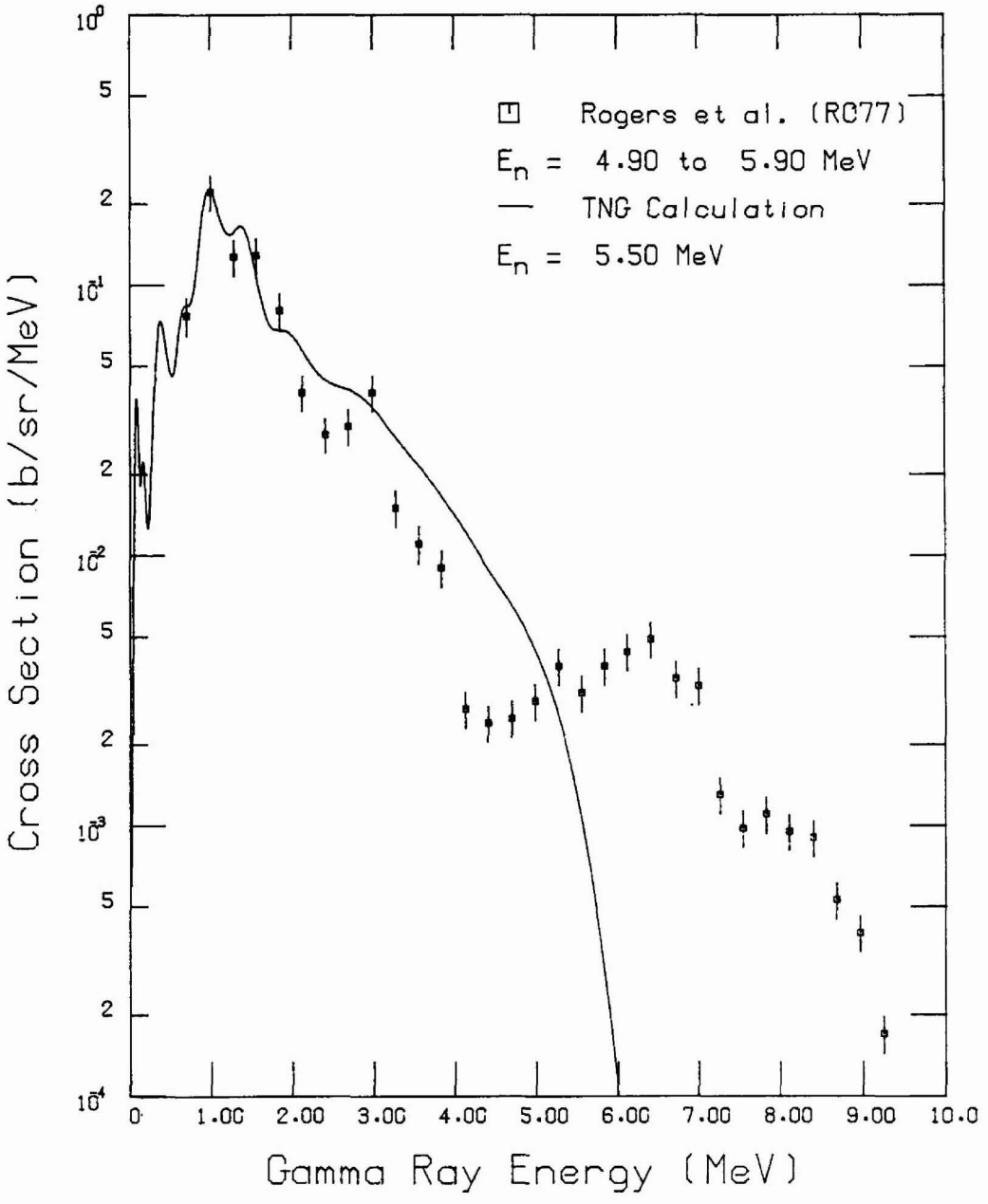

Fig. 58. Secondary gamma-ray spectra versus gamma-ray energy from the TNG calculation (incident energy E_n=5.5 MeV) compared with the data of Rogers et al. (RO77).

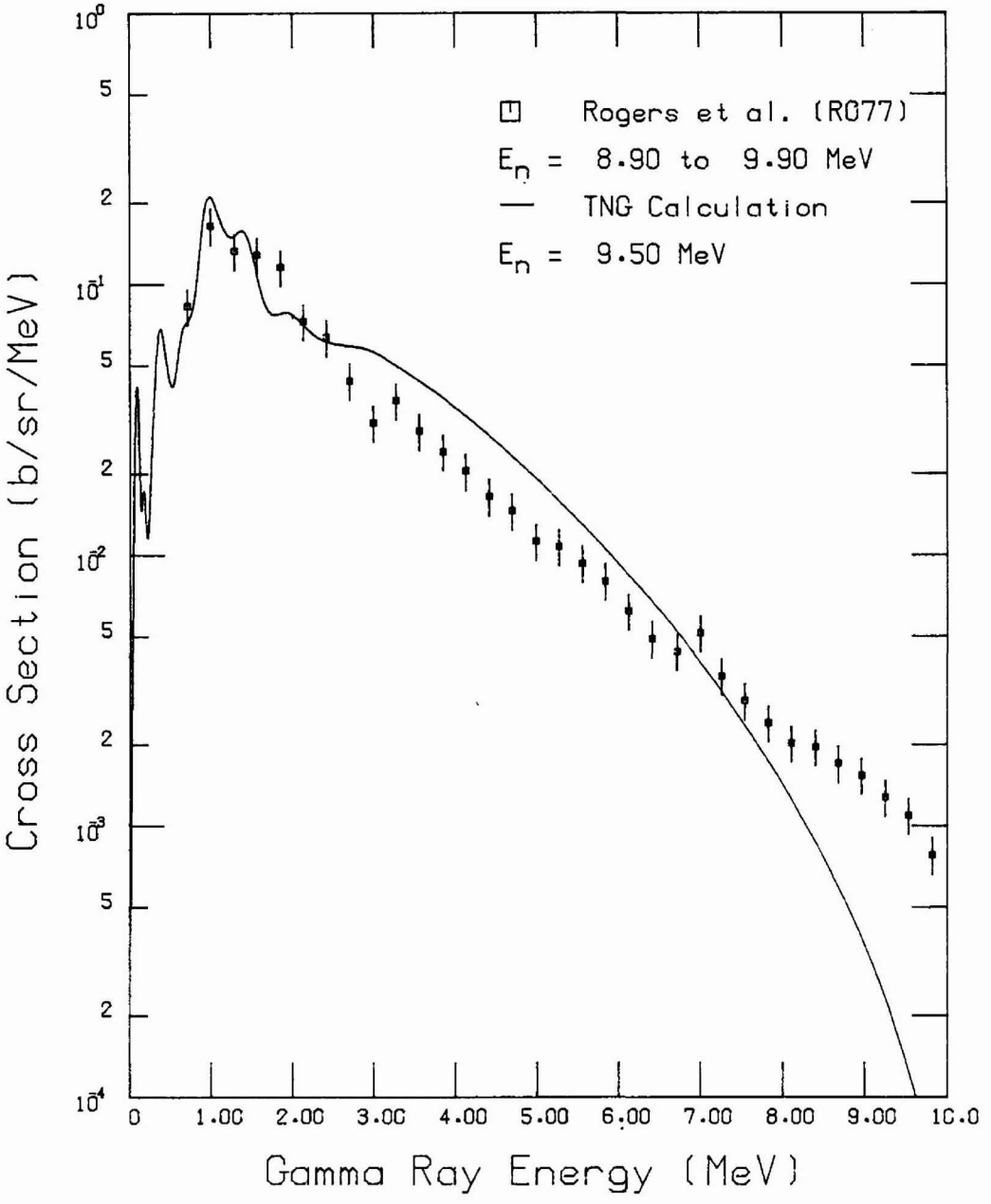

Fig. 59. Secondary gamma-ray spectra versus gamma-ray energy from the TNG calculation (incident energy E_n=9.5 MeV) compared with the data of Rogers et al. (R077).

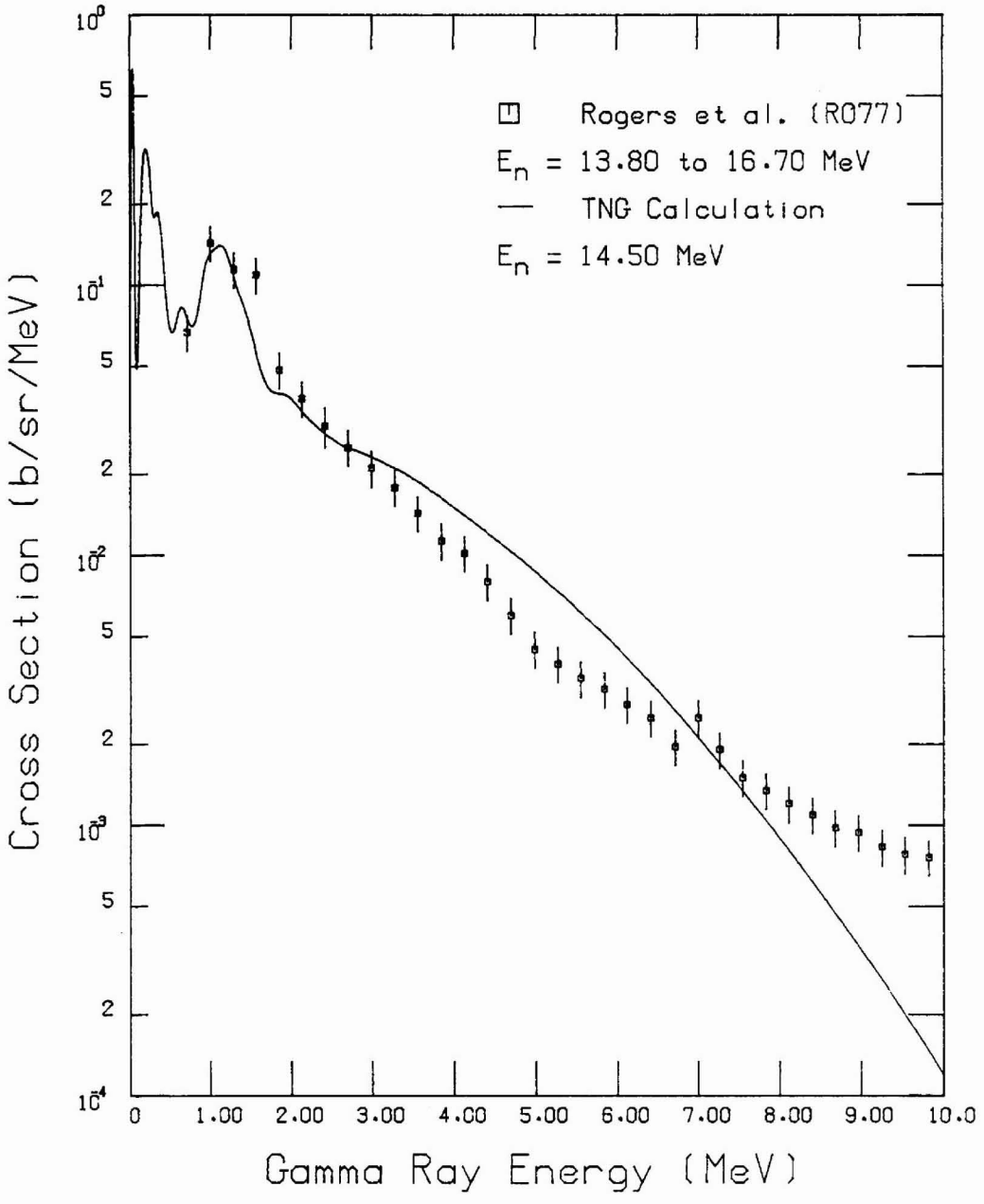

Fig. 60. Secondary gamma-ray spectra versus gamma-ray energy from the TNG calculation (incident energy E_n=14.5 MeV) compared with the data of Rogers et al. (R077).

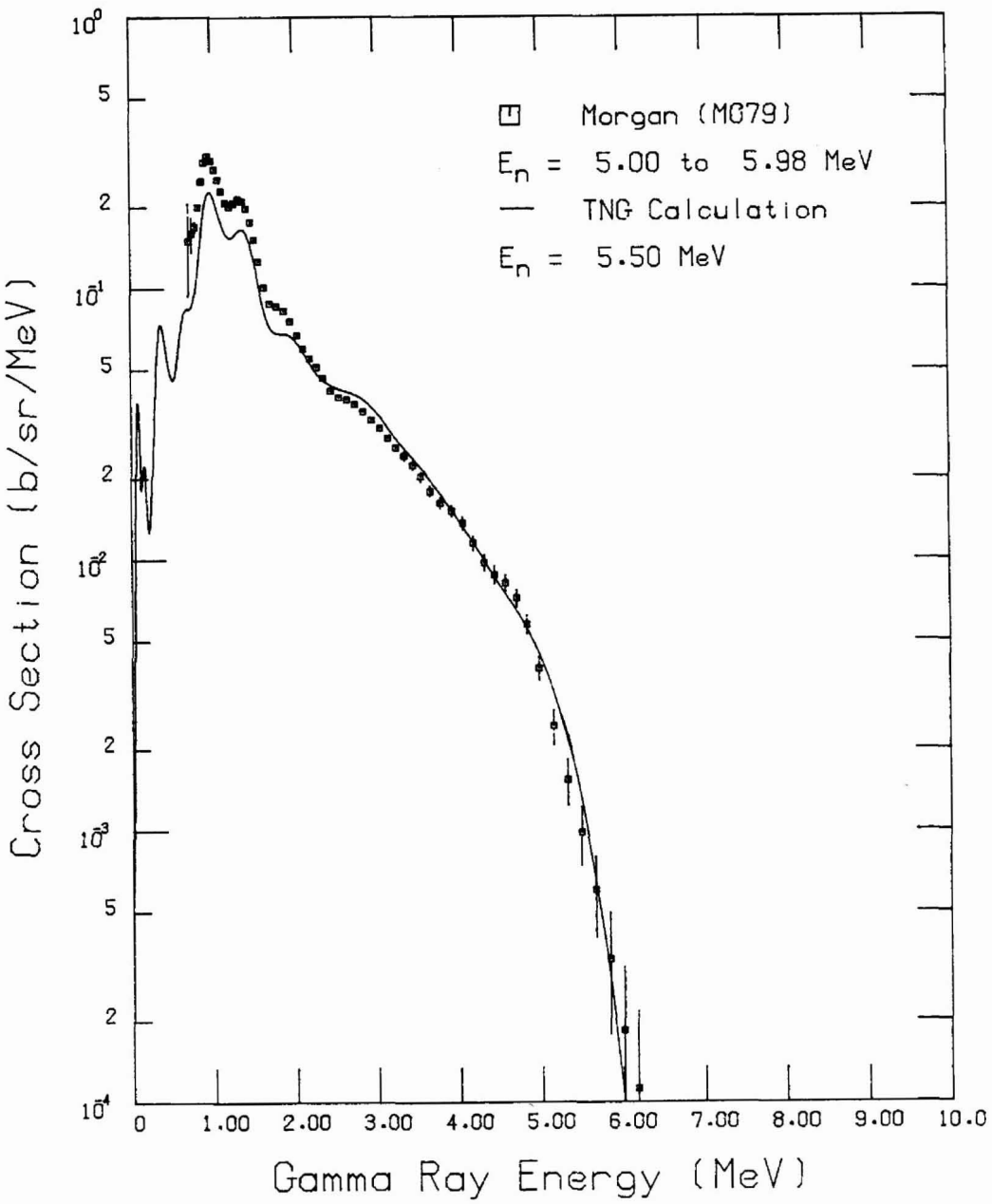

Fig. 61. Secondary gamma-ray spectra versus gamma-ray energy from the TNG calculation (incident energy E_n=5.5 MeV) compared with the data of Morgan (M079).

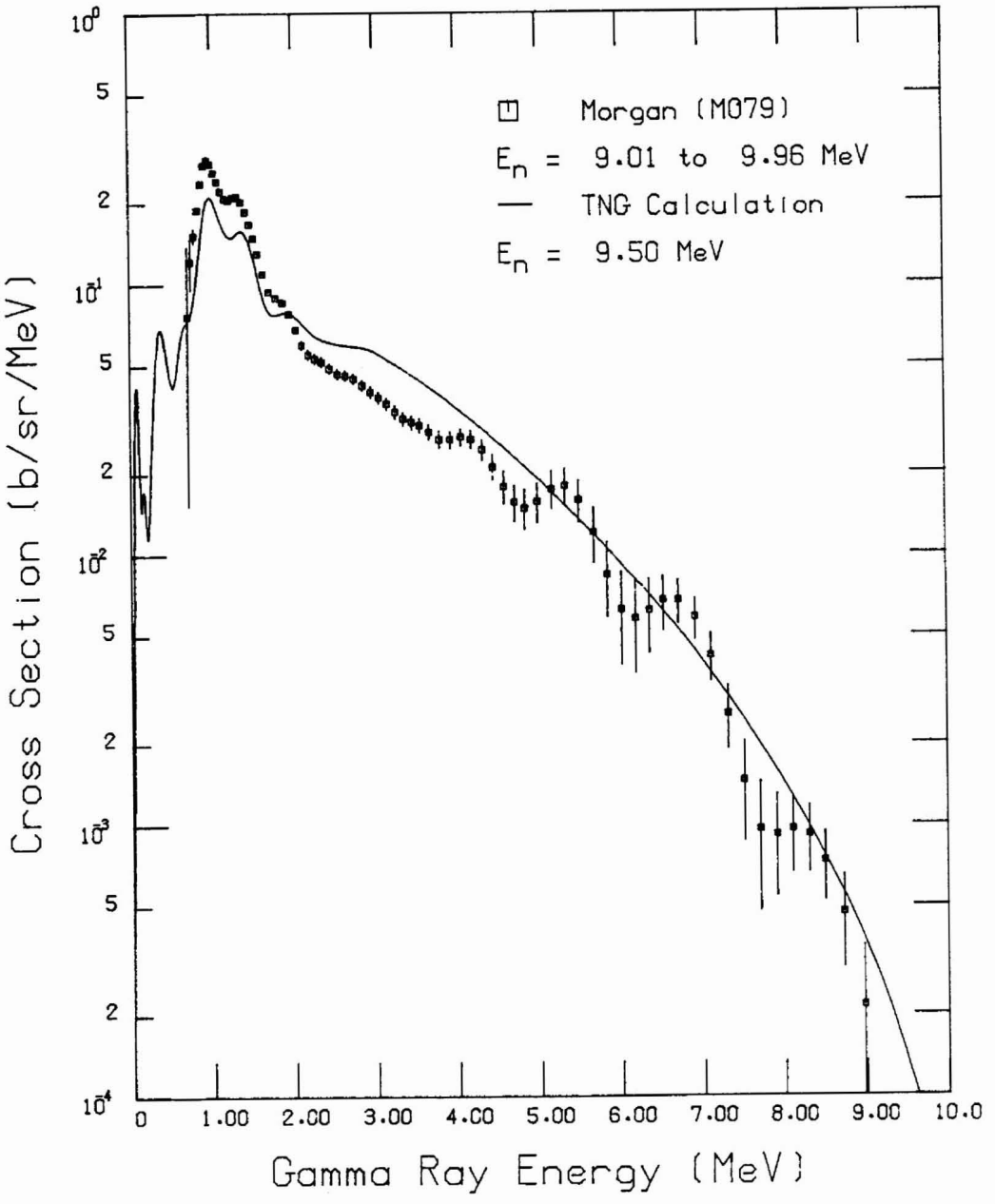

Fig. 62. Secondary gamma-ray spectra versus gamma-ray energy from the TNG calculation (incident energy E_n=9.5 MeV) compared with the data of Morgan (M079).

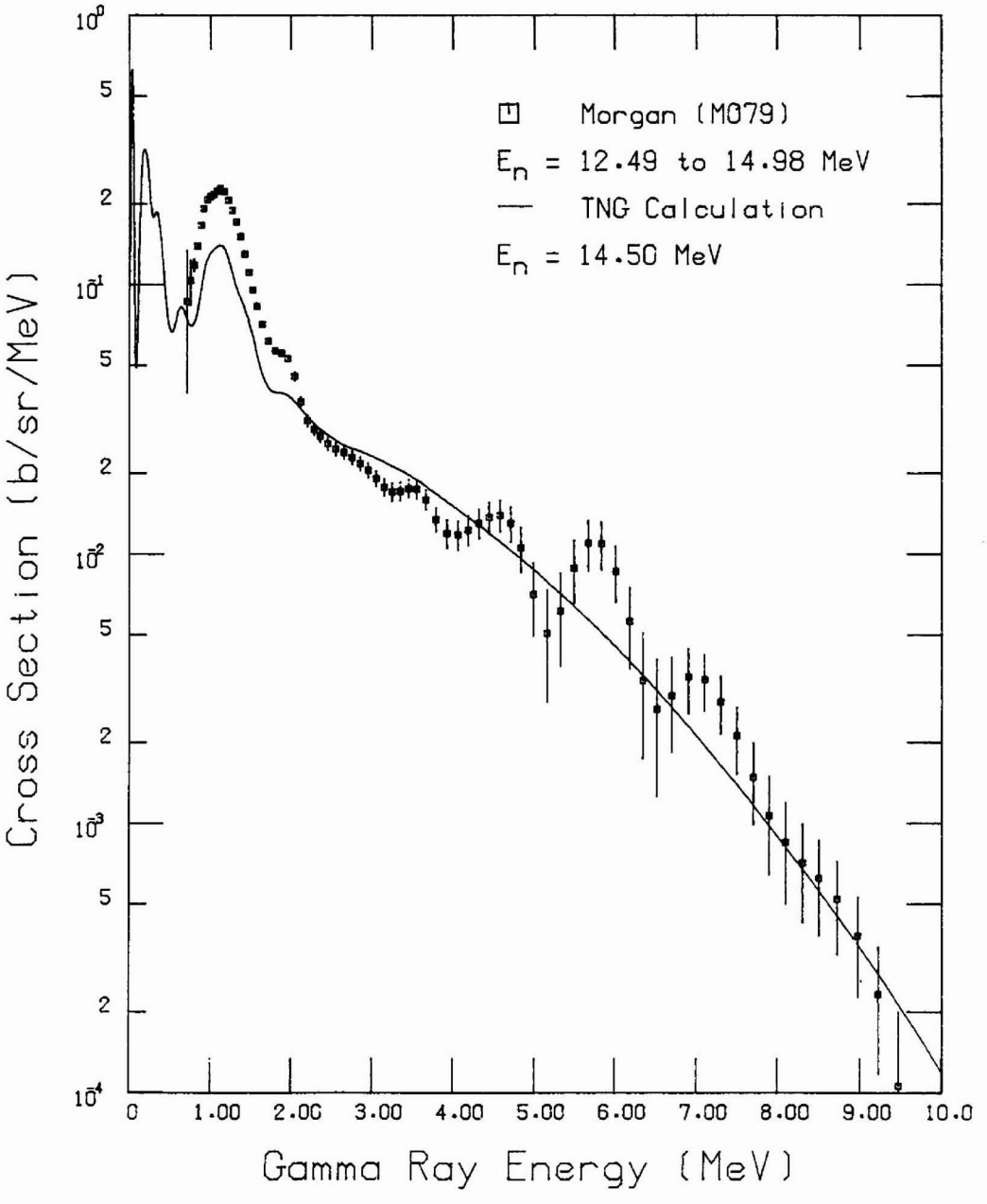

Fig. 63. Secondary gamma-ray spectra versus gamma-ray energy from the TNG calculation (incident energy E_n=14.5 MeV) compared with the data of Morgan (M079).

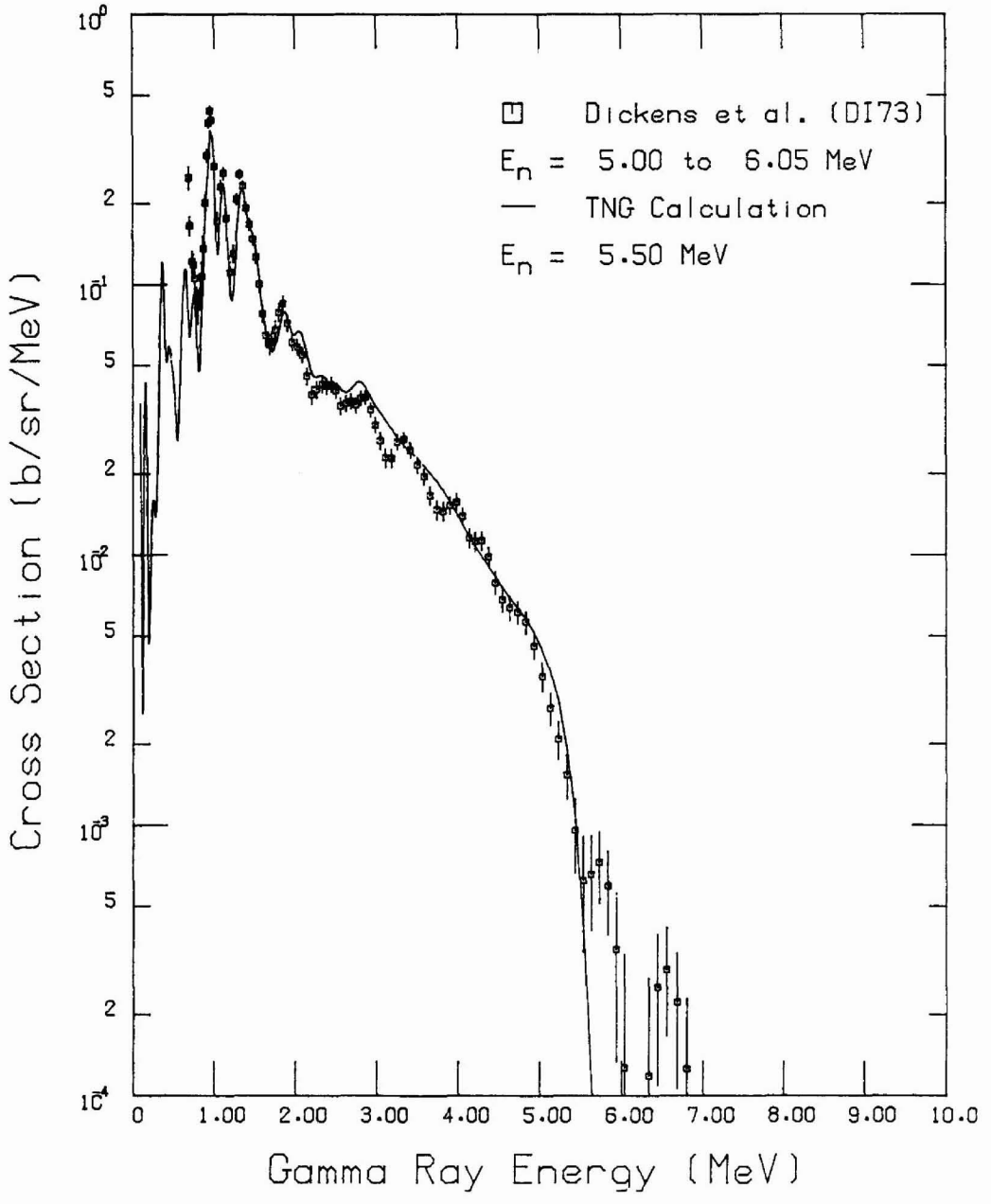

Fig. 64. Secondary gamma-ray spectra versus gamma-ray energy from the TNG calculation (incident energy E_n=5.5 MeV) compared with the data of Dickens et al. (DI73).

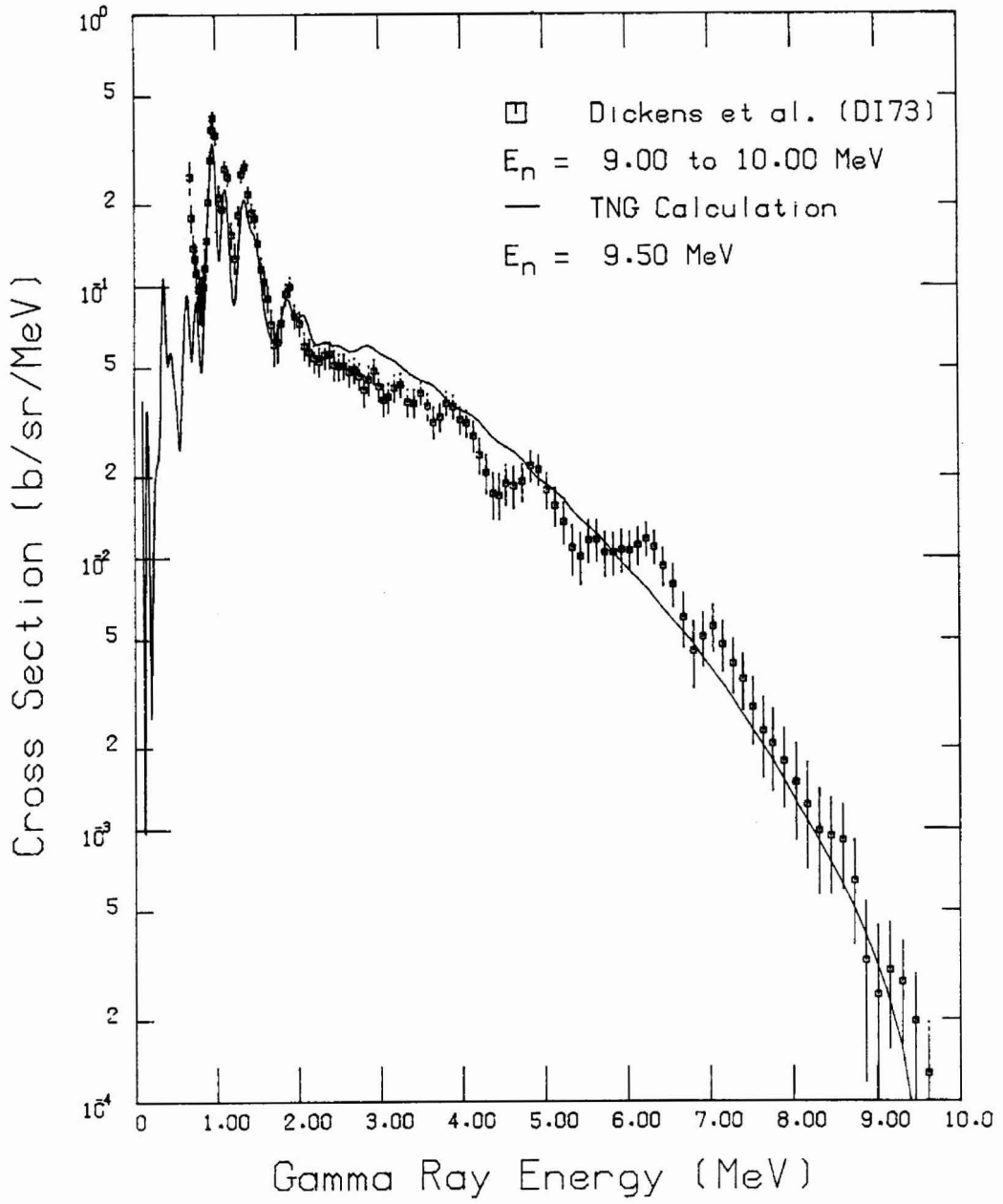

Fig. 65. Secondary gamma-ray spectra versus gamma-ray energy from the TNG calculation (incident energy E_n=9.5 MeV) compared with the data of Dickens et al. (DI73).

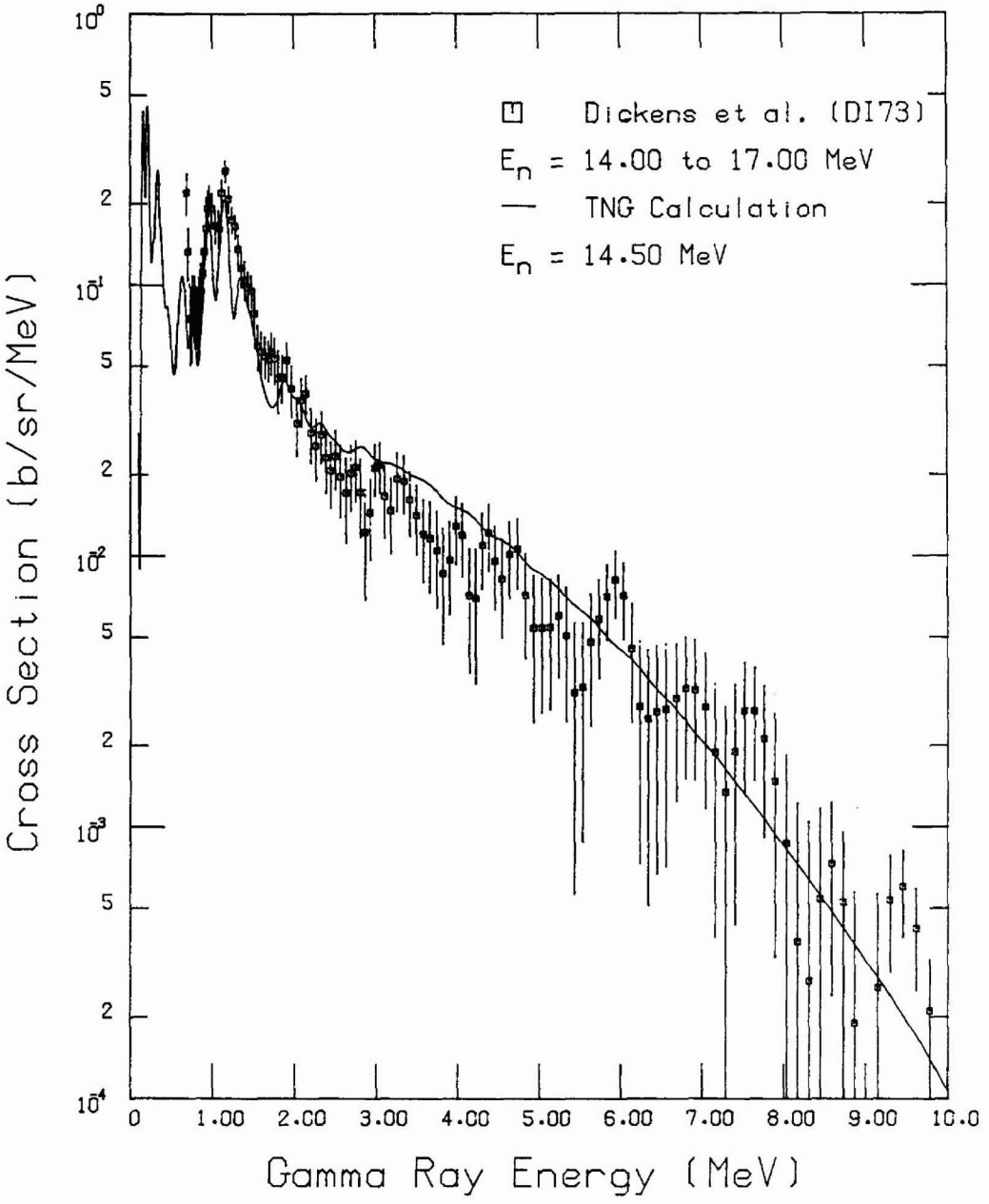

Fig. 66. Secondary gamma-ray spectra versus gamma-ray energy from the TNG calculation (incident energy E_n=14.5 MeV) compared with the data of Dickens et al. (DI73).

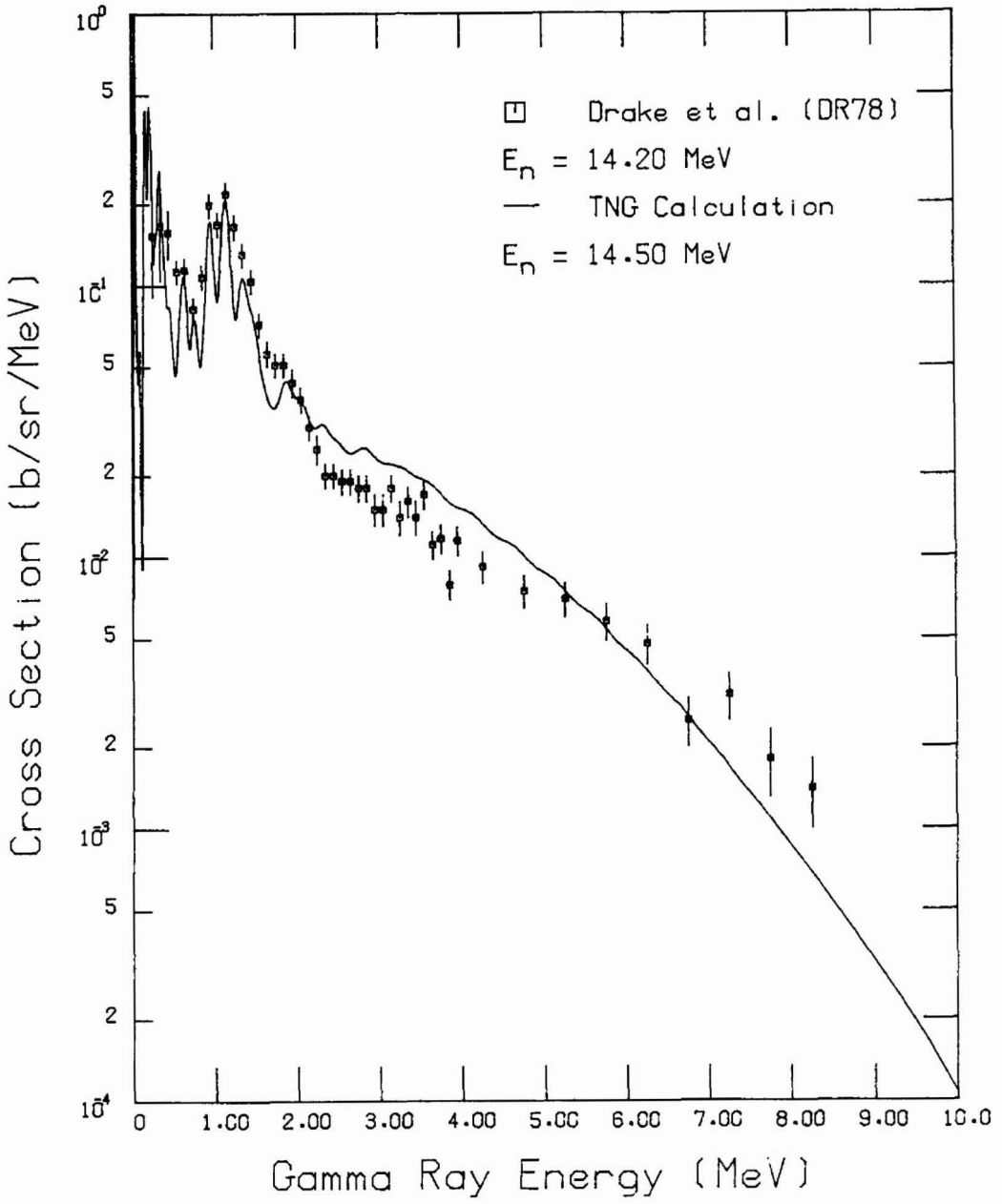

Fig. 67. Secondary gamma-ray spectra versus gamma-ray energy from the TNG calculation (incident energy E_n=14.5 MeV) compared with the data of Drake et al. (DR78).

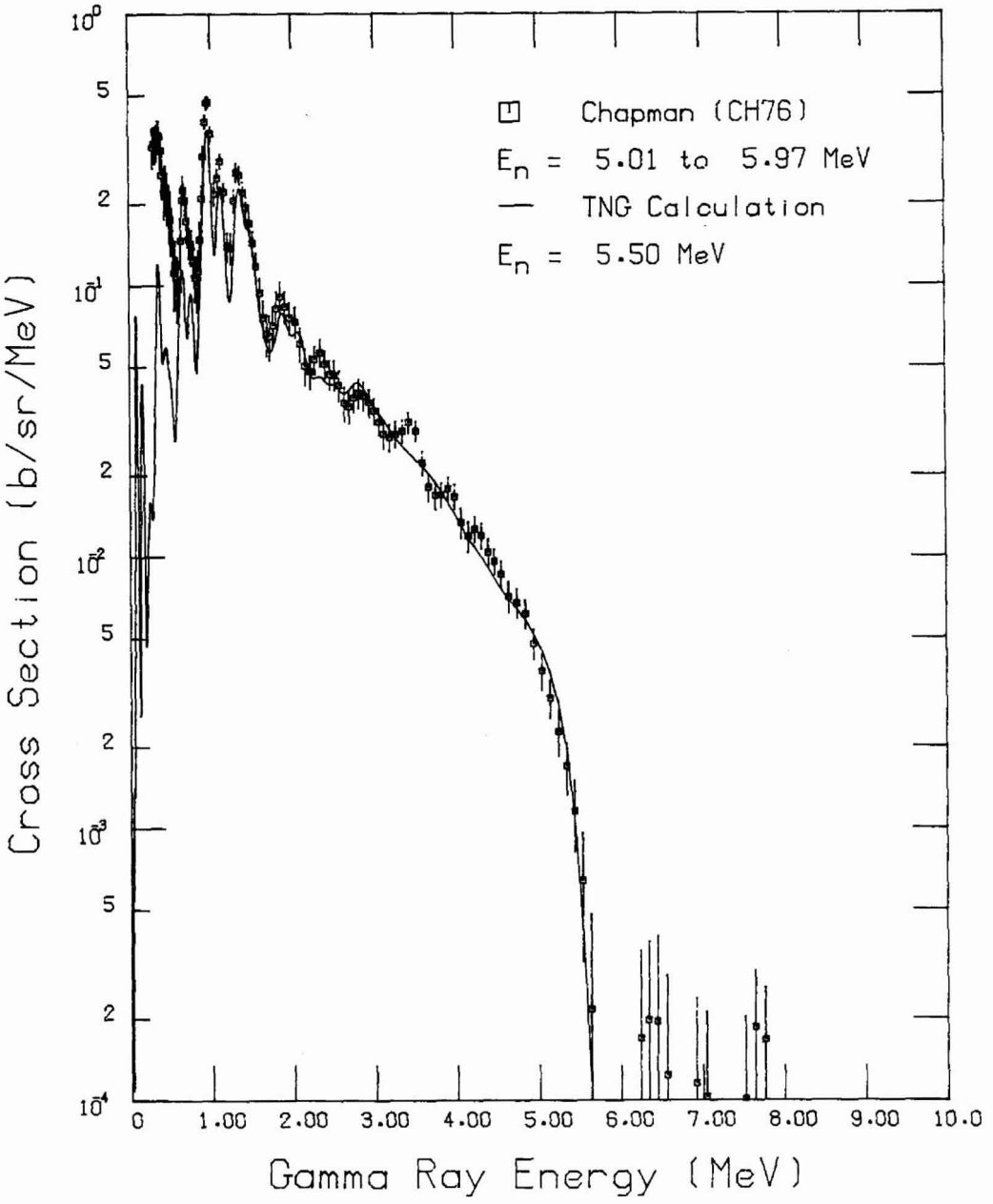

Fig. 68. Secondary gamma-ray spectra versus gamma-ray energy from the TNG calculation (incident energy E_n=5.5 MeV) compared with the data of Chapman (CH76).

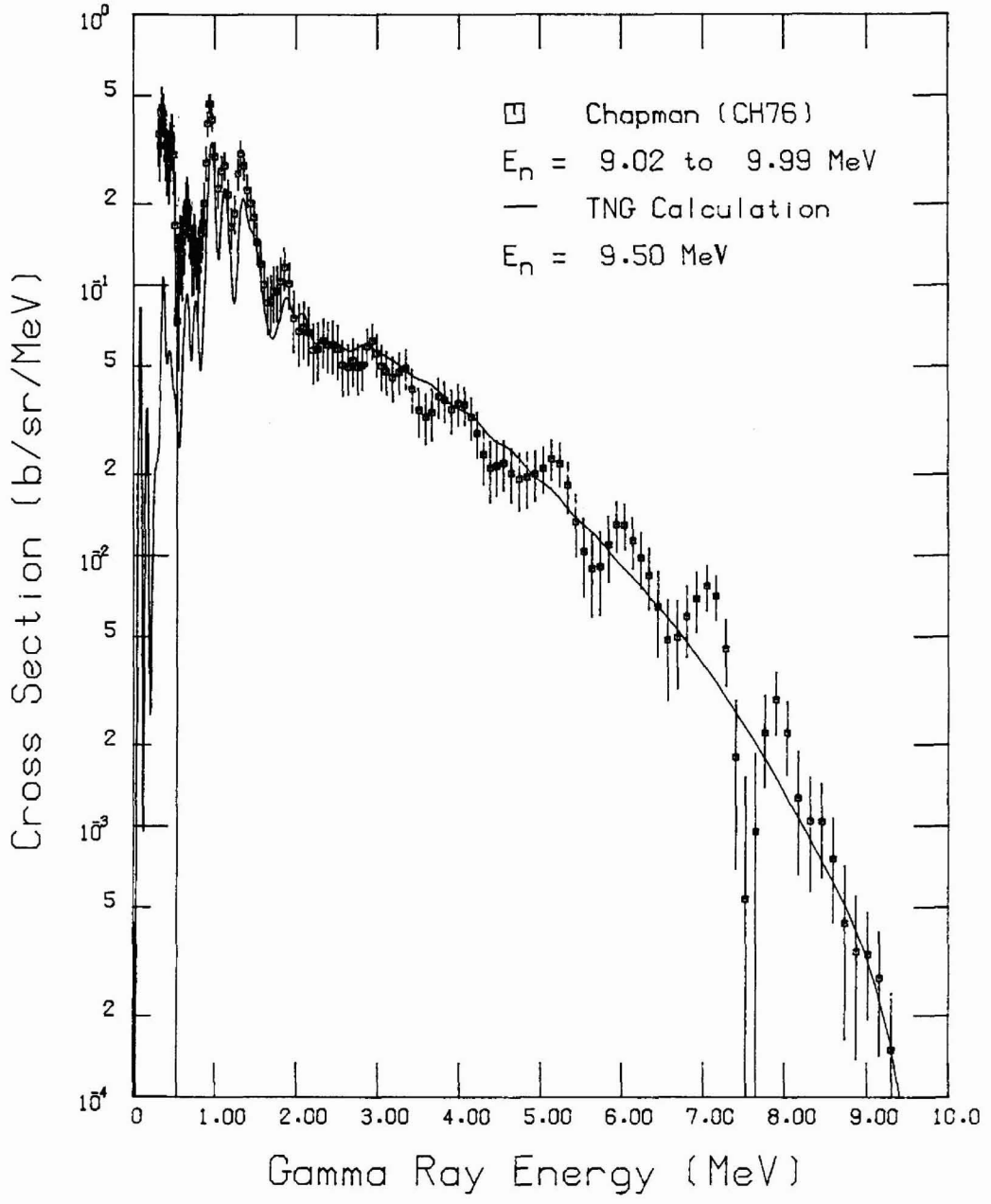

Fig. 69. Secondary gamma-ray spectra versus gamma-ray energy from the TNG calculation (incident energy E_n=9.5 MeV) compared with the data of Chapman (CH76).

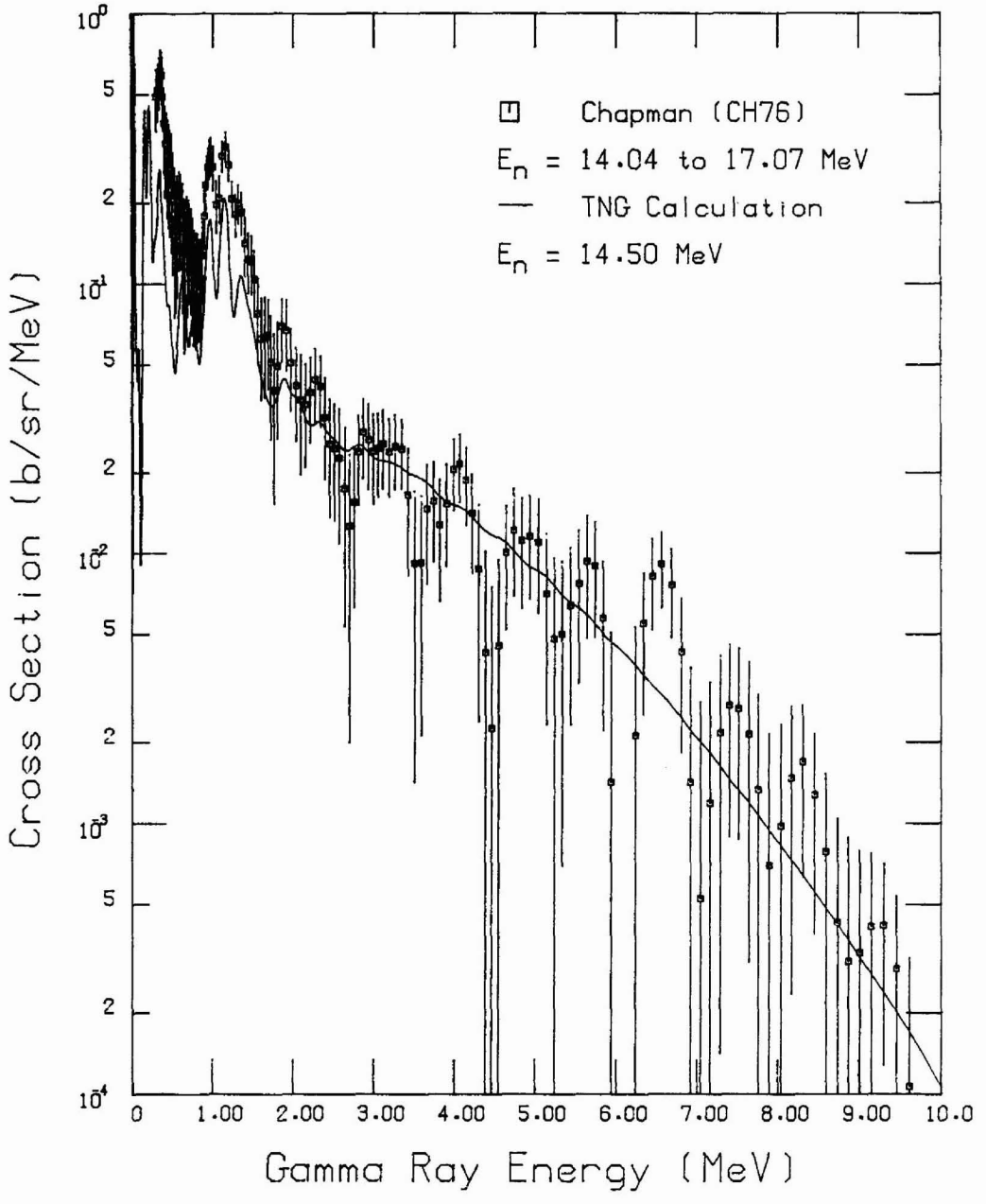

Fig. 70. Secondary gamma-ray spectra versus gamma-ray energy from the TNG calculation (incident energy E_n=14.5 MeV) compared with the data of Chapman (CH76).

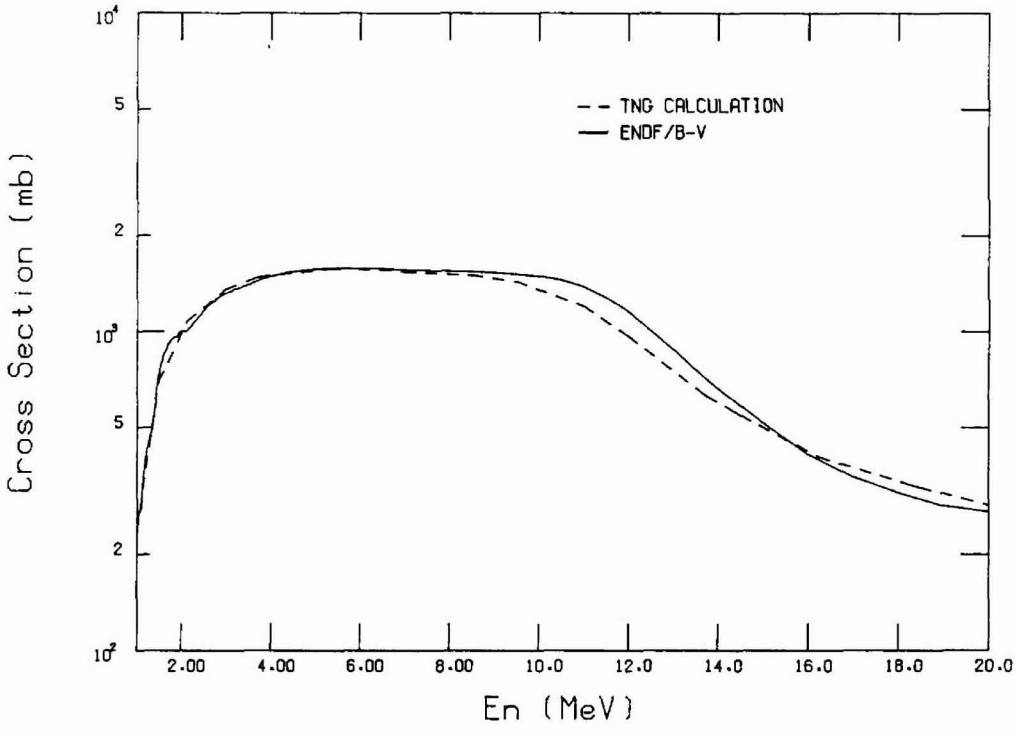

Fig. 71. Comparison of the TNG calculation with ENDF/B-V for the total inelastic scattering cross section.

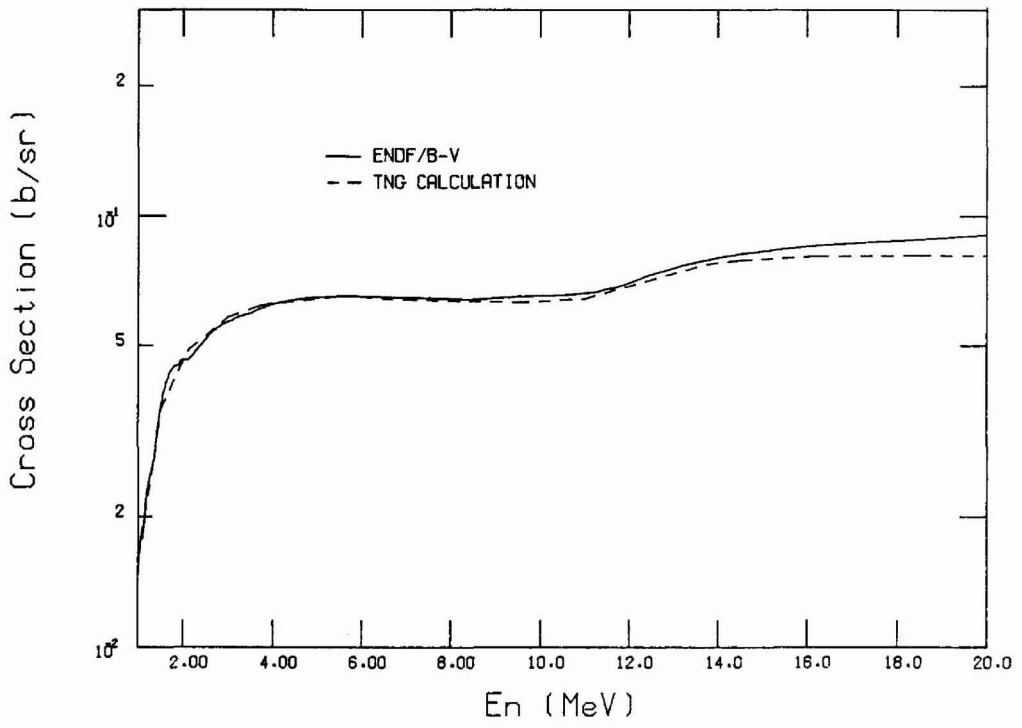

Fig. 72. Comparison of the TNG calculation with ENDF/B-V for the integrated yield of secondary neutrons as a function of incident neutron energy. The elastic contribution is not included.

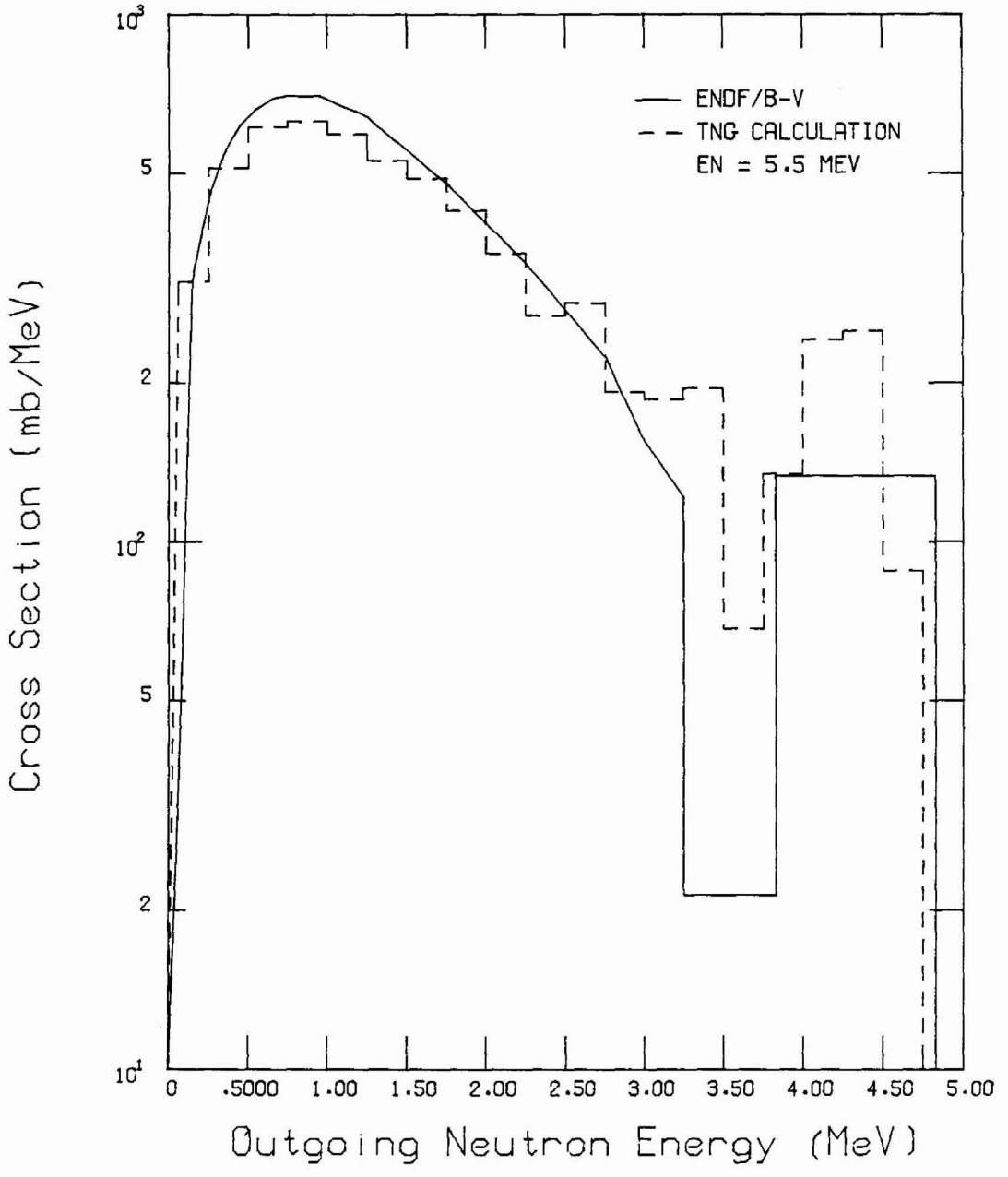

Fig. 73. Comparison of (n,xn) from ENDF/B-V with the TNG calculation for incident neutron energy of 5.5 MeV.

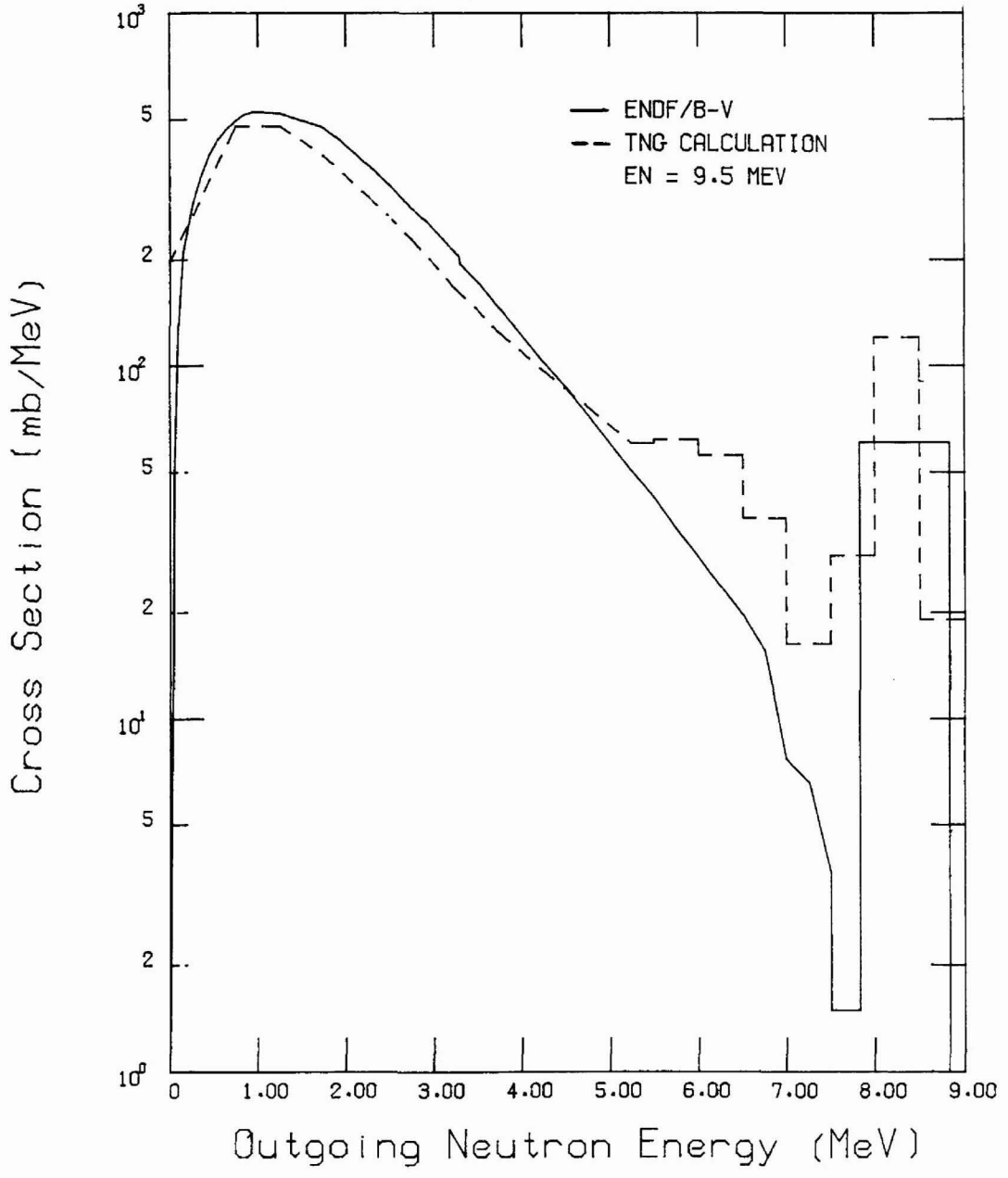

Fig. 74. Comparison of (n,xn) from ENDF/B-V with the TNG calculation for incident neutron energy of 9.5 MeV.

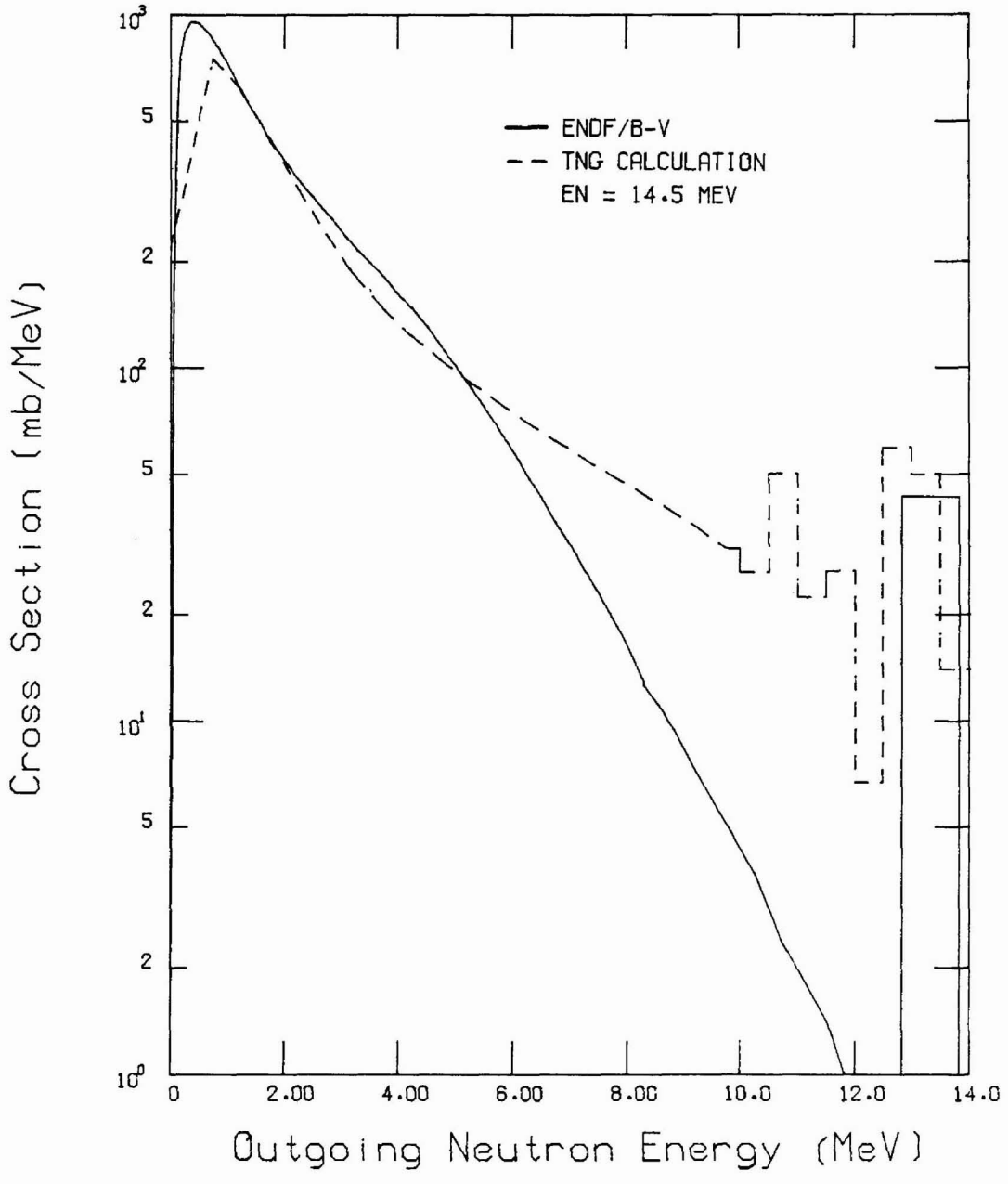

Fig. 75. Comparison of (n,xn) from ENDF/B-V with the TNG calculation for incident neutron energy of 14.5 MeV.

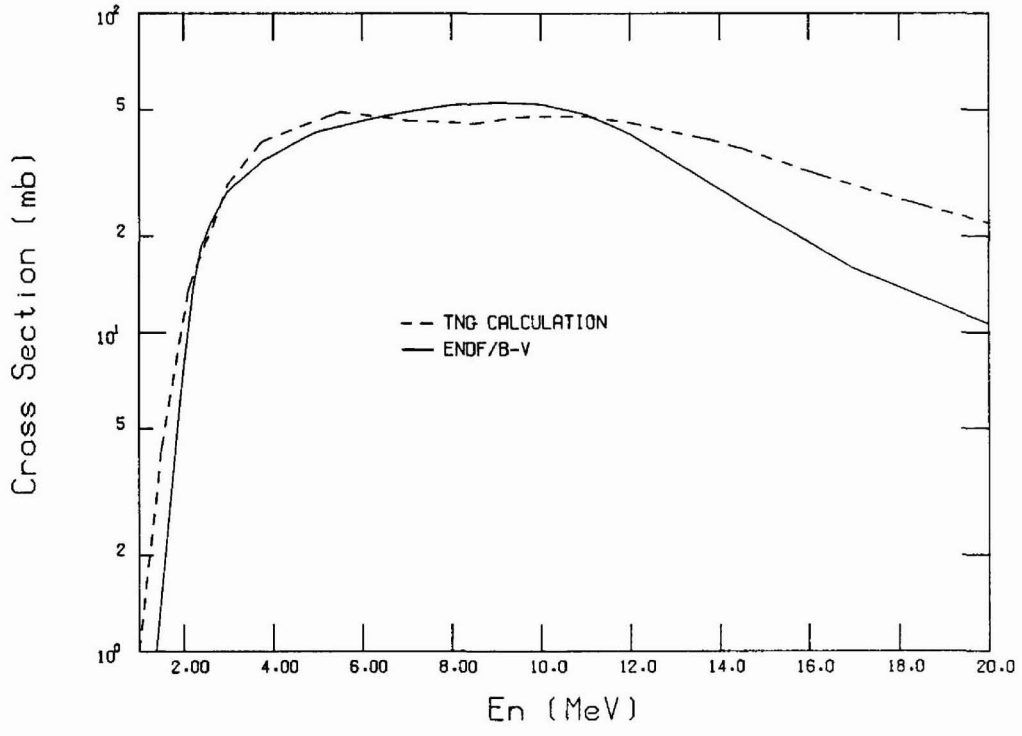

Fig. 76. Comparison of the TNG calculation with ENDF/B-V for the (n,p) cross section.

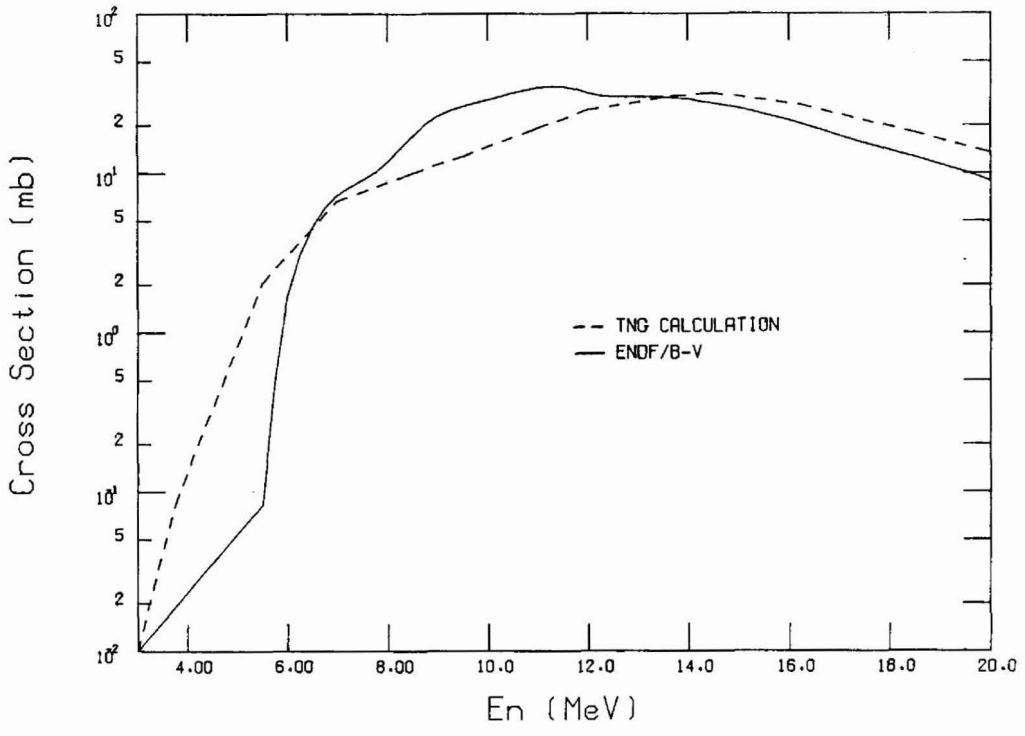

Fig. 77. Comparison of the TNG calculation with ENDF/B-V for the (n,α) cross section.

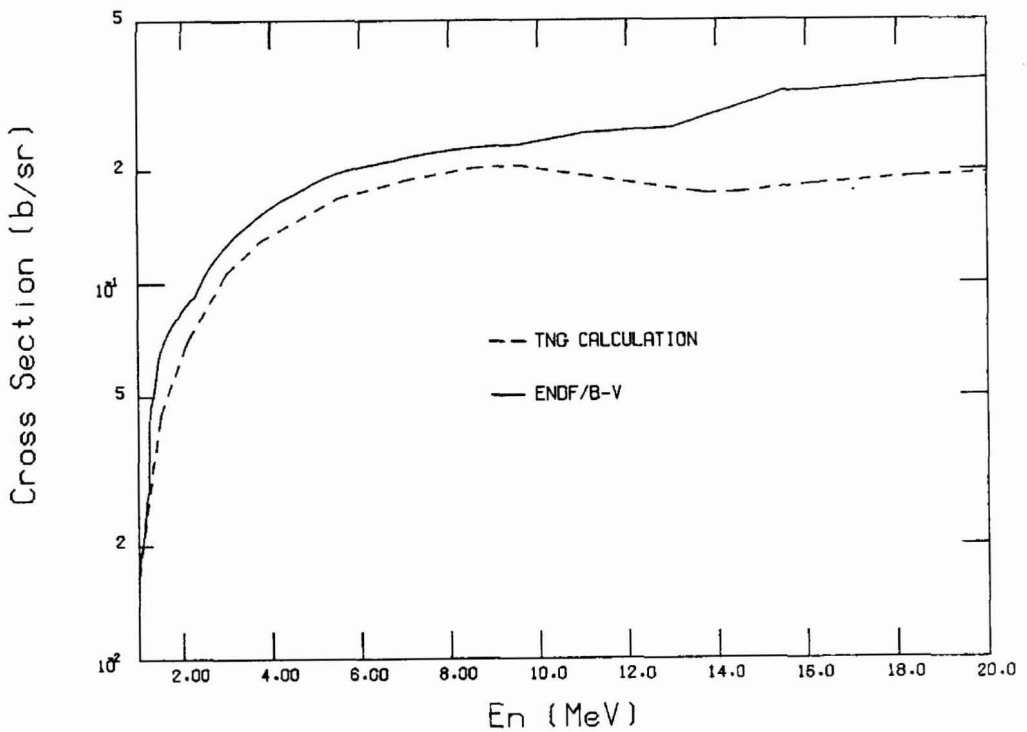

Fig. 78. Comparison of the TNG calculation with ENDF/B-V for the integrated yield of secondary gamma rays as a function of incident neutron energy.

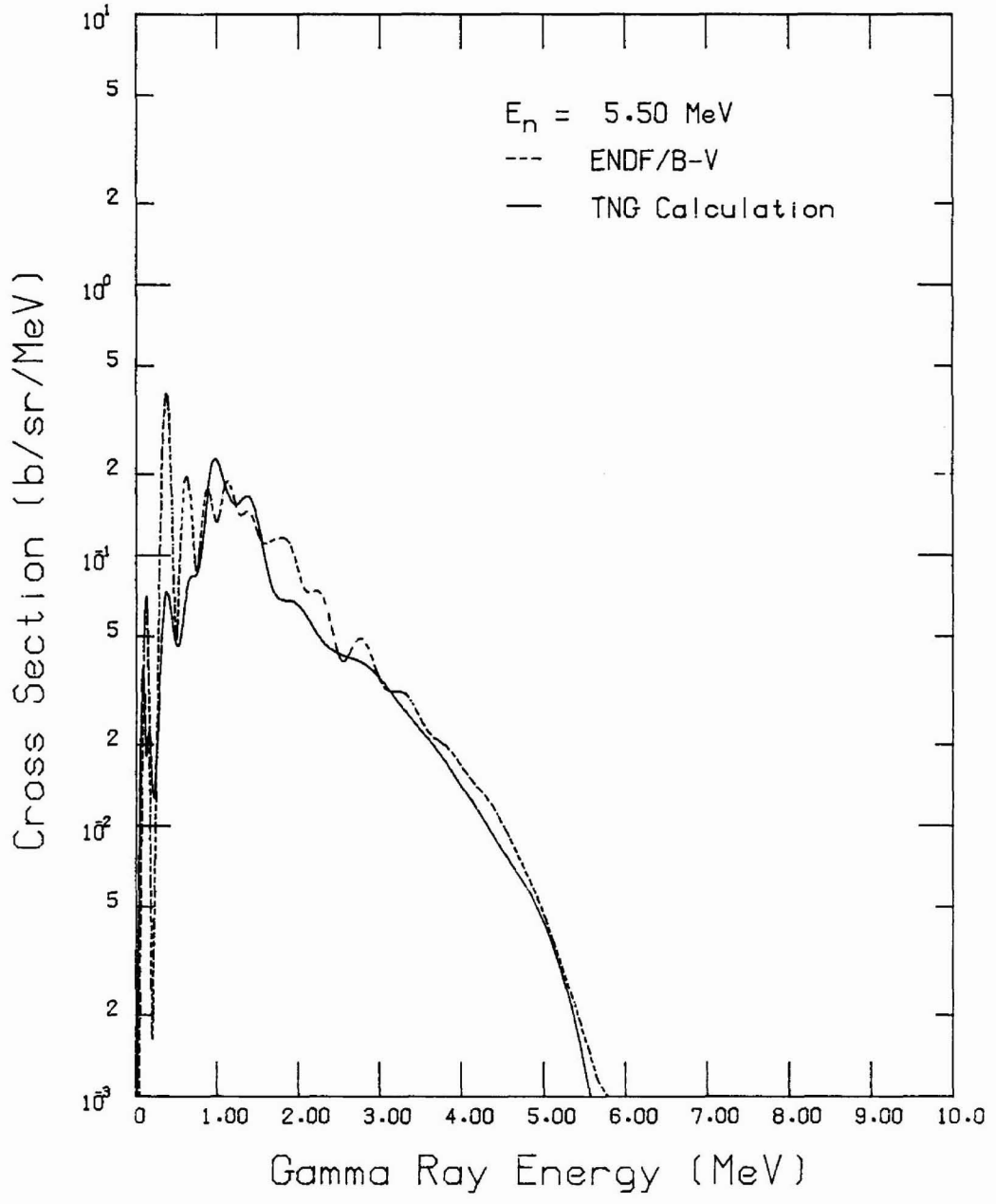

Fig. 79. Comparison of (n,xγ) from ENDF/B-V with the TNG calculation for incident neutron energy of 5.5 MeV.

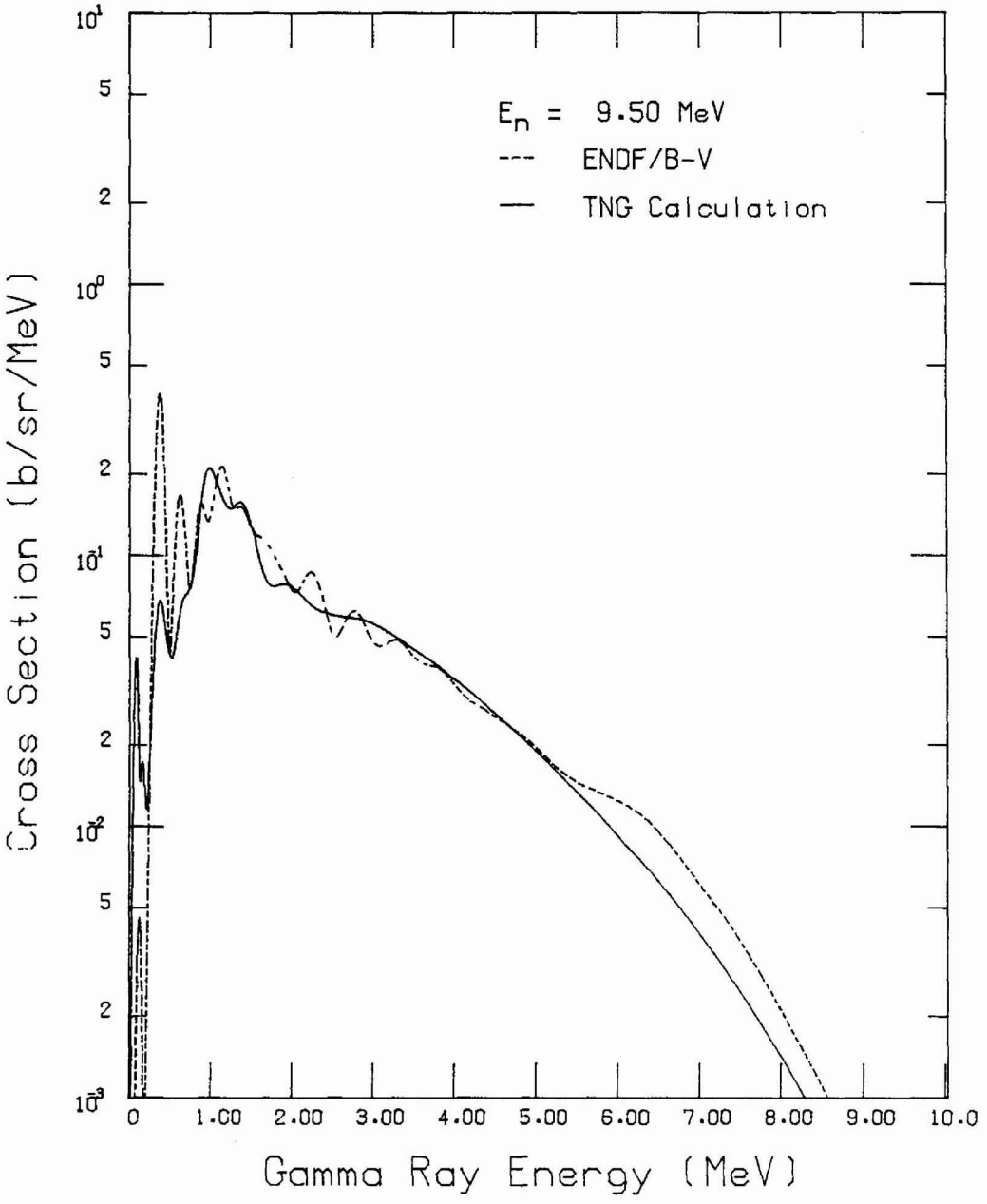

Fig. 80. Comparison of (n,xγ) from ENDF/B-V with the TNG calculation for incident neutron energy of 9.5 MeV.

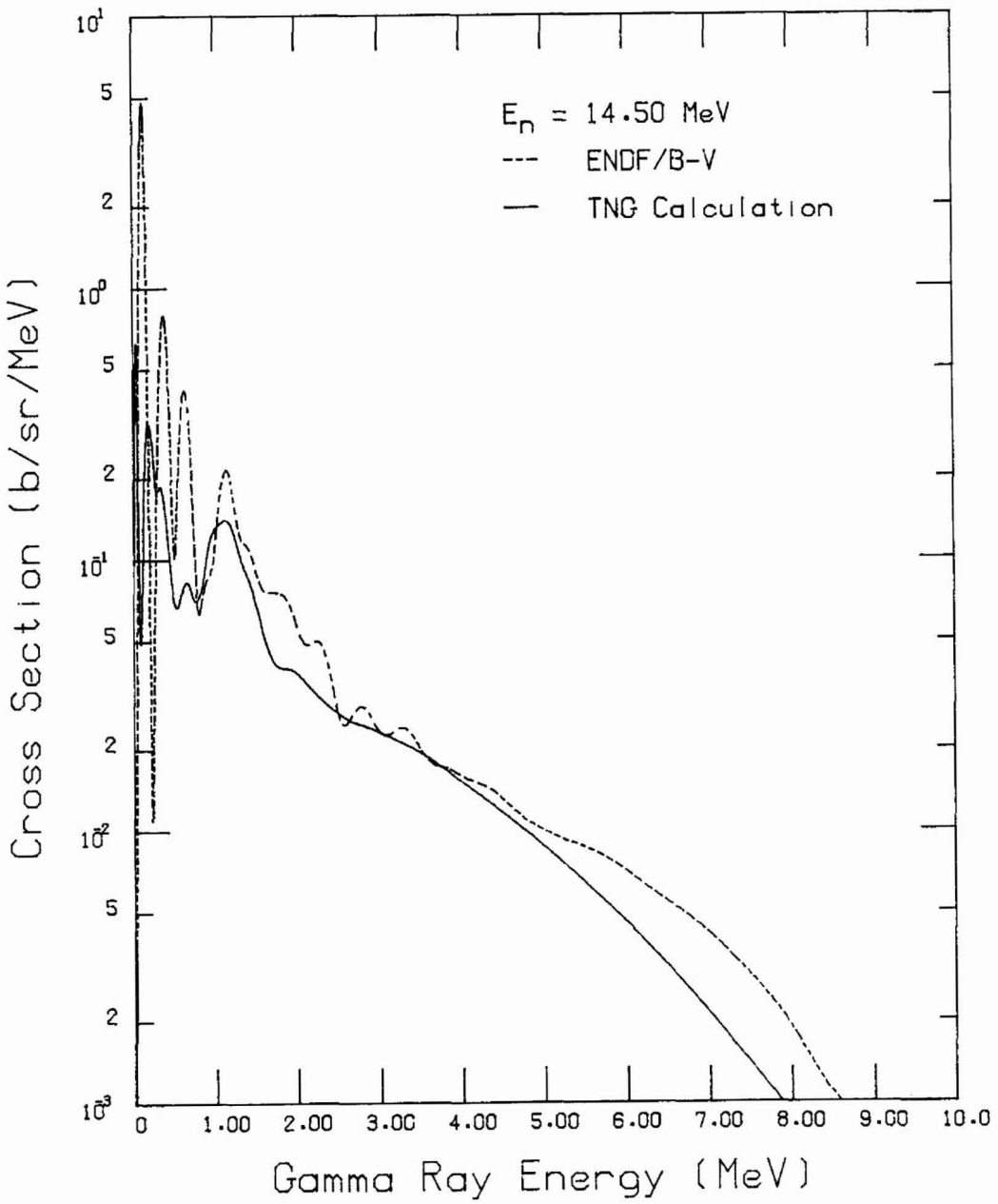

Fig. 81. Comparison of (n,xγ) from ENDF/B-V with the TNG calculation for incident neutron energy of 14.5 MeV.

REFERENCES

AB80. U. Abbondanno, A. Boiti, F. Demanins, C. Tuniz, and G. Nardelli, Nuclear Physics A345, 174 (1980).

AL61. D. L. Allan, Nuclear Physics, 24, 274 (April 1961).

AL75. E. Almen-Ramstrom, Aktiebolaget Atomenergi Repts. 503, Stockholm/Studsvik (April 1975).

AN67. B. Antolkovic, B. Holmqvist, and T. Wiedling, Ark. Fys., 33, 297 (1967).

AN68. M. F. Andreev and V. I. Serov, J. Yad. Fiz. 7, (4), 745 (April 1968).

AN70. G. V. Anikin and I. I. Kotukhov, Yadernaya Fizika, 12, (6), 1121 (1970).

AR80. E. D. Arthur and P. G. Young, "Evaluated Neutron-Induced Cross Sections for ^{54,56}Fe to 40 MeV", LA-8626-MS (ENDF-304), (December 1980).

AU75. R. L. Auble, Nuclear Data Sheets, 16, 351 (1975).

AU75a. R. L. Auble, Nuclear Data Sheets, 16, 1 (1975).

AU79. R. L. Auble, Nuclear Data Sheets, 28, 559 (1979).

AU79a. R. L. Auble, Nuclear Data Sheets, 28, 103 (1979).

BA51. R. C. Barrall, J. A. Holmes, and M. Silbergeld, Air Force Spec. Weap. Center Kirtland Report AFWL-TR-68-134 (March 1969).

BA58. W. P. Ball, M. MacGregor and R. Booth, Phys. Rev., 110, 1392 (1958).

BE55. J. R. Beyster, R. L. Henkel, R. A. Nobles, and J. M. Kister, Phys. Rev., 98, 1216 (1955).

BE56. J. R. Beyster, M. Walt, and E. W. Salmi, Phys. Rev., 104, 1319 (1956).

BE66. R. L. Becker, W. G. Guindon, and G. J. Smith, Nucl. Phys. 89, 154 (1966).

BE79. A. Begum, R. B. Galloway, and F. K. McNeil-Watson, Nuclear Phys., A332, 349 (1979).

BI75. T. Biro, S. Sudar, J. Csikai, and Z. Dezso, J. Inorg. Nucl. Chem., 37, 1583 (July 1975).

BL47. J. M. Blair, M. Deutsch, K. M. Griesen, A. O. Hanson, G. A. Linenberger, J. A. Miskel, R. F. Taschek, C. M. Turner, and J. H. Williams. Atomic Energy Centre, Dacca, Report AECD-2274 (1947).

BO58. R. Booth, W. Ball, and M. H. Mac Gregor, Phys. Rev., 112, 226 (1958).

BO59. T. W. Bonner and J. C. Slatterly, Phys. Rev., 113, 1088 (1959).

BO62. M. Bormann, S. Cierjacks, R. Langkau, and H. Neuert, Z. Phys., 166, 477 (February 1962).

BO63. M. Bormann, S. Cierjacks, E. Fretwurst, K. J. Giesicke, H. Neuert, and H. Pollehn, J. Z. Phys., 174, 1 (February 1963).

BO66. M. Bormann, F. Dreyer, U. Zielinski, European-American Nuclear Data Committee Documents (E)-66, 42 (February 1966).

BO69. M. Bormann and B. Lammers, Nuclear Phys., A130, 195 (June 1969).

BO72. M. Bormann, W. Schmidt, V. Schroeder, W. Scobel, and U. Seebeck, Nuclear Physics, A186, 65 (May 1972).

BR52. J. E. Brolley, Jr., J. L. Fowler, and L. K. Schlacks, Phys. Rev., 88, 618 (November 1952).

BR62. E. T. Bramlitt, R. W. Fink, D. G. Gardner, and A. Poularikas, Phys. Rev., 125, 297 (1962).

BR63. E. T. Bramlitt and R. W. Fink, Phys. Rev., 131, 2649 (September 1963).

BR78. E. Browne, J. M. Dairiki, R. E. Doebler, A. A. Shihab-Eldin, L. J. Jardine, J. K. Tuli, A. B. Buyrn, Table of Isotopes, Seventh Edition, Edited by C. M. Lederer and V. S. Shirley, John Wiley and Sons, Inc., N.Y. (1978).

CH66. A. K. Chaubey and M. L. Sehgal, Phys. Rev., 152, 1055 (December 1966).

CH70. S. N. Chaturvedi and R. Prasad, Nuclear and Solid State Physics Symposium, Madurai, India, 2, 615 (December 1970).

CH76. G. T. Chapman, "The Cu (n,) Reaction Cross Section for Incident Energies Between 0.2 and 20.0 MeV", ORNL/TM-5215 (1976).

CL69. I. G. Clator, J. Diss. Abstracts B, 30, 2850 (December 1969).

CO56. A. V. Cohen and P. H. White, Nuclear Physics, 1, 73 (February 1956).

CO58. J. H. Coon, R. W. Davis, H. E. Felthauser, D. B. Nicodemus, Phys. Rev., 111, 250 (1958).

CO59. L. Colli, U. Facchini, I. Iori, M. G. Marcazzan, and A. M. Sona, J. Nuovo Cimento, 13, 730 (August 1959).

CO68. J. Colditz and P. Hille, J. Ang. Oesterr. Akad. Wiss. Math-Naturwiss. Kl., 105, 236 (June 1968).

CS83. CSISRS Library, National Nuclear Data Center, Brookhaven National Laboratory, Upton, NY 11973.

CU68. P. Cuzzocrea, E. Perillo, and S. Notarrigo, J. Nuovo Cimento, B54, 53 (March 1968).

CZ60. B. Czapp and H. Vonach, J. Anz. Oesterr. Akad. Wiss., Math-Naturwiss, Kl., 97, 13 (January 1960).

DA56. R. B. Day, Phys. Rev., 102, 167 (1956).

DE61. Yu. G. Degtyarev and V. G. Nadtochii, Atomnaja Energija, 11, 397 (1961).

DI70. M. Diksic, P. Strohal, G. Peto, P. Bornemisza-Pauspertl, I. Hunyadi and J. Karolyi, J. Acta. Phys. Ac. Sci. Hung., 28, 257 (January 1970).

DI73. J. K. Dickens, T. A. Love, and G. L. Morgan, "Gamma-Ray Production Due to Neutron Interactions with Copper for Incident Neutron Energies Between 1.0 and 20.0 MeV: Tabulated Differential Cross Sections", ORNL-4846 (1973).

DI83. J. K. Dickens, Nuclear Physics, A401, 189 (1983).

DR78. D. M. Drake, E. D. Arthur, and M. G. Silbert, Nuclear Science and Engineering, 65, 49-64 (1978).

FA68. U. Facchini and E. Saetta-Menichella, Energia Nucleare 15, 54 (1968).

FE60. J. M. Ferguson and W. E. Thompson, Phys. Rev., 118, 228 (April 1960).

FE70. J. Felsteiner and R. Serfaty, Nuclear Physics, A148, 428 (1970).

FO50. J. L. Fowler and J. M. Slye, Jr., Phys. Rev., 77, 787 (March 1950).

FU73. E. G. Fuller, H. M. Gerstenberg, H. Vander Molen, and T. C. Dunn, "Photonuclear Reaction Data, 1973", U.S. Dept. of Commerce, National Bureau of Standards (March 1973).

FU76. C. Y. Fu, Atomic Data and Nuclear Data Tables 17, 127 (1976).

FU80. C. Y. Fu, "A Consistent Nuclear Model for Compound and Precompound Reactions with Conservation of Angular Momentum," Proc. Int. Conf. Nuclear Cross Sections for Technology, Knoxville, TN, Oct. 22-26, 1979, NBS-594, p. 757, U.S. National Bureau of Standards. Also, ORNL/TM-7042 (1980).

FU80a. C. Y. Fu, "Development and Applications of Multi-Step Hauser-Feshbach/Pre-Equilibrium Model Theory," Symp. Neutron Cross Sections from 10 to 50 MeV, Upton, N.Y., May 12-14, 1980, BNL-NCS-51425, p. 675, Brookhaven National Laboratory.

FU82. C. Y. Fu, "Summary of ENDF/B-V Evaluations for Carbon, Calcium, Iron, Copper, and Lead and ENDF/B-V Revision 2 for Calcium and Iron," ORNL/TM-8283, ENDF-325 (1982).

FU82a. C. Y. Fu and D. M. Hetrick, "Experience in Using the Covariances of Some ENDF/B-V Dosimetry Cross Sections: Proposed Improvements and Addition of Cross-Reaction Covariances," Proc. Fourth ASTM-EURATOM Symp. on Reactor Dosimetry, Gaithersburg, Maryland, March 22-26, 1982, p. 877, U.S. National Bureau of Standards.

FU80b. C. Y. Fu, "Evaluation of Photon Production from Neutron-Induced Reactions," Proc. of the Conference on Nuclear Data Evaluation Methods and Procedures, Upton, N.Y., September 22-25, 1980, BNL-NCS-51363, Vol. II, p. 753, Brookhaven National Laboratory.

GA80. U. Garuska, J. Dresler, and H. Malecki, Inst. Badan Jadr (Nuclear Research), Swierk-Warsaw, Rept. INR-1871, 15 (July 1980). A. Gilbert and A. G. W. Cameron, Can. J. Physics, 43, 1446 (1965).

GR78. S. M. Grimes, R. C. Haight, K. R. Alvar, H. H. Barschall, and R. R. Bouchers, Lawrence Rad. Lab. Report UCRL-81802 (October 1978).

GR79. S. M. Grimes, R. C. Haight, K. R. Alvar, H. H. Barschall, and R. R. Borchers, Phys. Rev. C19, 2127 (1979).

HA68. S. S. Hasan, A. K. Chaubey, and M. L. Sehgal, J. Nuovo Cimento B, 58, 402 (December 1968).

HA76. F. I. Habbani and A. H. Jiggins, Nucl. Instrum. Methods, 134, 545 (1976).

HA77. R. C. Haight and S. M. Grimes, Lawrence Livermore Laboratory Report UCRL-80235 (1977).

HA79. M. L. Halbert, Nuclear Data Sheets, 26, 5 (1979).

HA79a. M. L. Halbert, Nuclear Data Shetts, 28, 179 (1979).

HE75. D. Hermsdorf, A. Meister, S. Sassonoff, D. Seeliger, K. Seidel, and F. Shahin, Zentralinstitut Fur Kernforschung Rossendorf Bei Dresden, ZfK-277 (U), (1975).

HI58. R. W. Hill, Phys. Rev. 109, 2105 (1958).

HI78. Y. Hino, T. Yamamoto, T. Saito, Y. Arai, S. Itagaki and K. Sugiyama, J. Nuclear Science Technology, 15, 85 (1978).

HI80. Y. Hino, T. Yamamoto, S. Itagaki, and K. Sugiyama, "Nuclear Cross Sections for Technology," NBS Special Publication 594, pp. 408-412, J. L. Fowler, C. H. Johnson, and C. D. Bowman, Eds., U.S. National Bureau of Standards (1980).

HO64. B. Holmqvist and T. Wiedling, "Inelastic Neutron Scattering Cross Sections of ^{63}Cu and ^{65}Cu in the Energy Region 0.7 to 1.4 MeV," AE-150 (August 1964).

HO69. B. Holmqvist and T. Wiedling, Atomic Energy Company, Studsvik, Nykoping, Sweden, Report AE-366, (1969).

JA78. R. A. Jarjis, J. of Physics, Pt. G, 4, 3, 445 (1978).

JO59. A. E. Johnsrud, M. G. Silbert, and H. H. Barschall, Phys. Rev., 116, 927 (1959).

JO69. B. Joensson, K. Nyberg, and I. Bergqvist, J. Arkiv Foer Fysik, 39, 295 (April 1969).

KA79. K. Kayashima, A. Nagao, and I. Kumabe, European-American Nuclear Data Committee Documents - 61U, 94 (September 1979).

KI74. W. E. Kinney and F. G. Perey, "Elastic and Inelastic Scattering Cross Sections from 5.5 to 8.5 MeV," Report ORNL-4908 (February 1974).

KO58. V. N. Kononov, Yu. Ya. Stavisskii, and V. A. Tolstikov, J. Atomnaja Energija, 5, 564 (1958).

KO60. D. R. Koehler and W. L. Alford, Bull. Amer. Phys. Soc., 5, 443 (1960).

KU72. P. D. Kunz, "Distorted Wave Code DWUCK72," University of Colorado, unpublished (1972).

LA80. D. C. Larson, "ORELA Measurements to Meet Fusion Energy Neutron Cross Section Needs," Proc. Symposium on Neutron Cross-Sections from 10 to 50 MeV, BNL-NCS-51245, Brookhaven National Laboratory (July 1980).

LE58. A. I. Leipunsky, O. D. Kazachkovsky, G. Y. Artyukhov, A. I. Baryshnikov, T. S. Belanova, V. N. Galkov, Yu. Ya. Stavisskii, E. A. Stumpur, and L. E. Sherman, Second Internat. At. En. Conf., Geneva, 15, 50 (2219) (September 1958).

LE72. O. F. Lemos, "Diffusion Elastique de Particules Alpha de 21 a 29.6 MeV sur des Noyaux de la Region Ti-Zn," Orsay report, Series A, No. 136 (1972).

LI65. H. Liskien and A. Paulsen, J. of Nuclear Energy, 19, 73 (February 1965).

LY59. W. S. Lyon and R. L. Macklin, Phys. Rev., 114, 1619 (1959).

MA57. R. L. Macklin, N. H. Lazar, and W. S. Lyon, Phys. Rev., 107, 504 (1957).

MA72. G. N. Maslov, F. Nasyrov, and N. F. Pashkin, Union of Sov. Social. Republics, Rept. YK-9, 50 (1972).

MC60. J. H. McCrary and I. L. Morgan, Bull. Amer. Phys. Soc., 5, 246(HA5) (April 1960).

MC66. A. L. McCarthy and G. M. Crawley, Phys. Rev., 150, 935 (1966).

MI67. B. Mitra, Nuclear and Solid State Physics Symposium, Kanpur, 367 (February 1967).

MO79. G. L. Morgan, "Cross Sections for the Cu(n,xn) and Cu(N,xα) Reactions Between 1 and 20 MeV," ORNL-5499, ENDF-273 (1979).

MU81. S. F. Mughabghab, M. Divadeenam, and N. E. Holden, "Neutron Cross Sections, Vol. 1, Neutron Resonance Parameters and Thermal Cross Sections, Part A, Z=1-60," Academic Press (1981).

NA66. W. Nagel, J. Nuclear Energy, 20, 475 (June 1966).

ND83. "Compilation of Requests for Nuclear Data," Compiled and edited by the National Nuclear Data Center for the DOE Nuclear Data Committee, BNL-NCS-51572, DOE/NDC-28/U, January, 1983.

NG80. P. N. NGOC, S. Gueth, F. Deak, and A. Kiss, All Union Conf. on Neutron Physics, Kiev, USSR (September 1980).

NI61. K. Nishimura, J. Phys. Soc. Japan, 16, 355 (1961).

NI65. K. Nishimura, K. Okano, and S. Kikuchi, Nuclear Physics 70, 421 (1965).

PA55. M. V. Pasechnik, First Internat. At. En. Conf., Geneva, 2, 3(P/714) (1955).

PA58. M. V. Pasechnik, I. F. Barchuk, I. A. Totskii, V. I. Strizhak, A. M. Korolov, Y. V. Hofman, G. N. Lovchikova, E. A. Koltynin, and G. B. Yankov, Second Internat. At. En. Conf., Geneva, 15, 18(P/2030) (1958).

PA65. A. Paulsen and H. Liskien, J. Nukleonik, 7, 117 (March 1965).

PA67. A. Paulsen and H. Liskien, J. Nukleonik, 10, 91 (July 1967).

PA67a. A. Paulsen, J. Z. Phys., 205, 226 (August 1967).

PE58. J. L. Perkin, L. P. O'Connor, and R. F. Coleman, Proc. Phys. Soc. London, 72, 505 (1958).

PE63. F. G. Perey, Phys. Rev., 131, 745 (1963).

PE67a. G. Peto, Z. Milligy, and I. Hunyadi, J. Nucl. Energy, 21, 797 (October 1967).

PE67. F. G. Perey, Computer code GENOA, ORNL, unpublished (1967).

PO61. H. Pollehn and H. Neuert, Z. Naturforsch. A, 16, 227 (1961).

PO61a. A. Poularikas, S. Umemoto, E. Bramlitt, D. G. Gardner, U. of Arkansas, Fayetteville, Ark., Report A-ARK-61, 7 (February 1961).

PR60. I. L. Preiss, R. W. Fink, and D. G. Gardner, U. of Arkansas, Fayetteville, Ark., Rpt. A-ARK-60, 2 (January 1960).

PR61. R. J. Prestwood and B. P. Bayhurst, Phys. Rev., 121, 1438 (March 1961).

QA74. S. M. Qaim and G. Stoecklin, Euratom Report - 5182E, 939 (September 1974).

QA77. S. M. Qaim and N. I. Molla, Nucl. Phys., A283, 269 (June 1977).

RA62. L. A. Rayburn, Bull. Amer. Phys. Soc., 7, 335(TA12) (April 1962).

RA63. L. A. Rayburn, Phys. Rev., 130, 731 (1963).

RO67. W. L. Rodgers, E. F. Shrader, and J. T. Lindow, Chicago Operations Office, AEC, Contract Reports - 1573-33, 2 (1967).

RO77. V. C. Rogers, D. R. Dixon, C. G. Hoot, D. Costello, and V. J. Orphan, Nucl. Sci. Eng., 62, 716 (1977).

RY78. T. B. Ryves, P. Kolkowsky, and K. J. Zieba, J. Metrologia, 14, 3, 127 (June 1978).

SA65. D. C. Santry and J. P. Butler, Can. J. Phys., 44, 1183 (1965).

SA75. O. A. Salnikov, G. N. Lovchikova, G. V. Kotelnikova, A. M. Trufanov, N. I. Fetisov, "Energy Spectra of Inelastically Scattered Neutrons for Cr, Mn, Fe, Co, Ni, Cu, Y, Zr, Nb, W, and Bi," IAEA Nuclear Data Section, Karntner Ring 11, A-1010 Vienna (July 1974).

SL83. G. G. Slaughter and J. K. Dickens, Nucl. Sci. Eng., 84, 395 (1983).

ST63. Yu. Ya. Stavisskii and V. A. Tolstikov, J. Nucl. Energy, 17, 579 (1963).

TA55. H. L. Taylor, O. Lonsjo, and T. W. Bonner, Phys. Rev., 100, 174 (1955).

TH63. D. B. Thomson, Phys. Rev., 129, 1649 (1963).

TO66. V. A. Tolstikov, V. P. Koroleva, V. E. Kolesov, and A. G. Dovbenko, J. Sov. At. Energy, 21, 665 (1966).

TO66a. V. A. Tolstikov, V. E. Kolesov, A. G. Dovbenko, and Yu. Ya. Stavisskii, J. Nucl. Energy, 20, 86 (1966).

TU65. A. B. Tucker, J. T. Wells, and W. E. Meyerhoff, Phys. Rev., 137, 1181 (1965).

VE59. J. F. Vervier, Nucl. Phys., 9, 569 (January 1959).

VO80. H. Vonach, A. Chalupka, F. Wenninger, and G. Staffel, "Measurement of the Angle-Integrated Secondary Neutron Spectra from Interaction of 14 MeV Neutrons with Medium and Heavy Nuclei," Proc. Symposium on Neutron Cross-Sections from 10 to 50 MeV, BNL-NCS-51245, Brookhaven National Laboratory (July 1980).

WA54. M. Walt and H. H. Barschall, Phys. Rev. 93, 1062 (1954).

WI49. G. C. Wick, Phys. Rev., 75, 1459 (1949).

WI78. G. Winkler, Nucl. Sci. Eng., 67, 2, 260 (August 1978).

WI80. G. Winkler, D. L. Smith, ad J. W. Meadows, Nucl. Sci. Eng., 76, 30 (October 1980).

ZA68. G. G. Zaikin, I. A. Korzh, N. T. Skljar, and I. A. Totskij, J. Atomnaja Energija, 25, (6), 526, (December 1968).

ORNL/TM-9083
ENDF-337

INTERNAL DISTRIBUTION

1. R. G. Alsmiller, Jr.
2. H. P. Carter/G. E. Whitesides/ CS X-10 Library
3. J. K. Dickens
4. P. W. Dickson, Jr. (Consultant)
5-9. C. Y. Fu
10. T. A. Gabriel
11. G. H. Golub (Consultant)
12-16. D. M. Hetrick
17. H. J. C. Kouts (Consultant)
18-21. D. C. Larson
22. N. M. Larson
23. F. C. Maienschein
24. B. F. Maskewitz
25. G. S. McNeilly
26. L. S. Abbott
27. B. D. Murphy
28. M. R. Patterson
29. R. W. Peelle
30. F. G. Perey
31. R. W. Roussin
32. R. T. Santoro
33. R. R. Spencer
34. D. Steiner (Consultant)
35. Central Research Library Document Reference Section
36. K-25 Plant Library
37-38. Laboratory Records Department
39. ORNL Patent Office
40. Laboratory Records (RC)

EXTERNAL DISTRIBUTION

41. E. D. Arthur, T-2, MS243, Los Alamos National Laboratory, P.O. Box 1663, Los Alamos, NM 87545.
42. S. E. Berk, G234, Division of Development and Technology Office of Fusion Energy, USDOE, Washington, DC 20545.
43. M. R. Bhat, Building 197D, National Nuclear Data Center, Brookhaven National Laboratory, Upton, NY 11973.
44. Chief, Mathematics and Geoscience Branch, DOE, Washington, DC 20545.
45. Herbert Goldstein, 211 Mudd Columbia University, 520 West 120th St., New York, NY 10027.
46. R. C. Haight, P.O. Box 808, L-405, Lawrence Livermore National Laboratory, Livermore, CA 94550.
47. Robert MacFarlane, T-2, MS243, Los Alamos National Laboratory, P.O. Box 1663, Los Alamos, NM 87545.
48. F. M. Mann, W/A-4, Westinghouse Hanford, P.O. Box 1970, Richland, WA 99352.
49. G. L. Morgan, Los Alamos National Laboratory, P.O. Box 1663, Group P-15, MS D406, Los Alamos, NM 87545.
50. J. N. Rogers, Division 8324, Sandia Laboratories, Livermore, CA 94550.
51. Robert Schenter, Westinghouse Hanford, P.O. Box 1970, Richland, WA 99352.
52. D. L. Smith, Building 314, Applied Physics Division, Argonne National Laboratory, 9700 South Cass Avenue, Argonne, IL 60439.

53. Stanley Whetstone, Division Nuclear Sciences, Office of Basic Energy Sciences, U.S. DOE, Washington, DC 20545.
54. Phillip Young, T-2, MS-243, Los Alamos National Laboratory, P.O. Box 1663, Los Alamos, NM 87545.
55. Office of Assistance Manager for Energy Research and Development, Department of Energy, Oak Ridge Operations, Oak Ridge, TN 37830.
56-145. April Donegain, National Nuclear Data Center, ENDF, Brookhaven National Laboratory, Upton, NY 11973.
147-172. Technical Information Center, Oak Ridge, TN 37830.

☆U.S. GOVERNMENT PRINTING OFFICE: 1984-746-067/4113